Complex Hollow Structured Anodes for Sodium and Potassium Ion Batteries

Fangxi Xie

School of Chemical Engineering and Advanced Materials

Faculty of Engineering, Computer and Mathematical Science

A thesis submitted for the degree of Doctor of Philosophy

The University of Adelaide

July 2019

Table of Contents

Abstract

The development of the portable electronic devices, electrical vehicles, and smart grids boosts the development of electrical energy storage devices. Among them, lithium-ion batteries, a typical kind of rocking-chair batteries, have been considered as one of the most competitive choices. However, the limited lithium content in the Earth's crust raises a concern that its cost might increase with the growing demand for electrical vehicles. Therefore, due to the relatively abundant content of sodium and potassium, sodium and potassium ion batteries are considered as alternatives with reduced cost to lithium-ion batteries. Nevertheless, the electrode materials for these two devices suffers the sluggish ion reaction kinetics and the large volume expansion due to the larger ion radiuses of sodium-ion and potassium-ion than one of lithium-ion. Constructing hollow structured materials with shorten ion diffusion length and large voids to alleviate volume expansion is considered as one of the best approaches to solve those issues of sodium and potassium ion batteries. However, the rational design and engineering to hollow structure according to the features of these two batteries remain rarely reported. Additionally, more insightful understandings of the superior electrochemical performance of hollow structured electrodes are also needed. Therefore, this thesis aims to offer some hollow structured electrode materials with rational design and engineering for sodium and potassium ion batteries with insightful understandings.

Firstly, Chapter 2 summarizes the application and development trends of hollow structured electrode materials as anodes for sodium ion batteries. In this chapter, it points out that the future development of hollow structured electrode materials lays on the optimization of the confinement, the building units and the utilization of the inner voids. Therefore, the research efforts were mainly devoted in the rational design and synthesis of complex hollow structured anodes for sodium and potassium ion batteries in this thesis.

The first aspect is about sodium and potassium titanates, a kind of conventional intercalation anodes for sodium and potassium ion batteries. In Chapter 3, the building units of hollow structured $Na_2Ti_3O_7$ were tuning by changing the solvothermal reaction solvents. It has been demonstrated that $Na_2Ti_3O_7$ hollow spheres assembled from

nanosheets was with enhanced ion reaction kinetics by exhibiting a 33% higher charge capacity at the current density of 10 C than that of the ones assembled from nanoparticles. Furthermore, the as-prepared sample delivered a reversible capacity of over 60 mAh g^{-1} after 1000 continuous cycles at the high rate of 50 C. In Chapter 4, dual-shell structured sodium and potassium titanate cubes with oxygen vacancies were achieved. Various spectroscopy approaches were employed to offer an atomic understanding of the oxygen vacancies. Additionally, it was revealed by density functional theory calculation that the superior electrochemical performance originates from the enhanced conductivity which is induced by oxygen vacancies.

The second aspect of this thesis focuses on the synthesis of multi-shell structured anode materials for sodium and potassium ion batteries. Due to the large number of inward voids in hollow structured materials, hollow structured electrodes have been considered as with low volumetric energy density even though their high gravimetric energy density derived from their high reversible capacity. In Chapter 5, multi-shell structured Sb$_2$S$_3$ with high volumetric energy density and gravimetric energy density was synthesized. In the comparison of electrochemical performance, the multi-shell sample exhibited a higher reversible capacity than the one of pristine Sb$_2$S$_3$. Additionally, it also showed enhanced durability compared to its single-shell counterparts. These two points demonstrate the superiorities of multi-shell structured Sb$_2$S$_3$ to its single-shell counterpart and pristine Sb$_2$S$_3$. In Chapter 6, the dual-shell structured bismuth nanoboxes were synthesized and employed as anodes for potassium ion batteries. This as-prepared sample achieved an initial reversible capacity of over 300 mAh g^{-1} and the reversible capacity maintained over 200 mAh g^{-1} after 200 cycles under the current density of 1 C. More importantly, this dual-shell structured bismuth was employed as a concept of proof to reveal the origin of the improved reversible capacity of nanostructured alloy anodes. Through various *Operando* synchrotron-based techniques, it was revealed that there are different origins of improved reversible capacity under low current density and high current density. Under the low current density, *i.e.* 0.2 C, the improved reversible capacity originates from the change of the electrochemical reaction path, in which the nanostructure offers enhanced capability to tolerate the volume expansion. Additionally, in the scenario of high current density, for instance, 2 C, the nanostructured alloy anodes provide higher surface area, resulting in

more electrochemical surface reactions and, consequently, improved reversible capacity under high current density.

To sum up, this thesis includes several examples of rational design and engineering hollow structured materials, such as $Na_2Ti_3O_7$ hollow spheres assembled from ultrathin nanosheets with N-doped carbon coating, dual-shell structured titanates with oxygen vacancies, multi-shell structured Sb_2S_3 with enhanced energy density, and dual-shell structured bismuth nanoboxes. Furthermore, some insightful understandings of the origins of their superior electrochemical performance were acquired through various physicochemical and electrochemical characterizations.

Declaration

I certify that this work contains no material which has been accepted for the award of any other degree or diploma in my name, in any university or other tertiary institution and, to the best of my knowledge and belief, contains no material previously published or written by another person, except where due reference has been made in the text. In addition, I certify that no part of this work will, in the future, be used in a submission in my name, for any other degree or diploma in any university or other tertiary institution without the prior approval of the University of Adelaide and where applicable, any partner institution responsible for the joint-award of this degree.

I acknowledge that copyright of published works contained within this thesis resides with the copyright holder(s) of those works.

I also give permission for the digital version of my thesis to be made available on the web, via the University's digital research repository, the Library Search and also through web search engines, unless permission has been granted by the University to restrict access for a period of time.

Name of Candidate: Fangxi Xie

Signature:

Date: 2019. 07. 16.

Acknowledgments

This thesis can come to fruition only with the kind support and assistance of many people. I would like to extend my sincere thanks to all of them.

First and foremost, I owe my deepest gratitude to my principal supervisor, Prof. Shizhang Qiao, who has been supportive throughout my Ph.D. study with his patience, enthusiasm, and immense knowledge. Without his continuous guidance and valuable suggestion concerning this work, this thesis would hardly have been completed. I also want to thank my cosupervisor, Dr. Lei Zhang of the University of Adelaide, for his insightful comments and useful advices during my research and paper writing.

I am deeply indebted to all colleagues in Prof. Qiao's group at The University of Adelaide: Prof. Ling Tao of Tianjin University, Dr. Yao Zheng, Dr. Jiao Yan, Dr. Sheng Chen, Dr. Jingjing Duan, Dr. Ruifeng Zhou, Dr. Jingrun Ran, Dr. Lin Xiong, Dr. Bita Bayatsarmadi, Dr. Jinlong Liu, Dr. Lei Liu, Dr. Dongdong Zhu, Dr. Cheng Tang, Dr. Dongliang Chao, Dr. Bo You, Xuesi Wang, Chao Ye, Yongqiang Zhao, Anthony Vasileff, Yang Shi, Huanyu Jin, Chaochen Xu, Jieqiong Shan, Xin Liu, Mohammad Ziaur Rahman, Laiquan Li, Bingquan Xia, Huan Li, Dazhi Yao, Xin Xu, Yanzhao Zhang, Xing Zhi for the technological assistance, for the enlightening discussions, and for all the fun we have had in the last four years.

Special thanks go to Officers Michelle Fitton and Sue Earle, Jason Peak and Analytical Services Coordinator Dr. Qiuhong Hu from School of Chemical Engineering and Advanced Materials for their administrative helps; Microscopists Mr. Ken Neubauer, Dr. Lisa O'Donovan, Dr. Animesh Basak and Dr. Ashley Slattery from Adelaide Microscopy for their technical supports.

It is a great pleasure to express my heartfelt appreciation to those who contributed directly to some material characterizations: Dr. Qinfen Gu, Dr. Justin Kimpton, Dr. Helen Brand of PD beamline team, Dr. Bernt Johannessen of XAS beamline team, and Dr. Bruce Cowie, Dr. Lars Thomsen, Dr. Anton Tadich of soft X-ray spectroscopy team of Australian Synchrotron, and Prof. Hugh Harris of The University of Adelaide, for their help and insightful discussion on synchrotron related techniques; Prof. Xianfeng Yang of South

Chapter 1 : Introduction

1.1 Significance of the project

The lithium-ion batteries have been widely used as the electrical energy storage devices in portable electronic devices and electric vehicles.[1-2] However, the rising demand for lithium-ion batteries from the electric vehicles industries induces the raising concern that the price of lithium will significantly increase because of the uneven distribution and relatively small content of lithium in the Earth's crust.[3-4] Therefore, developing similar rocking-chair batteries as cheaper alternatives to lithium-ion batteries is considered as a good solution.[5-8] Compared with the content of 20 ppm of lithium in the Earth's crust, owing to the relative abundance of sodium or potassium (23,000 ppm for sodium and 17,000 ppm for potassium), developing the sodium or potassium ion batteries is considered as a solution for this issue of limited content lithium of lithium-ion batteries.[3, 6-8]

Though the cheaper price of sodium or potassium ion batteries, there are mainly several issues about them as electrical energy storage devices. Firstly, the most significant issue for employing sodium or potassium ion batteries to replace the lithium-ion batteries is the larger ion radiuses of sodium-ion and potassium-ion, resulting in the sluggish ion transportation in the electrode materials.[7-10] Additionally, because of the lowest voltage vs. standard hydrogen electrode of lithium (-3.04V) and the relative higher ones of sodium (-2.71V) and potassium (-2.94V), sodium and potassium ion batteries are considered with lower energy densities than lithium-ion batteries.[9-10] Furthermore, the density functional theory (DFT) calculations and experimental results suggest that the electrochemical reactions of the electrode materials with sodium/potassium ions causes larger volume expansion than the one with lithium ions.[6-8] To sum up, there are mainly three challenges in developing the novel rocking-chair batteries: the sluggish ion transportation, the lower energy densities and the large volume expansion. Therefore, to realize the practical applications of sodium and potassium ion batteries, the electrode materials with enhanced ion transportation kinetics, enhanced energy density and improved capability to alleviate the volume expansion are highly desired.

Hollow structured materials, with the functional thin shells and the inner voids, offer the advantages of a large surface-to-volume ration, short diffusion length, large contact area, abundant inner voids to alleviate the volume expansion during cycling etc.[11-13] Therefore, the applications of hollow structured electrode materials exhibited great successes for lithium-ion batteries.[11-12] However, the previous researches demonstrated that the simple hollow structured materials are with drawbacks in fulfilling the requirement of sodium and potassium ion batteries.[14] Therefore, rational design and engineering hollow structured electrode materials based on the features of those batteries are highly desired but remain in the initial stage of development.[14]

1.2   Research objectives

The major goals of this thesis are to design and synthesize a series of complex hollow structured anode materials for sodium and potassium ion batteries and to acquire fundamental insights into their superior electrochemical performance. Specifically, the objectives of this thesis are:

- *To fabricate* a novel hollow structure of $Na_2Ti_3O_7$ spheres assembled from ultrathin $Na_2Ti_3O_7$ nanosheets with nitrogen-doped carbon coating with excellent rate performance as anodes for sodium-ion batteries;

- *To reveal* the sodium-ion transportation kinetics is highly related with the building units of the hollow structure by the better performance of hollow spheres assembled from nanosheets than the one of hollow spheres assembled from nanoparticles;

- *To design* a series of novel dual-shell structured titanate cubes with oxygen vacancies to achieve good rate performance and durability as anodes for sodium and potassium ion batteries;

- *To develop* an optimizing approach to promote the performance of titanates as anodes for both sodium and potassium ion batteries;

- *To synthesize* a novel multi-shell structured Sb_2S_3 with improved energy density, enhanced durability and superior reversible capacity;

- *To identify* the key barrier in the electrochemical reaction between sodium and nanostructured Sb_2S_3;

- *To manufacture* a novel dual-shell structured bismuth boxes with enhanced durability as anodes for potassium ion batteries;
- *To understand* the origins of the improved reversible capacity of alloy anodes for rocking-chair batteries under various current densities through various synchrotron-based techniques.

1.3 Thesis outline

This thesis is partial outcomes of my Ph.D. research presented in the form of journal publications. This thesis is mainly about various complex hollow structured anodes materials for sodium and potassium batteries. And it identifies the origins of their superior electrochemical performance. Specifically, the chapters in the thesis are presented in the following sequence:

➢ **Chapter 1** introduces the significances of design and engineering hollow structured electrode materials for sodium and potassium ion batteries. Additionally, it outlines the research objectives and key contributions to the field of hollow structured anode materials for sodium and potassium ion batteries.

➢ **Chapter 2** reviews the recent application and development trends of hollow structured anodes for sodium ion batteries.

➢ **Chapter 3** reports a rational design and synthesis of $Na_2Ti_3O_7$@N-doped carbon hollow spheres with excellent rate performance as anodes for sodium ion batteries.

➢ **Chapter 4** studies a general approach to optimize the electrochemical performance of titanate and investigates the origin of this superior electrochemical performance.

➢ **Chapter 5** develops multi-shell hollow structured Sb_2S_3 with superior energy density, durability and reversible capacity.

➢ **Chapter 6** employs dual-shell structured bismuth boxes in potassium ion batteries as a concept of proof to investigate the origins of the improved reversible capacity of alloy anodes for rocking-chair batteries.

➢ **Chapter 7** presents the conclusions and perspectives for future work on rational design and engineering hollow structured anodes for novel rocking-chair batteries.

1.4 References

1. Tarascon, J. M.; Armand, M., Issues and Challenges Facing Rechargeable Lithium Batteries. *Nature* **2001**, *414*, 359-367.

2. Armand, M.; Tarascon, J. M., Building Better Batteries. *Nature* **2008**, *451*, 652-657.

3. Larcher, D.; Tarascon, J. M., Towards Greener and More Sustainable Batteries for Electrical Energy Storage. *Nat. Chem.* **2015**, *7*, 19-29.

4. Tarascon, J. M., Is Lithium the New Gold? *Nat. Chem.* **2010**, *2*, 510.

5. Yabuuchi, N.; Kubota, K.; Dahbi, M.; Komaba, S., Research Development on Sodium-Ion Batteries. *Chem. Rev.* **2014**, *114*, 11636-11682.

6. Kim, H.; Kim, J. C.; Bianchini, M.; Seo, D.-H.; Rodriguez-Garcia, J.; Ceder, G., Recent Progress and Perspective in Electrode Materials for K-Ion Batteries. *Adv. Energy Mater.* **2018**, *8*, 1702384.

7. Hwang, J. Y.; Myung, S. T.; Sun, Y. K., Recent Progress in Rechargeable Potassium Batteries. *Adv. Funct. Mater.* **2018**, *28*, 1802938.

8. Hwang, J. Y.; Myung, S. T.; Sun, Y. K., Sodium-Ion Batteries: Present and Future. *Chem. Soc. Rev.* **2017**, *46*, 3529-3614.

9. Nayak, P. K.; Yang, L.; Brehm, W.; Adelhelm, P., From Lithium-Ion to Sodium-Ion Batteries: Advantages, Challenges, and Surprises. *Angew. Chem. Int. Ed.* **2018**, *57*, 102-120.

10. Wu, X.; Leonard, D. P.; Ji, X., Emerging Non-Aqueous Potassium-Ion Batteries: Challenges and Opportunities. *Chem. Mater.* **2017**. *29*, 5031-5042

11. Yu, L.; Wu, H. B.; Lou, X. W., Self-Templated Formation of Hollow Structures for Electrochemical Energy Applications. *Acc. Chem. Res.* **2017,** *50*, 293-301.

12. Yu, L.; Hu, H.; Wu, H. B.; Lou, X. W., Complex Hollow Nanostructures: Synthesis and Energy-Related Applications. *Adv. Mater.* **2017,** *29*, 1604563.

13. Zhou, L.; Zhuang, Z.; Zhao, H.; Lin, M.; Zhao, D.; Mai, L., Intricate Hollow Structures: Controlled Synthesis and Applications in Energy Storage and Conversion. *Adv. Mater.* **2017,** *29*, 1602914.

14. Xie, F.; Zhang, L.; Ye, C.; Jaroniec, M.; Qiao, S. Z., The Application of Hollow Structured Anodes for Sodium-Ion Batteries: From Simple to Complex Systems. *Adv. Mater.* **2018,** *30*, 1800492.

Chapter 2 : Literature Review

2.1 Introduction

This chapter is mainly about the applications of hollow structured anodes for sodium ion batteries. By summarizing the developments of hollow structured anodes, we developed the concept of simple and complex hollow structured anodes for sodium ion batteries. Because of the differences between sodium and lithium-ion batteries, complex hollow structured anodes have been developed to meet the special requirements of being anode for sodium ion batteries. To summarize the novel hollow structures, the developments of hollow structured anodes with confinements, hierarchical structures, and multishell structure are highlighted and presented through recent studies. Finally, we also proposed several strategies to boost the development of complex hollow structured anodes for sodium ion batteries.

2.2 The Application of Hollow Structured Anodes for Sodium-Ion Batteries: From Simple to Complex Systems

This chapter is included as it appears as a journal paper published by Fangxi Xie, Lei Zhang, Chao Ye, Mietek Jaroniec, Shizhang Qiao, The application of hollow structured anodes for sodium-ion batteries: from simple to complex systems, *Advanced Materials*, 2018, 201800492.

Statement of Authorship

Title of Paper	The Application of Hollow Structured Anodes for Sodium‑Ion Batteries: From Simple to Complex Systems
Publication Status	☑ Published ☐ Accepted for Publication ☐ Submitted for Publication ☐ Unpublished and Unsubmitted work written in manuscript style
Publication Details	Fangxi Xie, Lei Zhang, Chao Ye, Mietek Jaroniec, Shizhang Qiao, The application of hollow structured anodes for sodium-ion batteries: from simple to complex systems, Advanced Materials, 2018, 201800492.

Principal Author

Name of Principal Author (Candidate)	Fangxi Xie
Contribution to the Paper	Manuscript Draft
Overall percentage (%)	70%
Certification:	This paper reports on original research I conducted during the period of my Higher Degree by Research candidature and is not subject to any obligations or contractual agreements with a third party that would constrain its inclusion in this thesis. I am the primary author of this paper.
Signature	Date 2019. May. 10.

Co-Author Contributions

By signing the Statement of Authorship, each author certifies that:

     i.   the candidate's stated contribution to the publication is accurate (as detailed above);

     ii.   permission is granted for the candidate in include the publication in the thesis; and

     iii.   the sum of all co-author contributions is equal to 100% less the candidate's stated contribution.

Name of Co-Author	Lei Zhang
Contribution to the Paper	Discussion of this manuscript and manuscript revision 10%
Signature	Date 11st of 2019

Name of Co-Author	Chao Ye
Contribution to the Paper	Discussion of this manuscript and manuscript revision 5%
Signature		Date	13/5/2019

Name of Co-Author	Mietek Jaroniec
Contribution to the Paper	Discussion of this manuscript and manuscript revision 5%
Signature		Date	May 12, 2019

Name of Co-Author	Shizhang Qiao
Contribution to the Paper	Supervision of the work, discussion of this manuscript and manuscript evaluation 10%
Signature		Date	May 13, 2019

Please cut and paste additional co-author panels here as required.

15

The Application of Hollow Structured Anodes for Sodium-Ion Batteries: From Simple to Complex Systems

Fangxi Xie, Lei Zhang, Chao Ye, Mietek Jaroniec, and Shi-Zhang Qiao*

Hollow structures exhibit fascinating and important properties for energy-related applications, such as lithium-ion batteries, supercapacitors, and electrocatalysts. Sodium-ion batteries, as analogs of lithium-ion batteries, are considered as promising devices for large-scale electrical energy storage. Inspired by applications of hollow structures as anodes for lithium-ion batteries, the application of these structures in sodium-ion batteries has attracted great attention in recent years. However, due to the difference in lithium and sodium-ion batteries, there are several issues that need to be addressed toward rational design of hollow structured sodium anodes. Herein, this research news article presents the recent developments in the synthesis of hollow structured anodes for sodium-ion batteries. The main strategies for rational design of materials for sodium-ion batteries are presented to provide an overview and perspectives for the future developments of this research area.

1. Introduction

Sodium-ion batteries are considered as the most competitive electrical energy storage devices for smart grids to enable the practical application of renewable energy.[1–4] They have similar working mechanism as lithium-ion batteries but possess much lower cost due to cheaper sodium and aluminum current collectors.[5–7] However, there are still some major barriers for their wide-scale usage.[8,9] One of them is the lack of suitable anode materials. Therefore, the search for a suitable anode for sodium-ion batteries is an essential task toward practical usage of sodium-ion batteries. Like the anodes for lithium-ion batteries, there are several kinds of anodes for sodium-ion batteries based on the insertion, alloying, or conversion mechanism.[9,10] Among three kinds of anodes, the most widely applied ones are those based on the insertion mechanism. Basically, the "insertion" anodes involve a sodium-ion storage mechanism that is

F. Xie, Dr. L. Zhang, C. Ye, Prof. S.-Z. Qiao
School of Chemical Engineering
The University of Adelaide
Adelaide, SA 5005, Australia
E-mail: s.qiao@adelaide.edu.au
Prof. M. Jaroniec
Department of Chemistry and Biochemistry
Kent State University
Kent, OH 44242, USA

The ORCID identification number(s) for the author(s) of this article can be found under https://doi.org/10.1002/adma.201800492.

a redox process taking place in the host material.[11] From a crystallographic point of view, this process is a reversible electrochemical reaction, which involves the change in the oxidation state of transition metals and a topotactic reversible intercalation of sodium ions inside the crystal structure of the host without major structural changes.[9,10] Except for the anodes based on the insertion mechanism, there are also anodes based on the alloying or conversion mechanism.[9] The anodes based on the alloying mechanism are those that can electrochemically store sodium ions via alloying reaction ($M + nNa^+ + ne^- = Na_nM$).[9,12–14] In this electrochemical reaction, sodium ions form alloys with anode materials. Contrasting to the insertion mechanism, the bonds between host atoms are broken.[13] Therefore, the atomic framework of the host does not constrain the reaction, which grants the alloying anodes much higher specific capacity than that in the "insertion" anodes.[12,13] As regards anodes based on the conversion mechanism, the conversion reaction is usually defined as the reaction of sodium and a binary transition metal compound, M_aX_b (M = transition metal, X = O, S, P,...), to yield M nanoparticles embedded in a matrix of Na_yX.[9,10] This electrochemical reaction involves the full reduction of the transition metal to its metallic state, which assures high theoretical capacity.[10] Like in the case of alloying reaction, the bonds between M and X are broken, which grants the "conversion anodes" high theoretical capacity. Since the crystal structure is destroyed and new compounds are formed during these electrochemical reactions, the high capacity anodes undergo severe volume expansion and the consequent capacity fading upon cycling.[9,12,15,16] This is one of the key obstacles toward practical applications of these high capacity anodes.

Hollow structured materials, with the functional thin shells and the inner voids, offer the advantages of a large surface-to-volume ratio, short diffusion length, large contact area, etc.[17–19] Resulting from numerous benefits, they have been widely employed in several fields, for example, electrocatalysts, supercapacitors, and lithium-ion batteries.[17–20] Instead of modifying nanostructure of anode materials for lithium-ion batteries, the employment of hollow structured materials resulted in a significant enhancement of the rate performance, durability, and specific capacity.[17–23] While the rational design of hollow structured anodes for sodium-ion batteries is similar to that of hollow structured anodes for lithium-ion batteries, the requirements referring to the properties of materials are different

due to the differences in sodium and lithium-ion batteries. First, because the expansion and strain of anodes in sodium-ion batteries during charging/discharging processes are more significant than those in the anodes used in lithium-ion batteries, the sodium anodes are easier to peel off.[9] Therefore, in the rational design of hollow structured anodes for sodium-ion batteries, apart from the simple hollow structure, there is a need to design an extra space to accommodate a larger volume expansion. Additionally, due to the larger ion radius of sodium, the reaction kinetics is more sluggish during the charging/discharging processes than that in the case of lithium-ion batteries.[5,6,9] Hence, in addition to the simple hollow structured anode to reduce the diffusion length at the interface between electrode material and electrolyte, the building block should be specially designed to accelerate the ion diffusion in the hollow structure to further enhance the sodium kinetics.[17,24] The most importantly, due to the lower voltage of sodium cathodes than those of lithium cathodes, the energy density of sodium-ion batteries is lower than that of lithium-ion batteries.[5,8] Another concern is the low volumetric density of hollow structured electrode materials.[16,25–28] Therefore, because of the low energy density of sodium-ion batteries and the low volumetric density of hollow structured electrode materials, the energy density of anodes in sodium-ion batteries is one of the major concerns toward application of these batteries. To sum up, although the design of hollow structured anodes for sodium-ion batteries should be similar to that in the case of lithium-ion batteries, the different features of these batteries require the use of proper anode materials.

There are several reports on the use of hollow structured anodes in sodium-ion batteries but a critical appraisal of this important area of research is not available yet. Here, we summarize recent advances in the development of hollow structured anodes for sodium-ion batteries. First, we present the progress in the application of simple hollow structured anodes in sodium-ion batteries. After that, the fabrication and application of different complex hollow structured anodes for sodium-ion batteries are discussed. Finally, a brief outlook of the future trends in this area is presented.

2. Simple Hollow Structures

In this section, we summarize the application of simple hollow structured anodes in sodium-ion batteries. These structures are defined as follows: (i) the hollow structure is without any confinement, (ii) the building blocks are simple nanoparticles without further tailoring, and (iii) the hollow structure consists of single shell. Among all kinds of "insertion" anodes, the carbon-based anodes are the most widely used.[29,30] For instance, Tang et al. developed simple carbon hollow spheres by hydrothermal carbonization of the mixture of poly(styrene) latex and D-glucose.[31] As compared to the solid carbon spheres, the hollow carbon spheres as shown in **Figure 1**A,B exhibited higher reversible capacities under both low and high current densities. Under the current density of 1 A g^{-1}, the hollow carbon spheres exhibited a reversible capacity of over 100 mA h g^{-1} while the solid ones delivered a reversible capacity of about 50 mA h g^{-1} (Figure 1C). This result demonstrates that

the hollow structure has favorable transport properties, which assure a superior electrochemical performance.

In addition to hollow spheres, hollow nanotubes, 1D hollow structures, are also attractive for sodium-ion batteries because of the structural stability and good conducting connectivity.[32–34] Liu et al. used the in situ transmission electron microscopy to investigate the behavior of hollow carbon nanofibers (CNF) for sodium-ion batteries. This study suggested that there is a strain caused by volume change during sodiation process, which can be partially alleviated by the hollow structure.[35] Except for hollow carbon tubes, there are also other reports on sodium titanate hollow tubes, another "insertion" anode. Thanks to the good connectivity of tubes and different modifications as shown in the scanning and transmission electron microscope (SEM and TEM) images, a capacity retention of over 90% after 10 000 cycles was achieved, demonstrating their excellent stability (Figure 1D–F).[36,37] As compared to the hollow spheres, thanks to the prolonged length and the consequently high length-to-diameter ratio, the 1D hollow structured anodes, for example, nanotubes, possess extra advantages of good conducting connectivity and better structural stability. Therefore, the nanotubes normally exhibit better cycling performance than hollow spheres.

There are also several reports on 3D hollow structures.[38–40] Zhao et al. prepared the 3D macroporous MXene films with different compositions. The as-prepared samples exhibited a reversible capacity of 250 mA h g^{-1} at 2.5 C after 1000 cycles, which was significantly better than the reversible capacity obtained on multilayer MXenes and MXene/CNT hybrid open structure (Figure 1G–I).[39] This work demonstrates that the proper architecture is crucial for achieving great electrochemical performance. As compared to 0D and 1D hollow structures, the 3D architecture provides higher electrolyte/electrode contact area, which is beneficial for the transportation of sodium ions, and consequently, assures a superior rate performance.

Numerous studies showed that the hollow structure of anodes is crucial for good electrochemical performance because of several reasons: (i) large amount of electrochemical active sites due to the large surface-to-volume ratio; (ii) large contact area between electrode and electrolyte; (iii) short ion diffusion path because of thin shell and inner void. The above-mentioned reasons grant the hollow structured anodes in sodium-ion batteries the performance better than that in the solid structured analogs.

3. Complex Hollow Structures

Although simple hollow structures possess many advantages, it is worth to mention that most of the reports on simple hollow structured anodes with good performance are not based on the alloying or conversion mechanism. On the other hand, several simple hollow structured "alloying and conversion" anodes have been reported.[41–44] Although they showed better electrochemical performance than pristine materials without hollow structure, it seems that the simple hollow structured anodes fail to achieve a satisfactory performance, which is in contrast to the simple hollow structured anodes for lithium-ion batteries. To find out the origin of the above-mentioned unsatisfactory performance, it is worth to mention that there are substantial differences between "alloying/conversion" anodes for sodium and

**ADVANCED
SCIENCE NEWS**
www.advancedsciencenews.com

**ADVANCED
MATERIALS**
www.advmat.de

Figure 1. A) and B) TEM images, and C) rate performance comparison of D-glucose derived carbon hollow spheres (0D) and solid carbon spheres as anodes for sodium-ion batteries. Reproduced with permission.[31] Copyright 2012, John Wiley & Sons, Inc. D) SEM and E) TEM images, and F) rate performance of hydrogenated $Na_2Ti_3O_7$ hollow tubes (1D) as anode for sodium-ion batteries. Reproduced with permission.[37] Copyright 2016, American Chemical Society. G) SEM and H) TEM images, and I) rate performance of different hollow MXene 3D frameworks as anode for sodium-ion batteries. Reproduced with permission.[39] Copyright 2017, John Wiley & Sons, Inc.

lithium-ion batteries: the larger volume expansion, the severe strain, lower voltages, etc. These reasons cause that the simple hollow structured anodes assembled via alloying or conversion mechanism show superior performance in lithium-ion batteries, but only a moderate performance in sodium-ion batteries. Therefore, there is a need for improving the design of anodes in sodium-ion batteries to obtain the optimal durability, enhanced transport of sodium ions and electrons, and higher energy density. This improvement can be achieved by developing complex hollow structured anodes. In this section, we present the developments of the complex hollow structured anodes with confinements, hierarchical structures, or multishell structures.

3.1. Hollow Structured Anodes with Confinements

Chevrier and Ceder compared the relationship between the volumetric energy density and volume expansion in the "alloying"

anodes for lithium and sodium-ion batteries through first principles calculations.[45] It was shown that the Na alloying compounds should be able to accommodate about 150% of volume expansion in order to reach the similar capacity as anodes for lithium-ion batteries. Specifically, based on the density functional theory (DFT) calculations and phase diagrams of Na-Sn, the expansion of alloying reaction of Sn to storage sodium ions is 420%, which is also proved via the in situ X-ray diffraction and in situ transmission microscopy technique.[46,47] On the contrary, the expansion caused by the alloying reaction of lithium and tin is only 260%, which is just about 62% of the former.[16,48] Hence, during the sodiation/desodiation processes, due to the larger radius of sodium ion than that of lithium ion, the electrochemical reaction with sodium ions causes much larger expansion than that in lithium-ion batteries.[9,45] From this perspective, the inner void of hollow structure should be suitable to accommodate this larger volume expansion.[17–19,49] However, it has been demonstrated that the electrode materials
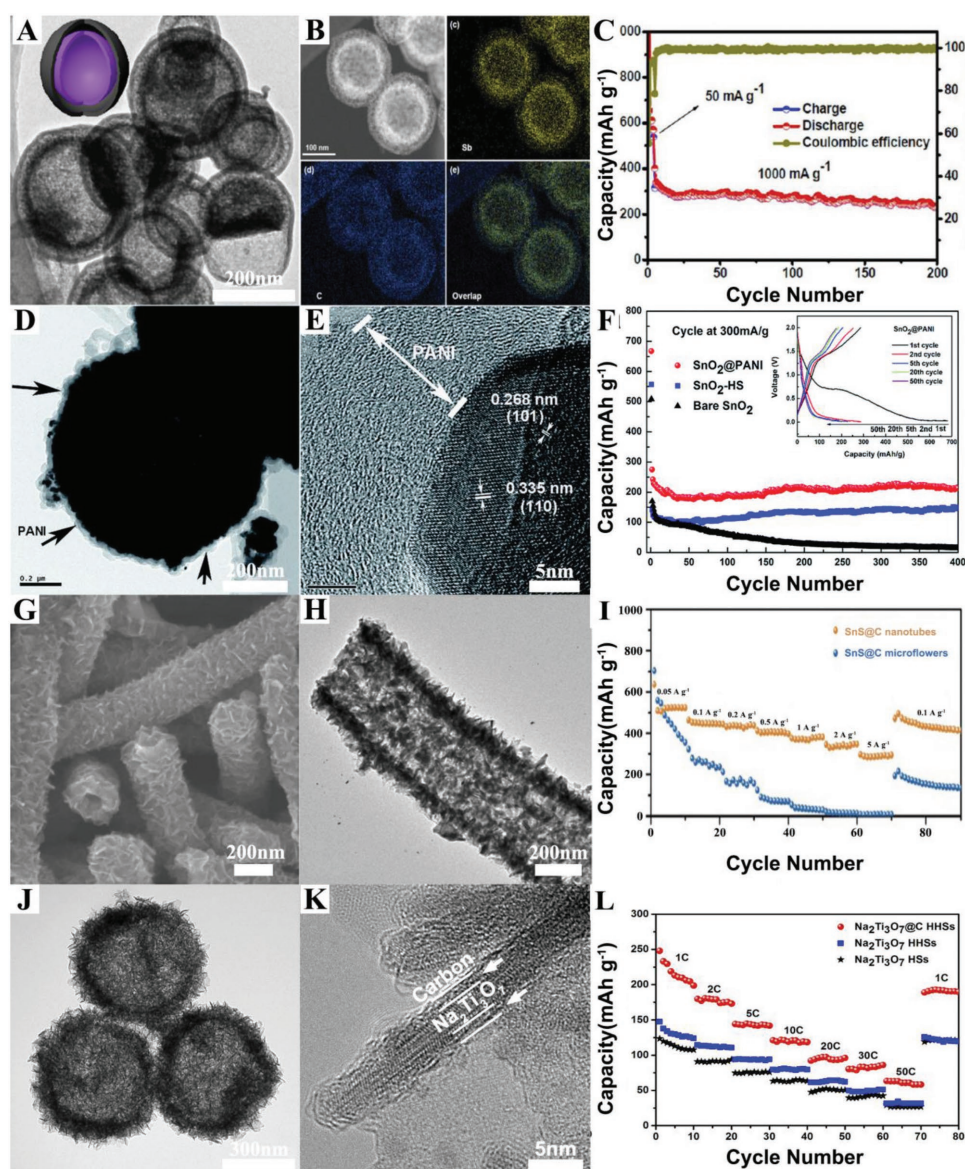
Figure 2. A) Low-magnification TEM, B) TEM elemental Mapping images, and C) cycling performance of carbon coating antimony hollow spheres as anode for sodium-ion batteries. Reproduced with permission.[55] Copyright 2016, American Chemical Society. D) Low-magnification TEM, E) high-magnification TEM images, and F) rate performance comparison of SnO_2 hollow spheres with polyaniline (SnO_2@PANI), SnO_2 hollow spheres (SnO_2-HS), and bare SnO_2 as anode for sodium-ion batteries. Reproduced with permission.[56] Copyright 2015, Royal Society of Chemistry. G) Low-magnification SEM, H) high-magnification TEM images of SnS nanotubes with carbon coating, and I) rate performance comparison of SnS nanotubes with carbon coating and SnS microflowers with carbon coating. Reproduced with permission.[61] Copyright 2017, John Wiley & Sons, Inc. J) Low-magnification TEM, K) high-magnification TEM images of hollow spheres assembled by N-doped carbon coating $Na_2Ti_3O_7$ nanosheets ($Na_2Ti_3O_7$@C HHSs), and L) rate performance comparison of hollow spheres assembled by $Na_2Ti_3O_7$ nanoparticles ($Na_2Ti_3O_7$ HSs), hollow spheres assembled by $Na_2Ti_3O_7$ bare nanosheets ($Na_2Ti_3O_7$ HHSs), and $Na_2Ti_3O_7$@C HHSs as anodes for sodium-ion batteries. Reproduced with permission.[24] Copyright 2017, John Wiley & Sons, Inc.

still suffer large strain even in the case of hollow structures.[49] Therefore, to develop a suitable confinement to maintain the integrity of active material is considered as one of the useful approaches to counteract the larger volume expansion caused by electrochemical reactions.[50–53] Additionally, due to the large exposed surface, the hollow structured anodes often lead to low initial Coulombic efficiency.[20] Introducing some confinement can be helpful to create a more stable solid electrolyte interface (SEI) film to enhance the initial Coulombic efficiency.[54]

For example, Liu et al. employed carbon confinement to enhance the performance of hollow Sb nanoparticles (**Figure 2**A,B). The carbon-coated antimony hollow spheres showed a high capacity of 280 mA h g^{-1} after 200 cycles under the current density of 1000 mA g^{-1} (Figure 2C).[55] In addition to carbon, a conductive polymer coating is also an advantageous way to improve the cyclic stability and rate performance of those high capacity anodes. Zhao et al. employed polyaniline (PANI) to improve the performance of SnO_2 hollow spheres

ADVANCED
SCIENCE NEWS

www.advancedsciencenews.com

ADVANCED
MATERIALS

www.advmat.de

used as an anode for sodium-ion batteries. By introducing the polyaniline as a soft elastic coating to buffer the volume change and create a stable SEI layer during charging/discharging, the reversible capacity of SnO_2 hollow spheres after 400 cycles under the current density of 300 mA g^{-1} was improved from 145.5 to 213.5 mA h g^{-1}, as well as the initial Coulombic efficiency was improved too. The enhanced cycling performance was attributed to the PANI buffer layer, which is beneficial for alleviating the volume change and prevent agglomeration (Figure 2D–F).[56]

Due to the larger radius of sodium ions, as compared to that of lithium ions, the volume change for "alloying/conversion" anodes is significant, which affects the anode durability.[57] With the inner voids, the hollow structure is naturally well suited to alleviate the volume change. However, without the confinement, even with hollow structure, due to the larger expansion, these high capacity anodes are still easy to peel off, which causes a large amount of irreversible capacity. On the contrary, anodes with the confinement, the papers mentioned previously and other reports demonstrate that the confinement can be beneficial for enhancing the cycling performance because the outward confinement can guarantee that the active materials are contained in the confinement after the expansion.[44,58,59] Therefore, employing confinement is a useful approach to optimize the performance of hollow structured anodes for sodium-ion batteries.

3.2. Hollow Anodes with Hierarchical Structure

Due to the larger radius of sodium ions, the strain during charging/discharging processes of anodes for sodium-ion batteries is much larger than that in lithium-ion batteries.[9] Su et al. developed a finite element model (FEM) with different densities of voids, to show that the average von Mises stress during sodiation/desodiation among different hollow spheres with different densities of voids can vary from 5.5 to 0.43 GPa, which is about 12.8-fold difference.[49] The above-mentioned work demonstrates that the stability of hollow spheres during sodiation/desodiation can be enhanced by introducing voids in the outer shells. For example, Zhou et al. used a wet-chemical synthesis method to obtain hollow red-phosphorus nanospheres with porous shells as anodes for sodium-ion batteries and demonstrated that the porous hollow structure was maintained after cycling, indicating that the porosity of the functional walls can alleviate the strain.[60] Furthermore, He et al. reported the synthesis of hollow SnS nanotubes (Figure 2G,H). With the voids in SnS hierarchical hollow nanotubes, the SnS@C hollow nanotubes delivered an average specific capacity of 290 mA h g^{-1} under a high current density of 5 A g^{-1} (Figure 2I).[61] Liu et al. also demonstrated that the use of ultrathin nanosheets for fabrication of hierarchical structures is helpful to maintain the pristine morphology.[62] Those above-mentioned works demonstrate that introducing voids in hollow structures by optimizing the building blocks is an effective way to enhance their durability.

Additionally, apart from the "alloying/conversion" anodes, hierarchical structures are also beneficial for the "insertion" anodes. Due to the larger ion radius, more attention should be paid toward optimization of the reaction kinetics between electrode and sodium ions by employing optimal building blocks for hollow structured anodes.[37] For example, Pan et al. investigated the sodium storage and transport properties of layered $Na_2Ti_3O_7$ and suggested that the diffusion coefficient of sodium ions along $Na_2Ti_3O_7$ layers is about 15 orders of magnitude larger than that related to the transport of these ions through the layers.[63] Inspired by this finding, $Na_2Ti_3O_7$ hollow spheres assembled by different building blocks were obtained in various solvents (Figure 2J,K). As compared with the hollow spheres assembled by nanoparticles, the hollow spheres assembled by nanosheets showed 33% higher charge capacity at the current density of 10 C, demonstrating the superiority of ultrathin nanosheets as building blocks (Figure 2L).[24] This work showed that the rational design of building blocks is of great significance for improving the ion transport and, hence, improving sodium storage performance under high current densities.[24]

The previous works demonstrated that, as compared to the hollow structures assembled by nanoparticles, the hollow structured materials assembled by nanosheets or other tailored building blocks might possess other important features. For the "alloying/conversion" anodes, because of larger amount of voids in the functional walls, the use of tailored building blocks is beneficial to alleviate the strain. Regarding the "insertion" anodes, the optimized ion transport paths are able to assure the improved sodium-ion transport and, consequently, enhance the rate performance. Although great improvements were made in the lithium anodes by modifying the building blocks, there are still limited reports about modifying the building blocks of hollow structured anodes for sodium-ion batteries. Combining the hollow structure and the specific hierarchical building blocks could be an interesting way to improve the durability and rate performance of sodium anodes.

3.3. Hollow Structured Anodes with Multishells

Ong et al. used the first principle calculations to study the differences in the voltages of sodium-ion and lithium-ion-based intercalation cathodes. Because sodium-ion intercalation into a fixed positive electrode is energetically unfavorable as compared to the lithium-ion intercalation, the calculated and observed Na voltages for most of the cathodes are lower than the corresponding Li voltages.[64,65] Additionally, by taking into account the higher equivalent weight of sodium than that of lithium, sodium-ion batteries will have difficulties in competing with lithium-ion batteries in terms of energy density.[5] When the hollow structure with single shell is considered, because of the large inner void, the concern about the low tap density is essential.[15,16,28] As the consequence of the lower voltage of sodium-ion batteries and the lower tap density of hollow structured anodes with single shells, the energy density of hollow structured anodes for sodium-ion batteries is another crucial concern. As compared with the single shell counterparts, multishell hollow structured anodes often possess two extra advantages. First, they can utilize most of the voids, which are distributed in each shell to alleviate the strain during charging/discharging processes. This can improve the tap density of hollow structured material and maintain the advantages of hollow structure.

ADVANCED
SCIENCE NEWS
www.advancedsciencenews.com

ADVANCED
MATERIALS
www.advmat.de

Additionally, different shells enhance the stability because they support each other and assure protection of the interior shells by the exterior shells.[25–27] This grants the multishell hollow structured anodes better durability as compared to the hollow structured anodes with single shells.

The simplest multishell structure is yolk–shell structure. With the outer shell to protect the inner core, the stability of electrode material can be enhanced. With the inner void between the inner core and the outer shell, the strain during charging/discharging can be alleviated.[25–27] Also, the large void inside the outer shell is utilized by the inner core, which increases the tap density of electrode. Therefore, yolk–shell structure attracts large amount of attention.[66,67] Wang et al. reported the yolk–shell iron sulfide–carbon nanospheres with enhanced electrochemical performance (**Figure 3**A,B).[68] As regards the electrochemical performance, micro-FeS can only retain 195 mA h g^{-1} after 300 cycles, with a corresponding capacity retention of 37.8%. On the contrary, the core–shell

FeS@C nanospheres showed a similar trend as micro-FeS, indicating the core–shell structure cannot tolerate the volume change of the inner core. It is worth to mention that the yolk–shell FeS@C still retained a decent reversible capacity of 488 mA h g^{-1} with a higher capacity retention of 67.6%. This result showed that the bare micro-FeS featured the poorest durability, implying the importance of the protection by outer carbon shell. Additionally, this finding also suggests that the yolk–shell structure is preferable for tolerating the large volume variation of FeS inner core during sodiation/desodiation (Figure 3C).[68] Expect for the conversion anodes, this modification strategy is also effective for the anodes with combination mechanism of alloying and conversion. Liu et al. employed yolk–shell Sn_4P_3@C nanospheres as the anodes for sodium-ion batteries (Figure 3D,E) and showed that the as-prepared sample with the outer carbon shells was shown to tolerate the sodiation volume variation and, hence, granted this material an enhanced electrochemical performance. The galvanostatic
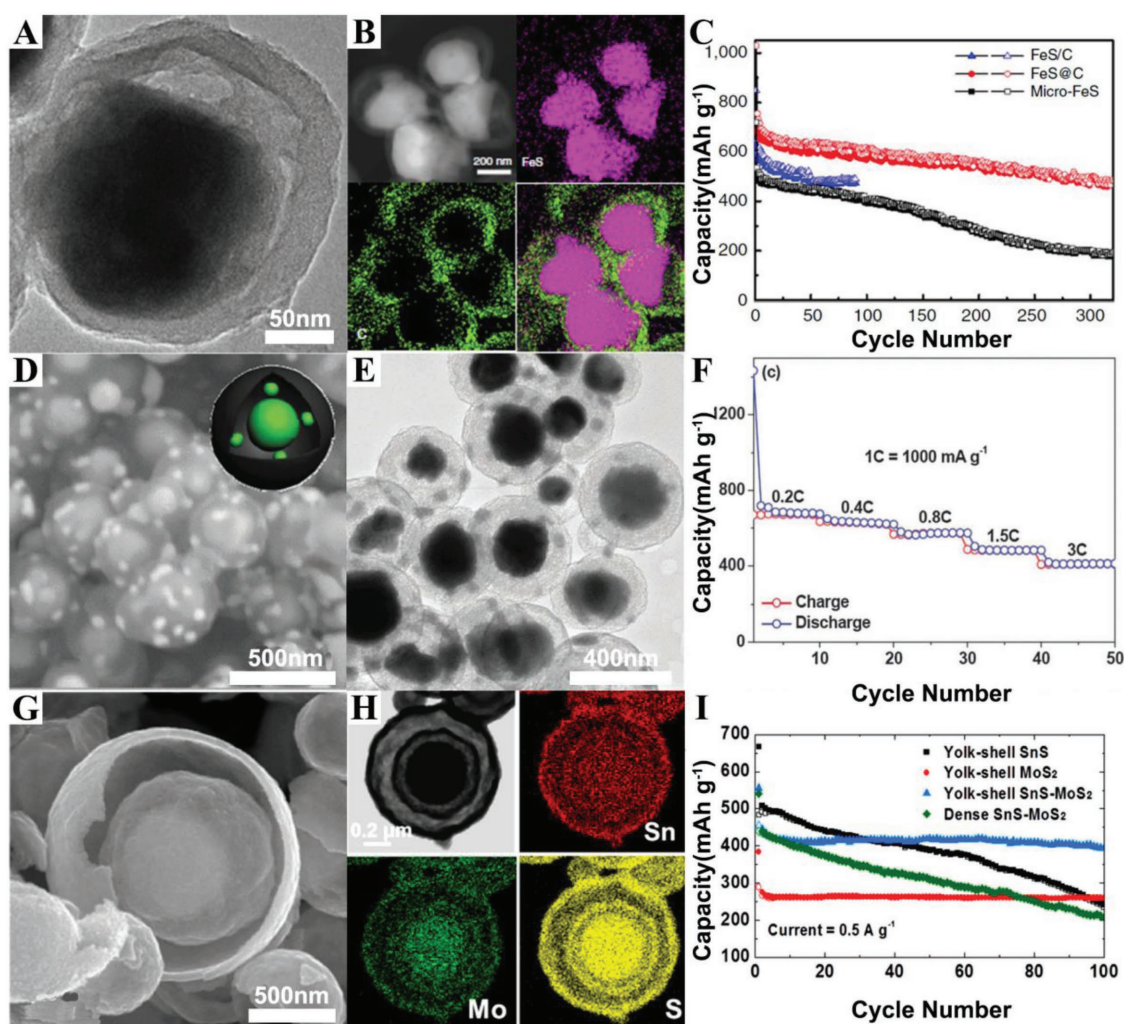
Figure 3. A) TEM, B) TEM elemental mapping images, and C) cycling performance comparison of microsized FeS, core–shell FeS/C nanoparticles (FeS/C), and yolk–shell FeS@carbon nanospheres (FeS@C) spheres as anodes for sodium-ion batteries. Reproduced with permission.[68] Copyright 2015, Nature Publishing Group. D) SEM, E) TEM images, and F) rate performance of yolk–shell Sn_4P_3@C nanospheres as anode for sodium-ion batteries. Reproduced with permission.[69] Copyright 2015, Royal Society of Chemistry. G) SEM, H) TEM elemental mapping images, and I) cycling performance of corresponding samples as anodes for sodium-ion batteries. Reproduced with permission.[70] Copyright 2015, American Chemical Society.

process showed that the as-prepared material delivered a highly stable discharge capacity of about 360 mA h g^{-1}, demonstrating the superiority of unique yolk–shell structure (Figure 3F).[69]

Though the many superiorities of yolk–shell structure, the inner core in this structure is still a solid nanosphere. Even with the protection of outer shell, the inner core still suffers the drawbacks of solid sphere. With the aims of utilizing the benefits of hollow structure and increasing energy density, hollow structure with more shells is the goal to achieve. However, there are limited reports of employing multishell anode for sodium-ion batteries. Choi et al. reported the synthesis of SnS-MoS$_2$ yolk–shell structure with two shells (Figure 3G). Though the TEM-EDX (energy-dispersive X-ray spectroscopy) analysis, the multishells of as-prepared sample and the uniform distribution of SnS and MoS$_2$ can be confirmed (Figure 3H). In the comparison of sodium-ion storage cycling performance, the yolk–shell SnS showed the highest initial capacity but with poor durability while the yolk–shell MoS$_2$ showed good stability but with poor initial capacity. Also, the specific capacity of dense SnS-MoS$_2$ microspheres showed a similar trend as the yolk–shell SnS but a slightly improved stability. With the protection of outer shells and the support from MoS$_2$, the yolk–shell structure with two shells showed a high reversible capacity and a similar stability with yolk–shell MoS$_2$, demonstrating the superiority of the yolk–shell structure with multishells (Figure 3I).[70]

To sum up, there are two crucial issues facing the hollow structured anode materials, which are the low energy density and poor durability. The above-mentioned works demonstrate that the multishell structured anodes provide similar performance to simple hollow structured anodes with increased volumetric capacity. Additionally, with the support from the outer shell to the inner shell, the durability of hollow structured anodes can be enhanced. Therefore, multishell hollow structure with improved energy density and durability should be one of the future directions for the development of hollow structured anode materials for sodium-ion batteries.

4. Conclusion and Outlook

In summary, we have reviewed the state-of-the-art research activities in hollow structured anodes for sodium-ion batteries. With the thin functional outer shell and the inner void, the hollow structure possesses several advantages: large surface-to-volume ratio for more electroactive sites, large void to accommodate the volume change as well as strain during sodiation/desodiation process and short diffusion length for sodium ions and electrons. Synthesizing hollow structured electrode materials has been widely applied as a modification strategy to optimize the electrochemical performance of anodes for sodium-ion batteries. However, there is still plenty room for the application of this strategy. First, apart from carbon or polymer, introduction of novel confinements to buffer the volume change and maintain the integrity of electrode is still an interesting topic for exploration. For example, various oxides have been proved as useful confinements to improve the durability of lithium-based electrodes.[71,72] Therefore, combining novel confinements and hollow structures can be an interesting area to be explored. Additionally, from the perspective of further optimization of the

ion and electron transport paths and introduction of voids to alleviate the strain, the presented works showed that employing optimized building blocks to construct the hollow spheres makes significant improvement of the rate performance and durability. Although various building blocks are employed to construct hollow structured anode for lithium-ion batteries, there are still limited effort on the use of optimized building blocks to construct hollow structured anodes for sodium-ion batteries, which is more urgent because of the larger ion radius, which leads to the more severe strain and more sluggish kinetics. Furthermore, the synthesis of hollow structured anode materials for sodium-ion batteries is still focused on the simple hollow spheres with single shells. Because of the low voltage of sodium-ion batteries and poor volumetric capacity of hollow structured electrodes, from the viewpoint of high energy density, the optimization of the void-to-solid ratio seems to be a promising solution. Therefore, the use of the multishell structure is the best approach to improve the void-to-solid ratio with all the advantages of hollow structured materials. However, there are still limited reports on the use of multishell hollow structured anodes for sodium-ion batteries. With the aims of obtaining good electrochemical performance and comparable energy density, the development of multishell hollow structured anodes is of great importance toward their practical applications.

Conflict of Interest

The authors declare no conflict of interest.

[1] Z. Yang, J. Zhang, M. C. W. Kintner-Meyer, X. Lu, D. Choi, J. P. Lemmon, J. Liu, *Chem. Rev.* **2011**, *111*, 3577.

[2] B. Dunn, H. Kamath, J. M. Tarascon, *Science* **2011**, *334*, 928.

[3] M. Armand, J. M. Tarascon, *Nature* **2008**, *451*, 652.

[4] P. G. Bruce, B. Scrosati, J. M. Tarascon, *Angew. Chem., Int. Ed.* **2008**, *47*, 2930.

[5] V. Palomares, P. Serras, I. Villaluenga, K. B. Hueso, J. Carretero-Gonzalez, T. Rojo, *Energy Environ. Sci.* **2012**, *5*, 5884.

[6] A. Ponrouch, D. Monti, A. Boschin, B. Steen, P. Johansson, M. R. Palacin, *J. Mater. Chem. A* **2015**, *3*, 22.

[7] G. Jeong, Y. U. Kim, H. Kim, Y. J. Kim, H. J. Sohn, *Energy Environ. Sci.* **2011**, *4*, 1986.

[8] W. Luo, F. Shen, C. Bommier, H. Zhu, X. Ji, L. Hu, *Acc. Chem. Res.* **2016**, *49*, 231.

[9] S. W. Kim, D. H. Seo, X. Ma, G. Ceder, K. Kang, *Adv. Energy Mater.* **2012**, *2*, 710.

[10] M. R. Palacin, *Chem. Soc. Rev.* **2009**, *38*, 2565.

[11] M. S. Whittingham, *Chem. Rev.* **2004**, *104*, 4271.

[12] M. Lao, Y. Zhang, W. Luo, Q. Yan, W. Sun, S. X. Dou, *Adv. Mater.* **2017**, *29*, 1700622.

[13] M. T. McDowell, S. W. Lee, W. D. Nix, Y. Cui, *Adv. Mater.* **2013**, *25*, 4966.

[14] M. N. Obrovac, V. L. Chevrier, *Chem. Rev.* **2014**, *114*, 11444.

[15] Y. Li, K. Yan, H. W. Lee, Z. Lu, N. Liu, Y. Cui, *Nat. Energy* **2016**, *1*, 15029.

[16] Y. Sun, N. Liu, Y. Cui, *Nat. Energy* **2016**, *1*, 16071.

[17] L. Yu, H. B. Wu, X. W. D. Lou, *Acc. Chem. Res.* **2017**, *50*, 293.

[18] L. Yu, H. Hu, H. B. Wu, X. W. Lou, *Adv. Mater.* **2017**, *29*, 1604563.

[19] L. Zhou, Z. Zhuang, H. Zhao, M. Lin, D. Zhao, L. Mai, *Adv. Mater.* **2017**, *29*, 1602914.

[20] C. Z. Yuan, H. B. Wu, Y. Xie, X. W. Lou, *Angew. Chem., Int. Ed.* **2014**, *53*, 1488.

[21] C. Ye, L. Zhang, C. Guo, D. Li, A. Vasileff, H. Wang, S. Z. Qiao, *Adv. Funct. Mater.* **2017**, *27*, 1702524.

[22] T. Yang, R. Zhou, D. W. Wang, S. P. Jiang, Y. Yamauchi, S. Z. Qiao, M. J. Monteiro, J. Liu, *Chem. Commun.* **2015**, *51*, 2518.

[23] J. Liu, T. Yang, D. W. Wang, G. Q. Lu, D. Zhao, S. Z. Qiao, *Nat. Commun.* **2013**, *4*, 2798.

[24] F. Xie, L. Zhang, D. Su, M. Jaroniec, S. Z. Qiao, *Adv. Mater.* **2017**, *29*, 1700989.

[25] J. Qi, X. Lai, J. Wang, H. Tang, H. Ren, Y. Yang, Q. Jin, L. Zhang, R. Yu, G. Ma, Z. Su, H. Zhao, D. Wang, *Chem. Soc. Rev.* **2015**, *44*, 6749.

[26] J. Wang, H. Tang, H. Wang, R. Yu, D. Wang, *Mater. Chem. Front.* **2017**, *1*, 414.

[27] J. Wang, H. Tang, L. Zhang, H. Ren, R. Yu, Q. Jin, J. Qi, D. Mao, M. Yang, Y. Wang, P. Liu, Y. Zhang, Y. Wen, L. Gu, G. Ma, Z. Su, Z. Tang, H. Zhao, D. Wang, *Nat. Energy* **2016**, *1*, 16050.

[28] N. Liu, Z. Lu, J. Zhao, M. T. McDowell, H. W. Lee, W. Zhao, Y. Cui, *Nat. Nanotechnol.* **2014**, *9*, 187.

[29] N. A. Kaskhedikar, J. Maier, *Adv. Mater.* **2009**, *21*, 2664.

[30] D. A. Stevens, J. R. Dahn, *J. Electrochem. Soc.* **2001**, *148*, A803.

[31] K. Tang, L. Fu, R. J. White, L. Yu, M. M. Titirici, M. Antonietti, J. Maier, *Adv. Energy Mater.* **2012**, *2*, 873.

[32] Y. L. Cao, L. F. Xiao, M. L. Sushko, W. Wang, B. Schwenzer, J. Xiao, Z. M. Nie, L. V. Saraf, Z. G. Yang, J. Liu, *Nano Lett.* **2012**, *12*, 3783.

[33] Y. Li, Y. Hu, M. M. Titirici, L. Chen, X. Huang, *Adv. Energy Mater.* **2016**, *6*, 1600659.

[34] S. Licht, A. Douglas, J. Ren, R. Carter, M. Lefler, C. L. Pint, *ACS Cent. Sci.* **2016**, *2*, 162.

[35] Y. Liu, F. Fan, J. Wang, Y. Liu, H. Chen, K. L. Jungjohann, Y. Xu, Y. Zhu, D. Bigio, T. Zhu, C. Wang, *Nano Lett.* **2014**, *14*, 3445.

[36] J. F. Ni, S. D. Fu, C. Wu, Y. Zhao, J. Maier, Y. Yu, L. Li, *Adv. Energy Mater.* **2016**, *6*, 1502568.

[37] S. Fu, J. Ni, Y. Xu, Q. Zhang, L. Li, *Nano Lett.* **2016**, *16*, 4544.

[38] J. Liu, Z. Yang, J. Wang, L. Gu, J. Maier, Y. Yu, *Nano Energy* **2015**, *16*, 389.

[39] M. Zhao, X. Xie, C. E. Ren, T. Makaryan, B. Anasori, G. Wang, Y. Gogotsi, *Adv. Mater.* **2017**, *29*, 1702410.

[40] H. Hou, C. E. Banks, M. Jing, Y. Zhang, X. Ji, *Adv. Mater.* **2015**, *27*, 7861.

[41] H. Hou, M. Jing, Y. Yang, Y. Zhu, L. Fang, W. Song, C. Pan, X. Yang, X. Ji, *ACS Appl. Mater. Interfaces* **2014**, *6*, 16189.

[42] Z. Yi, Q. Han, X. Li, Y. Wu, Y. Cheng, L. Wang, *Chem. Eng. J.* **2017**, *315*, 101.

[43] L. Wu, J. Lang, P. Zhang, X. Zhang, R. Guo, X. Yan, *J. Mater. Chem. A* **2016**, *4*, 18392.

[44] X. Ao, J. Jiang, Y. Ruan, Z. Li, Y. Zhang, J. Sun, C. Wang, *J. Power Sources* **2017**, *359*, 340.

[45] V. L. Chevrier, G. Ceder, *J. Electrochem. Soc.* **2011**, *158*, A1011.

[46] L. D. Ellis, T. D. Hatchard, M. N. Obrovac, *J. Electrochem. Soc.* **2012**, *159*, A1801.

[47] J. W. Wang, X. H. Liu, S. X. Mao, J. Y. Huang, *Nano Lett.* **2012**, *12*, 5897.

[48] Y. Abu-Lebdeh, *Nanotechnology for Lithium-Ion Batteries*, Springer, New York **2013**.

[49] D. W. Su, S. X. Dou, G. X. Wang, *J. Mater. Chem. A* **2014**, *2*, 11185.

[50] Y. C. Liu, N. Zhang, L. F. Jiao, Z. L. Tao, J. Chen, *Adv. Funct. Mater.* **2015**, *25*, 214.

[51] F. Xie, Y. Deng, Y. Xie, H. Xu, G. Chen, *Chem. Commun.* **2015**, *51*, 3545.

[52] L. Zhang, H. B. Wu, X. W. Lou, *Adv. Energy Mater.* **2014**, *4*, 1300958.

[53] Z. Liu, T. Lu, T. Song, X. Y. Yu, X. W. Lou, U. Paik, *Energy Environ. Sci.* **2017**, *10*, 1576.

[54] X. Zhou, L. Yu, X. Y. Yu, X. W. Lou, *Adv. Energy Mater.* **2016**, *6*, 1601177.

[55] J. Liu, L. Yu, C. Wu, Y. Wen, K. Yin, F. K. Chiang, R. Hu, J. Liu, L. Sun, L. Gu, J. Maier, Y. Yu, M. Zhu, *Nano Lett.* **2017**, *17*, 2034.

[56] X. Zhao, Z. Zhang, F. Yang, Y. Fu, Y. Lai, J. Li, *RSC Adv.* **2015**, *5*, 31465.

[57] Y. Du, X. Zhu, X. Zhou, L. Hu, Z. Dai, J. Bao, *J. Mater. Chem. A* **2015**, *3*, 6787.

[58] J. Chen, S. Li, V. Kumar, P. S. Lee, *Adv. Energy Mater.* **2017**, *7*, 1700180.

[59] C. Li, Q. Hu, Y. Li, H. Zhou, Z. Lv, X. Yang, L. Liu, H. Guo, *Sci. Rep.* **2016**, *6*, 25556.

[60] J. Zhou, X. Liu, W. Cai, Y. Zhu, J. Liang, K. Zhang, Y. Lan, Z. Jiang, G. Wang, Y. Qian, *Adv. Mater.* **2017**, *29*, 1700214.

[61] P. He, Y. Fang, X. Y. Yu, X. W. Lou, *Angew. Chem., Int. Ed.* **2017**, *56*, 12202.

[62] Y. Liu, X. Y. Yu, Y. Fang, X. Zhu, J. Bao, X. Zhou, X. W. Lou, *Joule* **2018**, *2*, 725.

[63] H. Pan, X. Lu, X. Yu, Y. S. Hu, H. Li, X. Q. Yang, L. Chen, *Adv. Energy Mater.* **2013**, *3*, 1186.

[64] S. P. Ong, V. L. Chevrier, G. Hautier, A. Jain, C. Moore, S. Kim, X. Ma, G. Ceder, *Energy Environ. Sci.* **2011**, *4*, 3680.

[65] P. K. Nayak, L. Yang, W. Brehm, P. Adelhelm, *Angew. Chem., Int. Ed.* **2018**, *57*, 102.

[66] S. Qiu, L. Xiao, X. Ai, H. Yang, Y. Cao, *ACS Appl. Mater. Interfaces* **2017**, *9*, 345.

[67] Y. J. Hong, J. H. Kim, Y. C. Kang, *J. Mater. Chem. A* **2016**, *4*, 15471.

[68] Y. X. Wang, J. Yang, S. L. Chou, H. K. Liu, W. X. Zhang, D. Zhao, S. X. Dou, *Nat. Commun.* **2015**, *6*, 8689.

[69] J. Liu, P. Kopold, C. Wu, P. A. van Aken, J. Maier, Y. Yu, *Energy Environ. Sci.* **2015**, *8*, 3531.

[70] S. H. Choi, Y. C. Kang, *ACS Appl. Mater. Interfaces* **2015**, *7*, 24694.

[71] S. Li, J. Niu, Y. C. Zhao, K. P. So, C. Wang, C. A. Wang, J. Li, *Nat. Commun.* **2015**, *6*, 7872.

[72] Z. W. Seh, W. Li, J. J. Cha, G. Zheng, Y. Yang, M. T. McDowell, P. C. Hsu, Y. Cui, *Nat. Commun.* **2013**, *4*, 1331.

Chapter 3 : Na₂Ti₃O₇@N-Doped Carbon Hollow Spheres for Sodium-Ion Batteries with Excellent Rate Performance

3.1 Introduction and Significance

$Na_2Ti_3O_7$ has been considered as a promising candidate for anode in sodium ion battery because of its low working voltage and consequently high energy density. However, its rate performance is limited by the poor conductivity and the sluggish ion transport kinetics. Therefore, rational design and synthesis of $Na_2Ti_3O_7$ to enhance the electrochemical performance remains a challenge. Here, by adjusting the synthesis conditions, $Na_2Ti_3O_7$ hollow spheres assembled from N-doped carbon coating nanosheets were obtained. This uniquely structured material exhibited excellent rate performance.

The highlights of this work include:

1. **Synthesis of Na₂Ti₃O₇ hollow spheres**

   Hollow spheres of $Na_2Ti_3O_7$ were synthesised to assure short ion diffusion paths and large surface area for the contact between the electrode material and electrolyte, were firstly synthesized.

2. **Rational design of two-dimensional structure of Na₂Ti₃O₇**

   $Na_2Ti_3O_7$ is a layered structure in which the sodium ions can be easily transported along the layer while their transport through the layer is difficult. Hence, the sheet-like nanostructure of $Na_2Ti_3O_7$, which has a small number of layers, was synthesized rationally to optimize the transport of sodium ions.

3. **N-doped carbon coating on Na₂Ti₃O₇**

   N-doped carbon, which might enhance both the transport of sodium ions and electrons, is used to improve the performance of $Na_2Ti_3O_7$ as an anode for sodium-ion battery for the first time, which further enhances the electrochemical performance.

4. **Excellent rate performance and durability**

   Thanks to the unique structure, this composite material showed excellent rate performance. Even under the high current density of 50 C, it can still deliver the specific capacity of more than 60 mAh g^{-1}. Also, it maintained over 90% of the capacity after 1000 cycles, demonstrating the good durability.

3.2 Na$_2$Ti$_3$O$_7$@N-doped carbon hollow spheres for sodium-ion batteries with excellent rate performance

This chapter is included as it appears as a journal paper published by Fangxi Xie, Lei Zhang, Dawei Su, Mietek Jaroniec, Shizhang Qiao, Na$_2$Ti$_3$O$_7$@N-doped carbon hollow spheres for sodium-ion batteries with excellent rate performance, ***Advanced Materials***, 2017, 201700989.

Statement of Authorship

Title of Paper	$Na_2Ti_3O_7$@N‑Doped Carbon Hollow Spheres for Sodium‑Ion Batteries with Excellent Rate Performance
Publication Status	☑ Published ☐ Accepted for Publication ☐ Submitted for Publication ☐ Unpublished and Unsubmitted work written in manuscript style
Publication Details	Fangxi Xie, Lei Zhang, Dawei Su, Mietek Jaroniec, Shizhang Qiao, $Na_2Ti_3O_7$@N‑Doped Carbon Hollow Spheres for Sodium‑Ion Batteries with Excellent Rate Performance, Advanced Materials, 2017, 201700989.

Principal Author

Name of Principal Author (Candidate)	Fangxi Xie
Contribution to the Paper	Research Plan, material synthesis, most of the characterizations and data analysis, electrochemical characterization, and manuscript Draft
Overall percentage (%)	70%
Certification:	This paper reports on original research I conducted during the period of my Higher Degree by Research candidature and is not subject to any obligations or contractual agreements with a third party that would constrain its inclusion in this thesis. I am the primary author of this paper.
Signature	Date 2019. May. 10.

Co-Author Contributions

By signing the Statement of Authorship, each author certifies that:

    i.   the candidate's stated contribution to the publication is accurate (as detailed above);

    ii.   permission is granted for the candidate in include the publication in the thesis; and

    iii.   the sum of all co-author contributions is equal to 100% less the candidate's stated contribution.

Name of Co-Author	Lei Zhang
Contribution to the Paper	Discussion of this manuscript and manuscript revision 10%
Signature	Date 11St of 2019

Name of Co-Author	Dawei Su
Contribution to the Paper	Acquiring high resolution transmission electron microscope image 5%
Signature		Date	2019. 5. 7

Name of Co-Author	Mietek Jaroniec
Contribution to the Paper	Discussion of this manuscript and manuscript revision 5%
Signature		Date	May 12, 2019

Name of Co-Author	Shizhang Qiao
Contribution to the Paper	Supervision of the work, discussion of this manuscript and manuscript evaluation 10%
Signature		Date	May 13, 2019

Please cut and paste additional co-author panels here as required.

Na$_2$Ti$_3$O$_7$@N-Doped Carbon Hollow Spheres for Sodium-Ion Batteries with Excellent Rate Performance

Fangxi Xie, Lei Zhang, Dawei Su, Mietek Jaroniec, and Shi-Zhang Qiao*

Uniform Na$_2$Ti$_3$O$_7$ hollow spheres assembled from N-doped carbon-coated ultrathin nanosheets are synthesized. A unique multilayer structure of nanosheets is presumed to significantly reduce energy consumption during the diffusion process of sodium ions, while the carbon-coated structure can increase the overall conductivity. The as-prepared sample used as an anode in sodium-ion batteries exhibits the best rate performance ever reported for Na$_2$Ti$_3$O$_7$, delivering more than 60 mAh g^{-1} after 1000 continuous cycles at the high rate of 50 C, which was achieved due to its unique structure.

Sodium-ion batteries have attracted a lot of attention due to the significantly reduced cost of the entire electrical energy storage system.[1–6] Among all kinds of anode materials employed in sodium-ion batteries, the Ti-based materials attracted a great attention due to their unique properties assuring high activity, low cost, and environmental friendliness.[7–10] Taking into account the lowest voltage of the Ti-based materials, Na$_2$Ti$_3$O$_7$ has been considered as an ideal anode material with high energy density.[11–16] Na$_2$Ti$_3$O$_7$ features a zigzag layered framework of TiO$_6$ octahedra, which are linked by edges. A large amount of energy is required for travel of sodium ions through a layer, which is much higher than that needed for travel along the layer.[12,13] Additionally, poor electron conductivity of Na$_2$Ti$_3$O$_7$ associated with its large bandgap (3.7 eV) creates another barrier for migration of electrons. Therefore, these factors are responsible for sluggish Na reaction kinetics, which limits the rate performance of Na$_2$Ti$_3$O$_7$ as an anode in sodium-ion batteries.[12,17]

In order to improve the performance of Na$_2$Ti$_3$O$_7$, numerous efforts have been undertaken to reduce the length of diffusion

paths of sodium ions and consequently, to enhance the sluggish Na reaction kinetics with Na$_2$Ti$_3$O$_7$. Zhang et al. reported a 3D spider-web architecture of Na$_2$Ti$_3$O$_7$. This unique structure reduces the diffusion length of sodium ions, which guarantees its superior electrochemical performance.[18] Meanwhile, besides the structure optimization, surface engineering has been considered as an effective way to improve the poor electronic conductivity of Na$_2$Ti$_3$O$_7$ and, hence, enhance its performance.[7,12,17] However, the lack of rationally designed nanostructured Na$_2$Ti$_3$O$_7$ for anodes in sodium-ion batteries limits its rate performance, especially under high current density, which is still unsatisfactory.

Hollow structures have been widely applied for the rational design of anode materials for lithium-ion batteries because they can offer short diffusion paths for transport of ions, high specific surface area accessible to the electrolyte, and a lot of active sites enhancing electrochemical activity under high current density.[9,10,19–24] Additionally, the large voids in hollow structures are beneficial to release the strain during charging/discharging processes.[19,25] Meanwhile, previous research shows that sodium ions migrate much easier along the Na$_2$Ti$_3$O$_7$ layers than through these layers.[12] Therefore, the hollow architectures assembled from nanosheets seem to be more desirable for Na$_2$Ti$_3$O$_7$ anodes in sodium-ion batteries because their unique structure can reduce the number of layers and consequently the energy consumption during the diffusion process of sodium ions travelling through these layers. As compared to the hollow spheres composed of nanoparticles, the hollow spheres assembled from Na$_2$Ti$_3$O$_7$ nanosheets may possess additional advantages, but their synthesis is more challenging.[26]

Besides optimization of the structure, carbon coating is considered as an effective strategy to improve the performance of Na$_2$Ti$_3$O$_7$ because it can serve as both the conducting additive to promote the electron transport in the poorly conductive Na$_2$Ti$_3$O$_7$ and the elastic buffer improving the stability of Na$_2$Ti$_3$O$_7$.[15,27,28] As compared with bare carbon materials, N-doped carbon might further enhance both ion and electron diffusion, resulting in enhanced electronic and ionic conductivity.[29] However, despite the merits brought by N-doped carbon, to the best of our knowledge, there is lack of reports on the surface modification of Na$_2$Ti$_3$O$_7$ with N-doped carbon.

Herein we report the first synthesis of Na$_2$Ti$_3$O$_7$ hollow spheres assembled from N-doped carbon-coated ultrathin Na$_2$Ti$_3$O$_7$ nanosheets. The hollow structure provides a large specific surface area, better access to the electrolyte, and shorter diffusion paths for both ions and electrons. The

F. Xie, Dr. L. Zhang, Prof. S.-Z. Qiao
School of Chemical Engineering
The University of Adelaide
Adelaide, SA 5005, Australia
E-mail: s.qiao@adelaide.edu.au
Dr. D. Su
Centre for Clean Energy Technology
Faculty of Science
University of Technology Sydney
Broadway, NSW 2007, Australia
Prof. M. Jaroniec
Department of Chemistry and Biochemistry
Kent State University
Kent, OH 44242, USA

The ORCID identification number(s) for the author(s) of this article can be found under http://dx.doi.org/10.1002/adma.201700989.
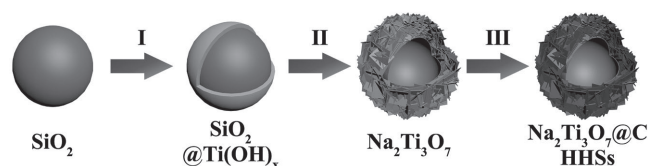
ADVANCED
SCIENCE NEWS
www.advancedsciencenews.com

ADVANCED
MATERIALS
www.advmat.de

Figure 1. Illustration of the route for synthesis of $Na_2Ti_3O_7$@C hollow spheres.

ultrathin nanosheets significantly decrease the number of $Na_2Ti_3O_7$ layers and, hence, provide preferable diffusion paths for sodium ions. Finally, the ultrathin carbon coating meaningfully enhances the conductivity and facilitates transport of electrons.[15] As expected, at the high current density of 50 C, the as-prepared $Na_2Ti_3O_7$ hollow spheres assembled from carbon-coated nanosheets could deliver a reversible capacity of more than 60 mAh g^{-1}, which is twice larger than the reversible capacity ($\approx$26 mAh g^{-1}) of the materials assembled from nanoparticles and nearly twice larger than the reversible capacity ($\approx$32 mAh g^{-1}) of the materials assembled from bare nanosheets, demonstrating the superiority of the sheet-like structure and the N-doped carbon coating.

The synthesis procedure of $Na_2Ti_3O_7$@C hollow spheres is schematically illustrated in **Figure 1**. First, highly uniform silica spheres were synthesized by Stöber method.[30,31] Second, the uniform amorphous titanium hydroxide was coated on the surface of silica template to obtain the titanium hydroxide-coated silica. Subsequently, hollow spheres composed of $Na_2Ti_3O_7$ ultrathin nanosheets were produced under hydrothermal conditions in sodium hydroxide aqueous solution probably due to the formation of a lamellar sodium titanate structure resulting from the intercalation of sodium cations between TiO_6 octahedral layers.[32] Next, dopamine was employed to

form polydopamine on the surface of nanosheets and create the polymer-coated nanosheets. Finally, the as-prepared sample was placed into a tube furnace and calcined to acquire the final product: hollow spheres composed of carbon-coated $Na_2Ti_3O_7$ ultrathin nanosheets. The resulting $Na_2Ti_3O_7$@C hierarchical hollow spheres are denoted as $Na_2Ti_3O_7$@C HHSs. For the purpose of comparison, hollow spheres assembled from $Na_2Ti_3O_7$ ultrathin nanosheets without carbon coating ($Na_2Ti_3O_7$ hierarchical hollow spheres denoted as $Na_2Ti_3O_7$ HHSs, Figure S1, Supporting Information) and hollow spheres assembled from $Na_2Ti_3O_7$ nanoparticles without carbon coating (denoted as $Na_2Ti_3O_7$ HSs, Figure S2, Supporting Information) were synthesized and the rate performance of those materials was tested, too.

Figure 2 shows the scanning electron microscope (SEM) images of the silica spheres before (panel a) and after (panel b) coating with titanium hydroxide. As shown in Figure 2a, the highly uniform silica templates with a smooth surface and a diameter of about 500 nm could be obtained by the Stöber method. After coating, the surface of as-prepared particles became rough (Figure 2b), indicating that titanium hydroxide was coated on the surface of silica spheres. The diameter of as-prepared particles increases to about 560 nm, which implies that the average thickness of Ti-based coating layer is about 30 nm. It is worth noting that the particles remained uniform after the aforementioned coating process (Figure S3, Supporting Information). Additionally, the roughness and 30 nm thickness of the coating layer are clearly visible on the transmission electron microscope (TEM) images (Figure 2c). The sample morphology after hydrothermal reaction with sodium hydroxide and the subsequent calcination was investigated by SEM (Figures S1 and S2, Supporting Information). It should be noted that the composition of reaction solvent has a significant
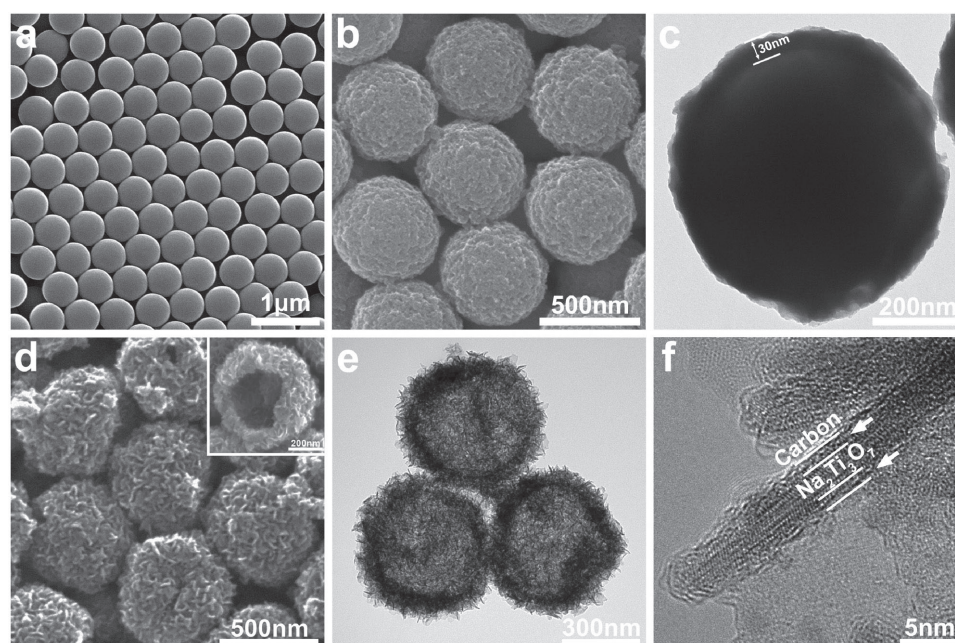

Figure 2. a) SEM images of silica spheres; b) SEM and c) TEM images of Si@Ti(OH)$_x$ spheres; d) SEM, e) TEM, and f) HRTEM images of $Na_2Ti_3O_7$@C HHSs.

ADVANCED
SCIENCE NEWS
www.advancedsciencenews.com

ADVANCED
MATERIALS
www.advmat.de
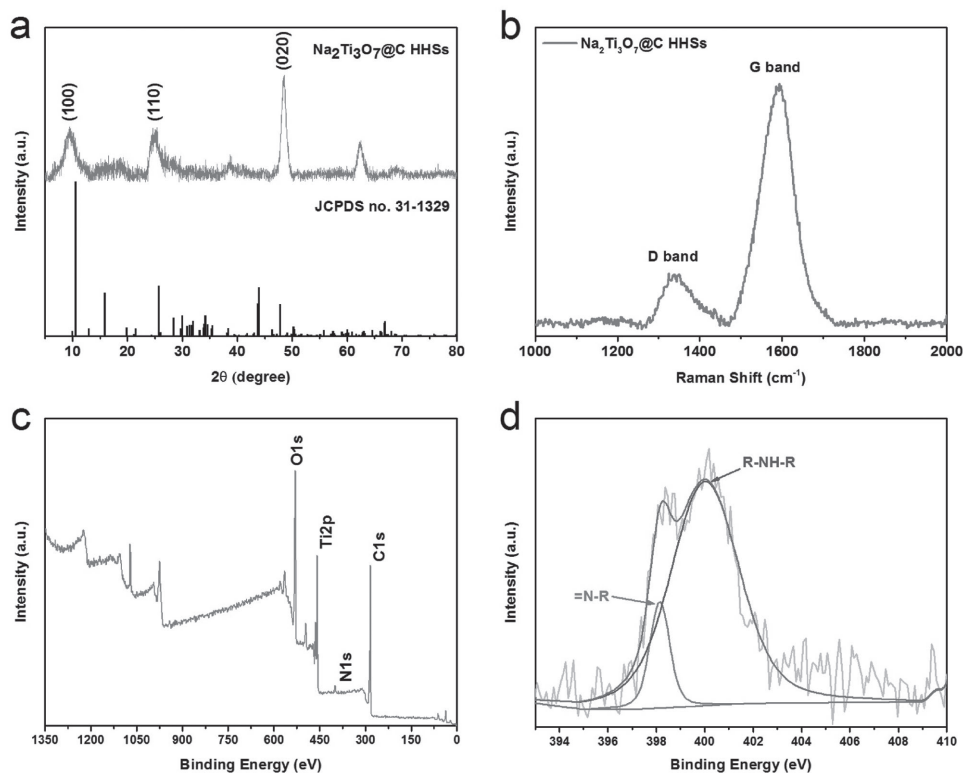
Figure 3. The structural analysis of $Na_2Ti_3O_7$@C HHSs. a) XRD patterns of $Na_2Ti_3O_7$@C HHSs. b) Raman spectra of $Na_2Ti_3O_7$@C HHSs. c,d) XPS survey and high-resolution N1s spectra of $Na_2Ti_3O_7$@C HHSs.

impact on the morphology of final products, especially in relation to the building blocks of hollow structures. When the reaction takes place in pure water, hollow spheres assembled from nanosheets are obtained (Figure S1, Supporting Information), while the hollow spheres assembled from small particles are formed in the water/ethanol mixed solution (Figure S2, Supporting Information).

The final particles ($Na_2Ti_3O_7$@C HHSs) were studied by SEM and TEM imaging analysis. As shown in Figure 2d and Figure S4 (Supporting Information), the $Na_2Ti_3O_7$@C HHSs particles are highly uniform spheres assembled from nanosheets. Their morphology is almost the same as that of the particles after treatment with sodium hydroxide but without carbon coating, indicating that the dopamine-derived carbon coating is ultrathin and highly uniform. As shown in the inset in Figure 2d,e, the hollow structure is clearly visible. The thickness of shell is estimated to be about 40 nm, while the nanosheets have the width of tens of nanometers. The detailed morphology can be further observed on high-resolution transmission electron microscope (HRTEM) images. The HRTEM images show 2D ultrathin nature of $Na_2Ti_3O_7$ sheets. It should be noticed that these ultrathin nanosheets with the thickness of less than 5 nm are highly uniform and consist of a few layers of $Na_2Ti_3O_7$ (Figure 2f and Figure S5, Supporting Information). Meanwhile, the detailed crystal structure of these nanosheets is revealed by HRTEM images of $Na_2Ti_3O_7$ HHSs (Figure S6, Supporting Information). As can be seen from the corresponding fast Fourier transform (FFT) pattern shown in Figure S6 (Supporting Information), the lattice spacings

of 0.207 and 0.206 nm with an interfacial angle of 88° can be indexed as $(\bar{4}02)$ and (104), revealing that the enclosed facets of $Na_2Ti_3O_7$ nanosheets are $\{0\bar{1}0\}$. This agrees with the $\{0\bar{2}0\}$ sharp peak visible on the X-ray powder diffraction (XRD) patterns (**Figure 3**a). As can be seen from Figure S6 (Supporting Information), the exposed facets can provide large tunnels for the diffusion of sodium ions.

The surface modification of $Na_2Ti_3O_7$ with carbon has been demonstrated as an effective way to improve the conductivity and, hence, the electrochemical performance.[7,15,33] Due to the large bandgap of 3.7 eV, $Na_2Ti_3O_7$ is considered as an insulator, which causes the sluggish kinetics of sodium ions and the poor rate performance of the pristine material. The carbon coating layer was employed to solve this issue. As shown in Figure 2f, the ultrathin and highly uniform carbon layer has been achieved and its thickness has been estimated to be below 2 nm. Additionally, the high angle annular dark field scanning transmission electron microscopy (HAADF-STEM) elemental mapping images (Figure S7, Supporting Information) also demonstrate the presence of carbon and its even distribution in the hollow spherical structures. Thermogravimetric analysis (Figure S8, Supporting Information) shows that the content of carbon in this composite material is about 24%. Furthermore, based on the Raman spectra (Figure 3b), it can be found that the intensity of G band located at around 1600 cm^{-1} (indicating the sp^2-hybridized graphitic carbon atoms) is much higher than the intensity of D band related to the disordered carbon atoms.[34–36] The Raman spectra indicate the highly graphitic nature of the carbon coating. The X-ray photoelectron

**ADVANCED
SCIENCE NEWS**

www.advancedsciencenews.com

**ADVANCED
MATERIALS**

www.advmat.de

spectroscopy (XPS) reveals the N-doped nature of this thin carbon coating (Figure 3c). According to Figure 3d, the high-resolution spectra of N 1s region can be fitted with two peaks: the one located at 400.0 cm^{-1} can be assigned to the secondary amine nitrogen (R−NH−R) and the one located at 398.1 cm^{-1} is attributed with tertiary/aromatic (=N−R) amine functionalities, demonstrating the N-doped nature of the carbon coating.[37] The N content in this composite material estimated from the survey XPS spectrum (Figure 3c) is 2.97%. Furthermore, Brunauer–Emmett–Teller (BET) surface area increases from 99 m^2 g^{-1} ($Na_2Ti_3O_7$ HSs), 168 m^2 g^{-1} ($Na_2Ti_3O_7$ HHSs) to 307 m^2 g^{-1} ($Na_2Ti_3O_7$@C HHSs) due to the 2D structure of nanosheets and the micropores present in the coated carbon layer (Figure S9, Supporting Information).

The cycling performance of $Na_2Ti_3O_7$@C HHSs was examined on the basis of galvanostatic discharge–charge measurements. The initial profiles for $Na_2Ti_3O_7$@C HHSs are shown in **Figure 4**a, which were recorded in the voltage range of 0.01–2.5 V versus Na/Na$^+$ at a current density of 1 C, corresponding to 177 mA g^{-1}. The first discharge capacity is 647 mAh g^{-1} while the first charge capacity is 278 mAh g^{-1}, resulting in a low Coulombic efficiency of 43.0% in the first cycle. This low Coulombic efficiency can be generally attributed to the decomposition of electrolyte and the formation of solid-electrolyte interfacial (SEI) film, which is also reflected by the initial cycles of $Na_2Ti_3O_7$ HHSs and $Na_2Ti_3O_7$ HSs with the corresponding Coulombic efficiencies of 53.8% and 57.4% (Figure S10, Supporting Information), respectively.[18] The
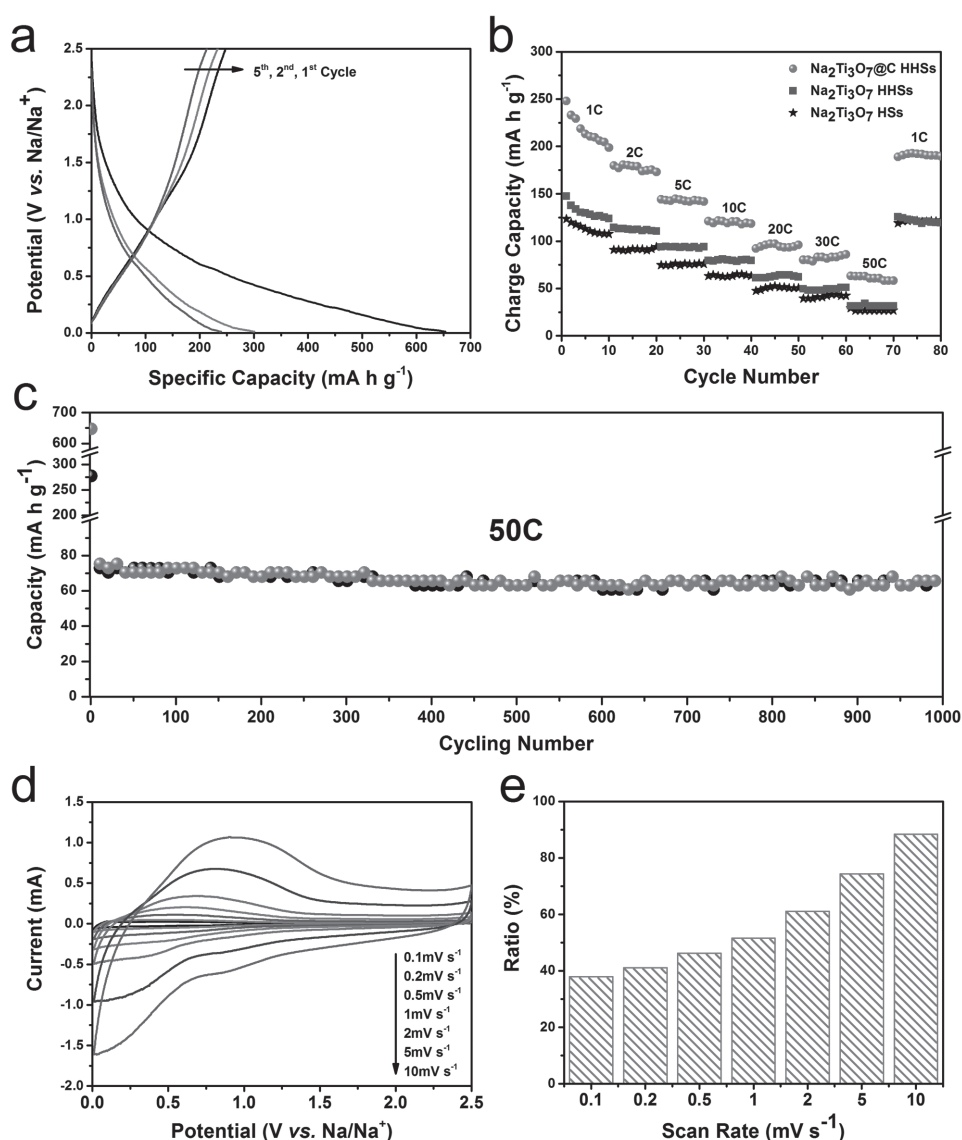
Figure 4. Electrochemical sodium-storage properties of $Na_2Ti_3O_7$@C HHSs: a) Initial discharge–charge voltage profiles of the first, second, and fifth cycles in the current density of 1 C. b) Rate performance of $Na_2Ti_3O_7$@C HHSs, $Na_2Ti_3O_7$ HHSs, and $Na_2Ti_3O_7$ HSs. c) Cycling performance of $Na_2Ti_3O_7$@C HHSs under the high current density of 50 C. d) CV curves of $Na_2Ti_3O_7$@C HHSs at various sweep rates. e) Diagram of capacitive contribution to the total capacity.

**ADVANCED
SCIENCE NEWS**

www.advancedsciencenews.com

**ADVANCED
MATERIALS**

www.advmat.de

low Coulombic efficiency is also suggested by the large void between the first cycle and the second cycle in the initial cyclic voltammetry (CV) profiles (Figure S11, Supporting Information). After five cycles, as shown in Figure 4c, the current density increased to about 50 C, corresponding to about 8.8 A g^{-1}. The corresponding Coulombic efficiency increased to over 90%, which implies the highly reversible nature of the as-prepared sample. It is noteworthy that the capacity fading for almost 1000 cycles is just 6.5%, corresponding to the initial cycle charging capacity of 72.8 mAh g^{-1} and the final cycle charging capacity of 68 mAh g^{-1}. This small capacity fading indicates a good durability of this uniquely structured material. To the best of our knowledge, this is the first report on the use of Na$_2$Ti$_3$O$_7$ under 50 C and it is also the best rate performance ever reported. The good durability and high reversible capacity, which is about 40% of the theoretical capacity of Na$_2$Ti$_3$O$_7$, verify the possibility of using this material as a high-performance anode for sodium-ion batteries. To evaluate the rate capability, Na$_2$Ti$_3$O$_7$@C HHSs were cycled at various current densities, while the charge capacities are shown in Figure 4b and the discharge/charge profiles are shown in Figure S12 (Supporting Information). Na$_2$Ti$_3$O$_7$@C HHSs exhibited reversible capacities of 210, 179, 142, 120, 94, 82, and 63 mAh g^{-1} at the current densities of 1, 2, 5, 10, 20, 30, and 50 C. First, at the current density of 50 C, Na$_2$Ti$_3$O$_7$ HHSs (no carbon coating) can only deliver about 50% charge capacity of Na$_2$Ti$_3$O$_7$@C HHSs, indicating a significant enhancement of the sodium-ion storage performance resulting from N-doped carbon coating. Second, Na$_2$Ti$_3$O$_7$ HHSs exhibit about 33% higher charge capacity at the current density of 10 C in comparison to Na$_2$Ti$_3$O$_7$ HSs, supporting the idea that the ultrathin nanosheets can improve the rate performance of Na$_2$Ti$_3$O$_7$. Also at higher current densities, Na$_2$Ti$_3$O$_7$ HHSs show smaller polarization than Na$_2$Ti$_3$O$_7$ HSs, which supports the idea of better sodium-ion transport in Na$_2$Ti$_3$O$_7$ HHSs (Figure S13, Supporting Information).[38] In conclusion, it has been demonstrated that this unique structure of N-doped carbon-coated ultrathin nanosheets can not only improve the conductivity but also facilitate the diffusion of sodium ions.

To further investigate the origin of the superior electrochemical performance of Na$_2$Ti$_3$O$_7$@C HHSs, the sodium-ion storage mechanism was investigated by CV techniques.[17,33,39,40] Figure 4d shows the CV curves at various sweep rates from 0.1 to 10 mV s^{-1}. At the higher sweep rates (higher than 2 mV s^{-1}), an obvious distortion from the basic shape is visible on the CV curves. This distortion is originated from several sources such as increased Ohmic contribution and/or diffusion constraints.[17] The contribution to the total charge stored resulting from the redox pseudocapacitance and intercalation can be analyzed by the following equations

$$i(V) = a_1 v + a_2 v^{1/2} \qquad (1)$$

or

$$i(V)/v^{1/2} = a_1 v^{1/2} + a_2 \qquad (2)$$

where $a_1 v$ represents the contribution of redox pseudocapacitance and double layer capacitance while $a_2 v^{1/2}$ reflects the contribution originating from the insertion processes.[17,33,39] If a_1

and a_2 are determined, the current response from the capacitive and insertion processes at the specific potential can be determined. As illustrated in Figure 4e, the contribution from the capacitive process to the total charge stored increases with increasing sweep rates. The pseudocapacitive contribution to the total capacity increases from 37.9% (the specific capacitive contribution is shown in Figure S14, Supporting Information), corresponding to the scan rate of 0.1 mV s^{-1}, to 88.3% at the scan rate of 10 mV s^{-1} (the specific capacitive contribution is shown in Figure S15, Supporting Information) while the capacitive contributions obtained for Na$_2$Ti$_3$O$_7$ HHSs and Na$_2$Ti$_3$O$_7$ HSs show similar trend (Figure S16, Supporting Information). Thanks to the high ratio of pseudocapacitive contribution in the total charge stored and the unique structure of hollow spheres assembled from N-doped carbon-coated nanosheets, Na$_2$Ti$_3$O$_7$@C HHSs exhibit an excellent performance as an anode for sodium-ion batteries under extremely high current density.

The above results clearly show that the unique structure of hollow spheres assembled from N-doped carbon-coated nanosheets can significantly enhance the sodium-ion storage performance of Na$_2$Ti$_3$O$_7$ as compared to the hollow spheres assembled from Na$_2$Ti$_3$O$_7$ nanosheets alone and the hollow spheres assembled from nanoparticles. Specifically, the hollow structure provides large surface area for the contact of the electrode material with electrolyte, which is beneficial for the transport of sodium ions. It is worth to mention that the hollow structure significantly reduces the diffusion length of sodium ions in Na$_2$Ti$_3$O$_7$.[19] Furthermore, the N-doped carbon coating with micropores provides a high surface area for electrode/electrolyte interface, which reduces the diffusion length of electrons and ions, and provides relatively high conductivity to improve the transport of electrons, while the aforementioned N-doping also results in the large number of reactive sites for sodium ions.[29,41] Additionally, the hollow spheres assembled from nanosheets can also provide more electrochemical active sites than those formed from nanoparticles due to the higher surface-to-volume ratio.[26] Most importantly, the prior theoretical studies show that the diffusion coefficient of sodium ions along Na$_2$Ti$_3$O$_7$ layers is about 15 orders of magnitude larger than that related to the transport of these ions through the layers.[12] Therefore, the 2D structure with fewer layers is preferable for the transport of sodium ions due to the large energy barrier associated with their migration through the layers, which is matched with the improved performance of hollow structure assembled from nanosheets (Na$_2$Ti$_3$O$_7$@C HHSs and Na$_2$Ti$_3$O$_7$ HHSs) in comparison to the hollow structure assembled from nanoparticles (Na$_2$Ti$_3$O$_7$ HSs) in this work. Our results prove that the significantly reduced dimension along the layers of ultrathin nanosheets can facilitate the diffusion of sodium ions in Na$_2$Ti$_3$O$_7$, resulting in greatly improved sodium kinetics and, hence, the excellent rate performance as an anode in sodium-ion batteries.

In summary, a novel nanostructure of hollow spheres assembled from N-doped carbon-coated ultrathin Na$_2$Ti$_3$O$_7$ nanosheets has been successfully synthesized. These well-defined Na$_2$Ti$_3$O$_7$ hollow spheres exhibit excellent sodium storage performance under high current density, due to the reduced diffusion length originating from their unique structure assembled from

**ADVANCED
SCIENCE NEWS**

www.advancedsciencenews.com

**ADVANCED
MATERIALS**

www.advmat.de

ultrathin nanosheets and the improved electronic conductivity of the N-doped carbon coating. All these features enhance the electrochemical performance of this anode material for sodium-ion batteries, leading to the excellent performance under the high current density. This study demonstrates that reducing the number of layers in nanosheets can enhance the electrochemical performance of such layered material. Due to the wide application of layered material in batteries, electrocatalysis, and other areas, this study indicates a new avenue for the design of layered materials for electrochemical applications.

Supporting Information

Supporting Information is available from the Wiley Online Library or from the author.

Acknowledgements

Conflict of Interest

The authors declare no conflict of interest.

Keywords

[1] D. Larcher, J. M. Tarascon, *Nat. Chem.* **2015**, *7*, 19.
[2] A. Ponrouch, D. Monti, A. Boschin, B. Steen, P. Johansson, M. R. Palacin, *J. Mater. Chem. A* **2015**, *3*, 22.
[3] V. Palomares, P. Serras, I. Villaluenga, K. B. Hueso, J. Carretero-Gonzalez, T. Rojo, *Energy Environ. Sci.* **2012**, *5*, 5884.
[4] S. W. Kim, D. H. Seo, X. Ma, G. Ceder, K. Kang, *Adv. Energy Mater.* **2012**, *2*, 710.
[5] Y. You, H. Yao, S. Xin, Y. X. Yin, T. T. Zuo, C. P. Yang, Y. G. Guo, Y. Cui, L. J. Wan, J. B. Goodenough, *Adv. Mater.* **2016**, *28*, 7243.
[6] M. Fan, Y. Chen, Y. Xie, T. Yang, X. Shen, N. Xu, H. Yu, C. Yan, *Adv. Funct. Mater.* **2016**, *26*, 5019.
[7] J. Ni, S. Fu, C. Wu, J. Maier, Y. Yu, L. Li, *Adv. Mater.* **2016**, *28*, 2259.
[8] Y. Sun, L. Zhao, H. Pan, X. Lu, L. Gu, Y. S. Hu, H. Li, M. Armand, Y. Ikuhara, L. Chen, X. Huang, *Nat. Commun.* **2013**, *4*, 1870.
[9] H. Ren, J. Sun, R. Yu, M. Yang, L. Gu, P. Liu, H. Zhao, D. Wang, *Chem. Sci.* **2016**, *7*, 793.
[10] H. Ren, R. Yu, J. Wang, Q. Jin, M. Yang, D. Mao, D. Kisailus, H. Zhao, D. Wang, *Nano Lett.* **2014**, *14*, 6679.
[11] P. Senguttuvan, G. Rousse, V. Seznec, J. M. Tarascon, M. R. Palacín, *Chem. Mater.* **2011**, *23*, 4109.
[12] H. Pan, X. Lu, X. Yu, Y. S. Hu, H. Li, X. Q. Yang, L. Chen, *Adv. Energy Mater.* **2013**, *3*, 1186.
[13] G. Rousse, M. E. Arroyo-de Dompablo, P. Senguttuvan, A. Ponrouch, J. M. Tarascon, M. R. Palacín, *Chem. Mater.* **2013**, *25*, 4946.
[14] A. Rudola, K. Saravanan, C. W. Mason, P. Balaya, *J. Mater. Chem. A* **2013**, *1*, 2653.
[15] J. Xu, C. Ma, M. Balasubramanian, Y. S. Meng, *Chem. Commun.* **2014**, *50*, 12564.
[16] M. A. Muñoz-Márquez, M. Zarrabeitia, E. Castillo-Martínez, A. Eguía-Barrio, T. Rojo, M. Casas-Cabanas, *ACS Appl. Mater. Interfaces* **2015**, *7*, 7801.
[17] S. Fu, J. Ni, Y. Xu, Q. Zhang, L. Li, *Nano Lett.* **2016**, *16*, 4544.
[18] Y. Zhang, L. Guo, S. Yang, *Chem. Commun.* **2014**, *50*, 14029.
[19] C. Z. Yuan, H. B. Wu, Y. Xie, X. W. Lou, *Angew. Chem., Int. Ed.* **2014**, *53*, 1488.
[20] J. Wang, H. Tang, L. Zhang, H. Ren, R. Yu, Q. Jin, J. Qi, D. Mao, M. Yang, Y. Wang, P. Liu, Y. Zhang, Y. Wen, L. Gu, G. Ma, Z. Su, Z. Tang, H. Zhao, D. Wang, *Nat. Energy* **2016**, *1*, 16050.
[21] H. Tang, J. Wang, H. Yin, H. Zhao, D. Wang, Z. Tang, *Adv. Mater.* **2015**, *27*, 1117.
[22] J. Wang, H. Tang, H. Wang, R. Yu, D. Wang, *Mater. Chem. Front.* **2017**, *1*, 414.
[23] J. Zhang, H. Ren, J. Wang, J. Qi, R. Yu, D. Wang, Y. Liu, *J. Mater. Chem. A* **2016**, *4*, 17673.
[24] J. Qi, X. Lai, J. Wang, H. Tang, H. Ren, Y. Yang, Q. Jin, L. Zhang, R. Yu, G. Ma, Z. Su, H. Zhao, D. Wang, *Chem. Soc. Rev.* **2015**, *44*, 6749.
[25] X. Y. Yu, H. B. Wu, L. Yu, F. X. Ma, X. W. Lou, *Angew. Chem., Int. Ed.* **2015**, *54*, 4001.
[26] F. X. Ma, H. Hu, H. B. Wu, C. Y. Xu, Z. C. Xu, L. Zhen, X. W. Lou, *Adv. Mater.* **2015**, *27*, 4097.
[27] W. M. Zhang, X. L. Wu, J. S. Hu, Y. G. Guo, L. J. Wan, *Adv. Funct. Mater.* **2008**, *18*, 3941.
[28] L. Zhang, H. B. Wu, X. W. Lou, *Adv. Energy Mater.* **2014**, *4*, 1300958.
[29] T. Yang, T. Qian, M. Wang, X. Shen, N. Xu, Z. Sun, C. Yan, *Adv. Mater.* **2016**, *28*, 539.
[30] W. Stöber, A. Fink, E. Bohn, *J. Colloid Interface Sci.* **1968**, *26*, 62.
[31] L. Yu, H. B. Wu, X. W. Lou, *Adv. Mater.* **2013**, *25*, 2296.
[32] L. Cao, D. H. Chen, R. A. Caruso, *Angew. Chem., Int. Ed.* **2013**, *52*, 10986.
[33] J. F. Ni, S. D. Fu, C. Wu, Y. Zhao, J. Maier, Y. Yu, L. Li, *Adv. Energy Mater.* **2016**, *6*, 1502568.
[34] S. Chen, J. Duan, J. Ran, M. Jaroniec, S. Z. Qiao, *Energy Environ. Sci.* **2013**, *6*, 3693.
[35] A. C. Ferrari, D. M. Basko, *Nat. Nanotechnol.* **2013**, *8*, 235.
[36] A. C. Ferrari, J. Robertson, *Phys. Rev. B* **2000**, *61*, 14095.
[37] R. A. Zangmeister, T. A. Morris, M. J. Tarlov, *Langmuir* **2013**, *29*, 8619.
[38] L. Tang, Y. B. He, C. Wang, S. Wang, M. Wagemaker, B. Li, Q. H. Yang, F. Kang, *Adv. Sci.* **2017**, *4*, 1600311.
[39] M. Sathiya, A. S. Prakash, K. Ramesha, J. M. Tarascon, A. K. Shukla, *J. Am. Chem. Soc.* **2011**, *133*, 16291.
[40] V. Augustyn, J. Come, M. A. Lowe, J. W. Kim, P. L. Taberna, S. H. Tolbert, H. D. Abruña, P. Simon, B. Dunn, *Nat. Mater.* **2013**, *12*, 518.
[41] C. Zhang, X. Wang, Q. Liang, X. Liu, Q. Weng, J. Liu, Y. Yang, Z. Dai, K. Ding, Y. Bando, J. Tang, D. Golberg, *Nano Lett.* **2016**, *16*, 2054.

ADVANCED MATERIALS

Supporting Information

Na$_2$Ti$_3$O$_7$@N-Doped Carbon Hollow Spheres for Sodium-Ion Batteries with Excellent Rate Performance

Fangxi Xie, Lei Zhang, Dawei Su, Mietek Jaroniec, and Shi-Zhang Qiao*

Supporting Information

Na$_2$Ti$_3$O$_7$@N-doped Carbon Hollow Spheres for Sodium-Ion Batteries with Excellent Rate Performance

Fangxi Xie$^+$,[a] Lei Zhang$^+$,[a] Dawei Su,[b] Mietek Jaroniec,[c] and Shi-Zhang Qiao[a]*

[+] There authors contributed equally to this work.

F. Xie, Dr. L. Zhang, Prof. S. Z. Qiao
School of Chemical Engineering
The University of Adelaide
Adelaide, SA 5005 (Australia)
E-mail: s.qiao@adelaide.edu.au

Dr. D. Su,
Centre for Clean Energy Technology
Faculty of Science
University of Technology Sydney
Broadway, NSW 2007, Australia

Prof. M. Jaroniec
Department of Chemistry and Biochemistry
Kent State University
Kent, Ohio 44240 (USA)

Experimental Procedures

Synthesis of Materials

Synthesis of SiO$_2$ Spheres. Silica spheres were synthesized by the modified Stöber method:[1] 12.6 mL of tetraethyl orthosilicate (Sigma-Aldrich) were added rapidly into the mixed solution of 72 mL of ammonia (30%, Sigma-Aldrich) and 240 mL of absolute ethanol (Chem-Supply) under vigorous magnetic stirring. The as-prepared silica spheres were washed with distilled water and ethanol several times and collected by centrifugation.

Synthesis of SiO$_2$@Ti(OH)$_x$ Spheres. SiO$_2$@Ti(OH)$_x$ spheres were prepared by a slightly modified sol-gel method.[1a] 0.4 g of silica spheres were ultrasonically dispersed in a mixed solution containing 120 mL of ethanol and 1.2 mL of water. After that, 0.3 g of hydroxypropyl cellulose (average M$_w$=~80,000, Sigma-Aldrich) were added to the solution. After stirring for 30 minutes, a mixed solution of 4.0 mL of titanium butoxide (Sigma-Aldrich) and 10.0 mL of ethanol were added into the mixed solution at a rate of 1.5 mL min^{-1}. Next, the temperature of oil bath was increased to 80 ^{o}C and maintained for 100 minutes. The as-prepared SiO$_2$@Ti(OH)$_x$ was collected by centrifugation, washed with ethanol three times and redispersed ultrasonically (5 min) in 25 mL of distilled water to obtain the suspension having concentration of about 20 mg mL^{-1}.

Preparation of sodium titanate hollow spheres (Na$_2$Ti$_3$O$_7$ HSs and Na$_2$Ti$_3$O$_7$ HHSs). 10.0 mL of the as-prepared solution as described above, 2.0 mL of 5 M sodium hydroxide aqueous solution and 8.0 mL of the suitable solvent were added into a 50-ml autoclave. To prepare hollow spheres assembled from nanoparticles (Na$_2$Ti$_3$O$_7$ HSs), the solvent was ethanol; however, distilled water was used for the preparation of hollow spheres assembled from nanosheets (Na$_2$Ti$_3$O$_7$ HHSs and Na$_2$Ti$_3$O$_7$@C HHSs). After sealing, the autoclave was kept at 140 ^{o}C for 6 hours. The precipitate was washed with distilled water and ethanol several times and collected by centrifugation. After drying at 60 ^{o}C in a vacuum oven, the as-prepared hollow spheres were calcined at 500 ^{o}C for 3 hours with a ramping rate of 5 ^{o}C per minute.

Synthesis of hollow spheres assembled from carbon-coated sodium titanate nanosheets (Na$_2$Ti$_3$O$_7$@C HHSs). 50 mg of the as-prepared sodium titanate hollow spheres assembled from nanosheets were ultrasonically (30 min) dispersed in a solution containing 0.1 g of Trizma® base (Sigma-Aldrich) and 80 mL of distilled water. After that, 48 mg of dopamine hydrochloride (Sigma-Aldrich) was added rapidly into the suspension with

intense stirring. The product was washed and collected by centrifugation after 3-hour reaction at room temperature. After placing it in vacuum oven overnight, the resulting hollow spheres were calcined in a tube furnace at 500 ^{o}C for 3 hours with a ramping rate of 5 ^{o}C per minute.

Characterization

X-Ray Powder Diffraction (XRD) data were collected on Rigaku MiniFlex 600 X-Ray Diffractometer. The field-emission scanning electron microscope images were acquired on the FEI Quanta 450 FEG scanning electron microscope. The transmission electron microscope images and the high-resolution transmission electron microscope images were taken on JEOL JEM 2100F. Thermogravimetric analysis (TGA) was conducted on METTLER TOLEDO TGA/DSC 2 under air flow with a temperature ramp of 20 ^{o}C min^{-1}. Raman spectra were obtained using HORIBA LabRAM HR Evolution with the excitation wavelength of 532 nm.

Electrochemical Measurements

The electrochemical performance tests were carried out in 3025 type coin cells at room temperature. The working electrode consisted of active material (i.e., $Na_2Ti_3O_7$ HSs, $Na_2Ti_3O_7$ HHSs, $Na_2Ti_3O_7$@C HHSs), carbon black (Super P from VWR, supplied by Alfa Aesar) and binder (CMC, average M_w= ~700,000, Sigma-Aldrich) in a weight ratio of 60:30:10 with a mass loading of about 1.0 mg cm^{-2} while the copper foil was employed as the current collector. The electrolyte was composed of 1.0 M $NaClO_4$ in a mixture of ethylene carbonate and diethyl carbonate (1:1 by volume), while 1.0 M $NaClO_4$ in a mixture of ethylene carbonate and propylene carbonate (1:1 by volume) was employed in the rate performance testing. Galvanostatic tests were performed on Landt CT2001A. The cyclic voltammetry data were collected on CHI 650D electrochemical station.

Reference

[1]   L. Yu, H. B. Wu, X. W. Lou, *Adv. Mater.* **2013**, *25*, 2296; b) W. Stöber, A. Fink, E. Bohn, *J. Colloid Interface Sci.* **1968**, *26*, 62.

Supplementary Results
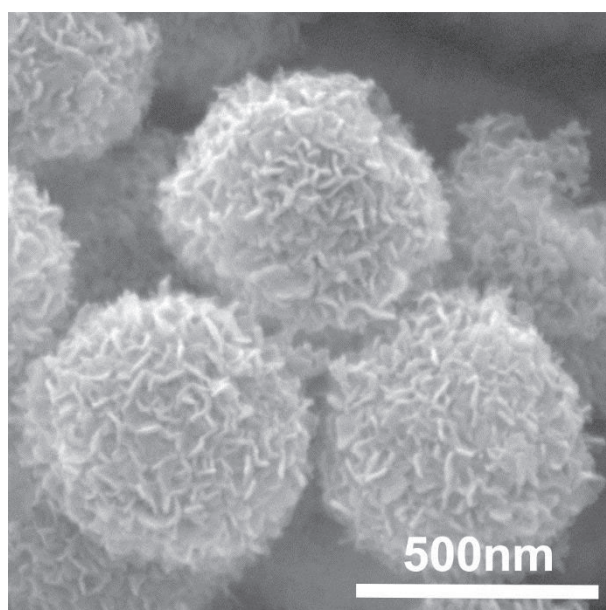
Figure S1. FESEM image of $Na_2Ti_3O_7$ HHSs.
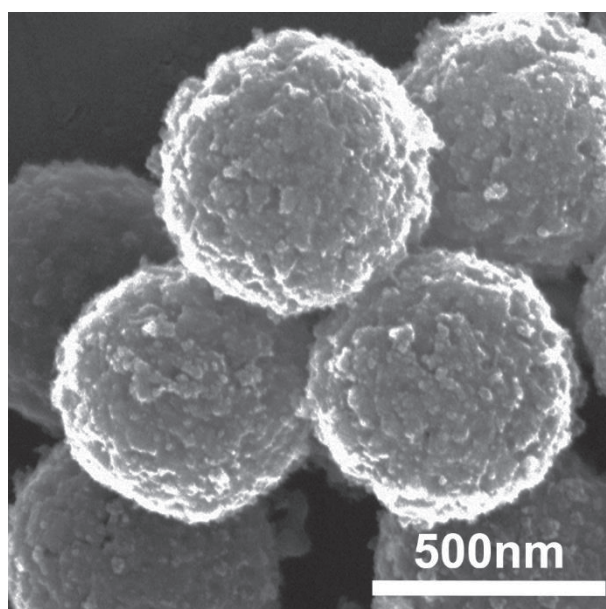
Figure S2. FESEM image of $Na_2Ti_3O_7$ HSs.
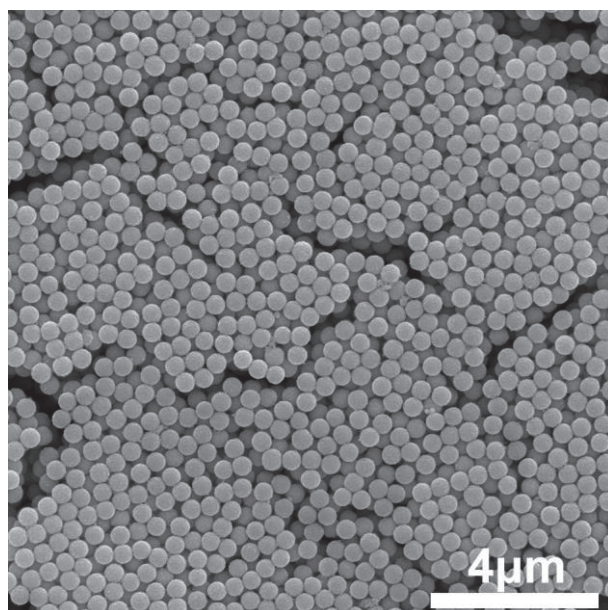
Figure S3. FESEM image of $SiO_2@Ti(OH)_x$
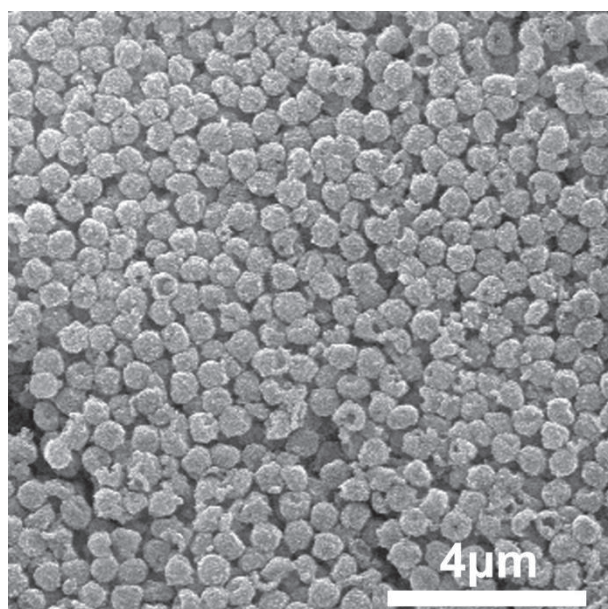
Figure S4. Low magnification SEM Image of $Na_2Ti_3O_7@C$ HHSs.
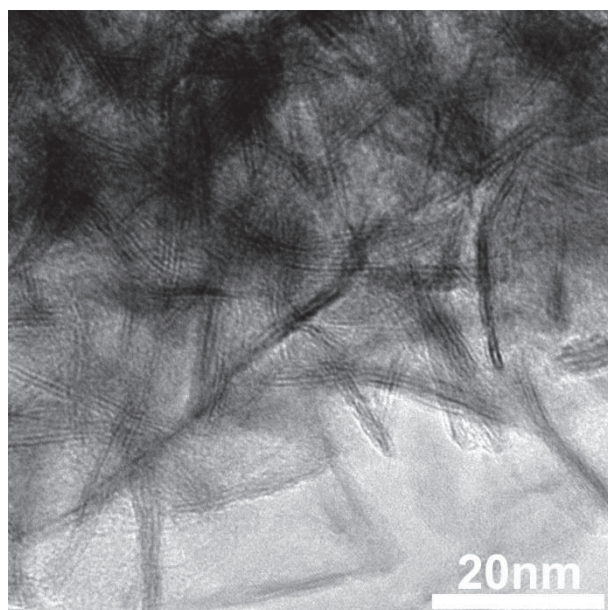
Figure S5. TEM image of $Na_2Ti_3O_7$@C HHSs.
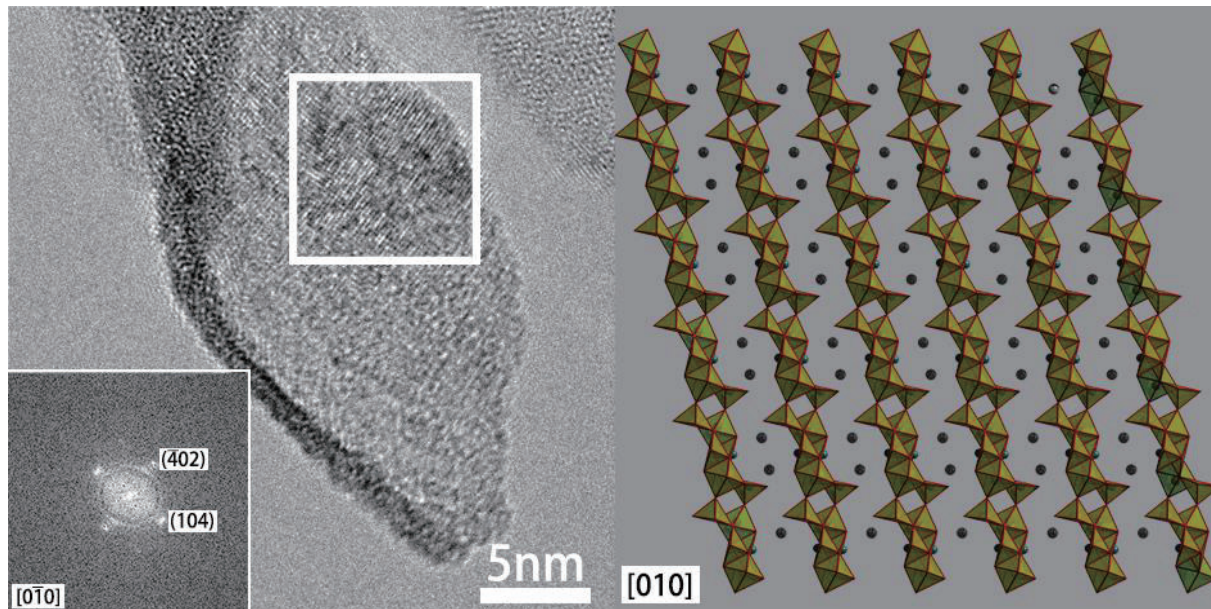
Figure S6. (Left) HRTEM image of $Na_2Ti_3O_7$ HHSs, the corresponding FFT image (inset) and (right) the scheme of the corresponding crystal structure.
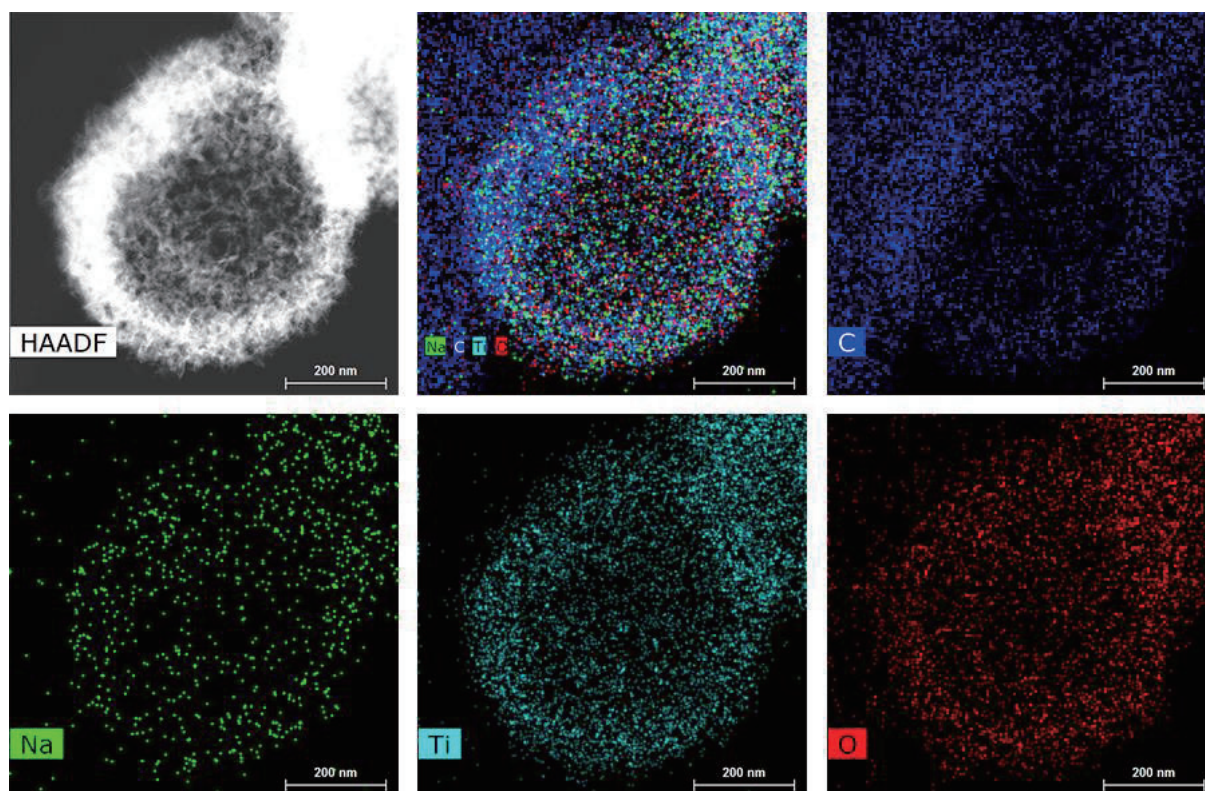
Figure S7. HAADF-STEM elemental mapping images of $Na_2Ti_3O_7@C$ HHSs.
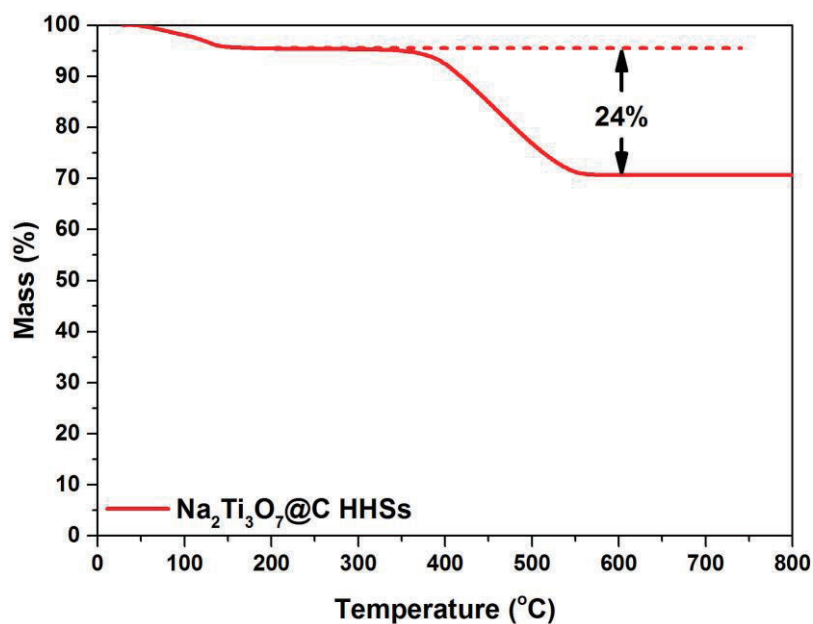
Figure S8. TGA curve of $Na_2Ti_3O_7@C$ HHSs
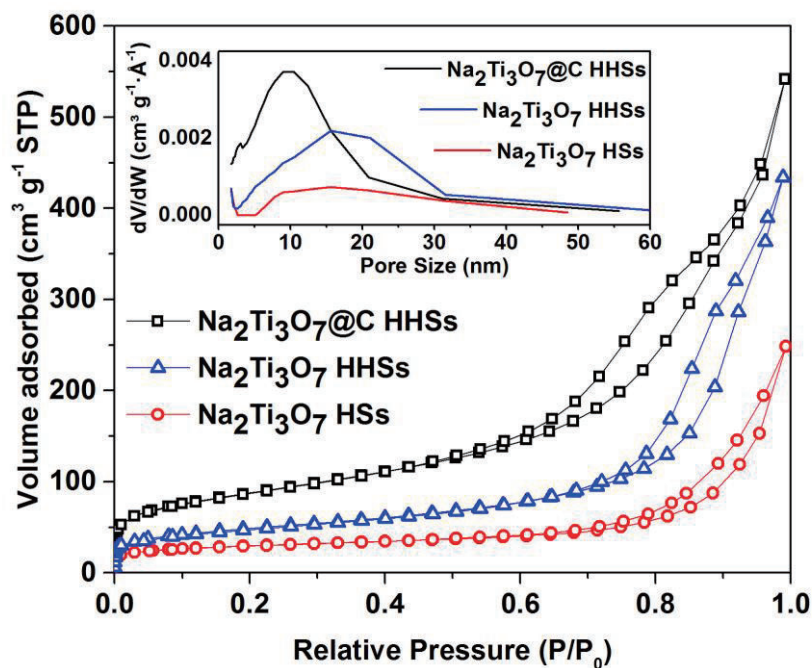
Figure S9. N_2 adsorption isotherms and (inset) the corresponding pore size distributions of the as-prepared samples.
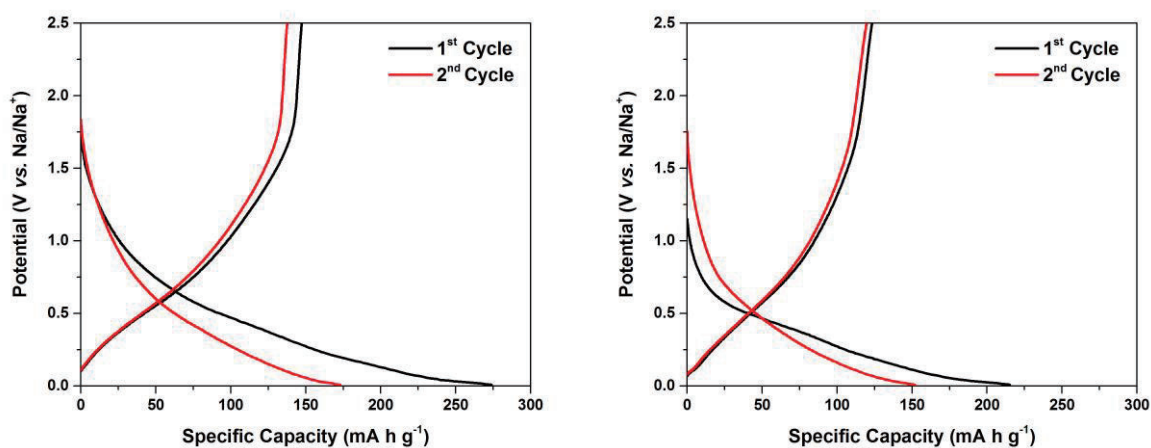
Figure S10 Initial cycles profiles obtained for $Na_2Ti_3O_7$ HHSs (left) and $Na_2Ti_3O_7$ HSs (right)
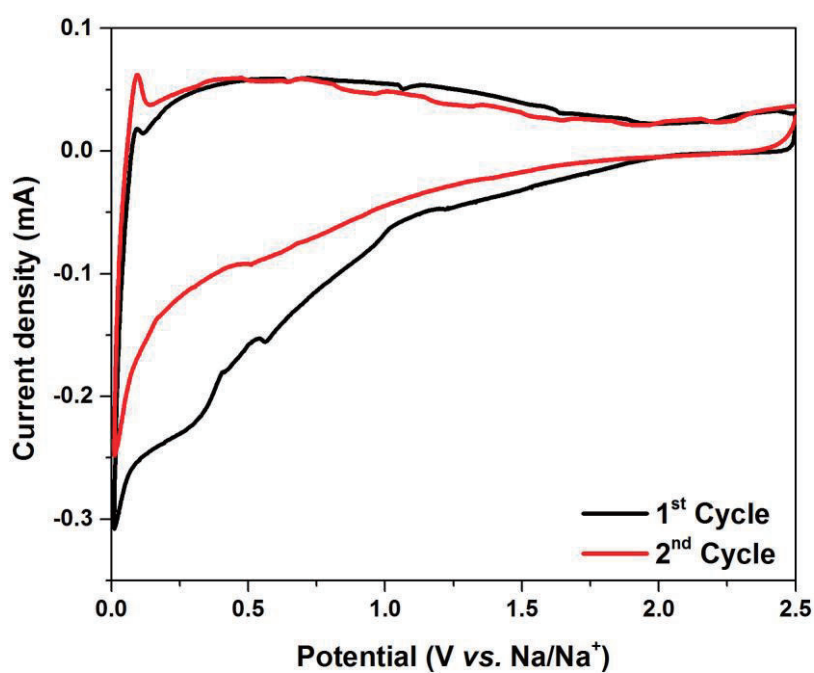
Figure S11. Initial CV profiles obtained for $Na_2Ti_3O_7$@C HHSs
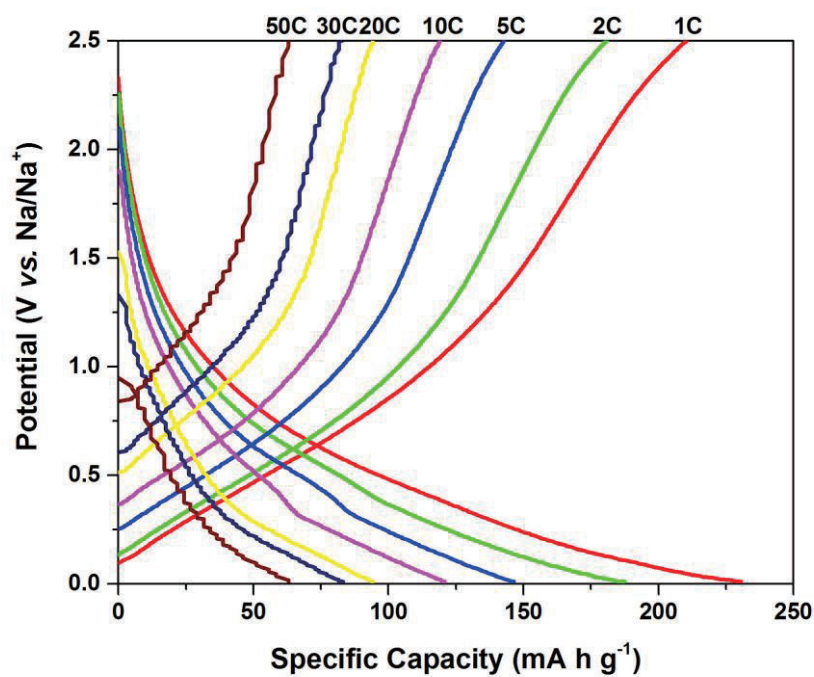
Figure S12. Various rate profiles of $Na_2Ti_3O_7$@C HHSs
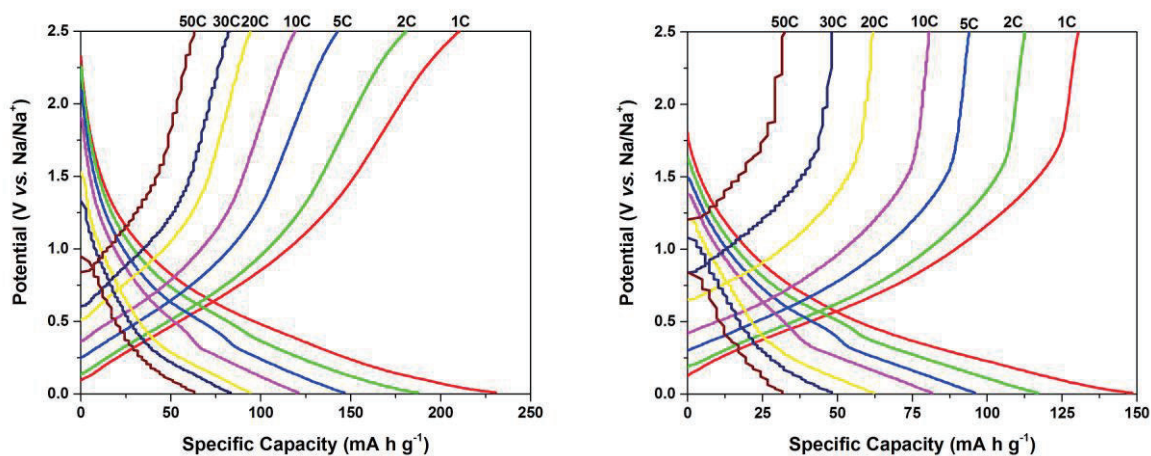
Figure S13 Various rate profiles obtained for $Na_2Ti_3O_7$ HHSs (left) and $Na_2Ti_3O_7$ HSs (right)
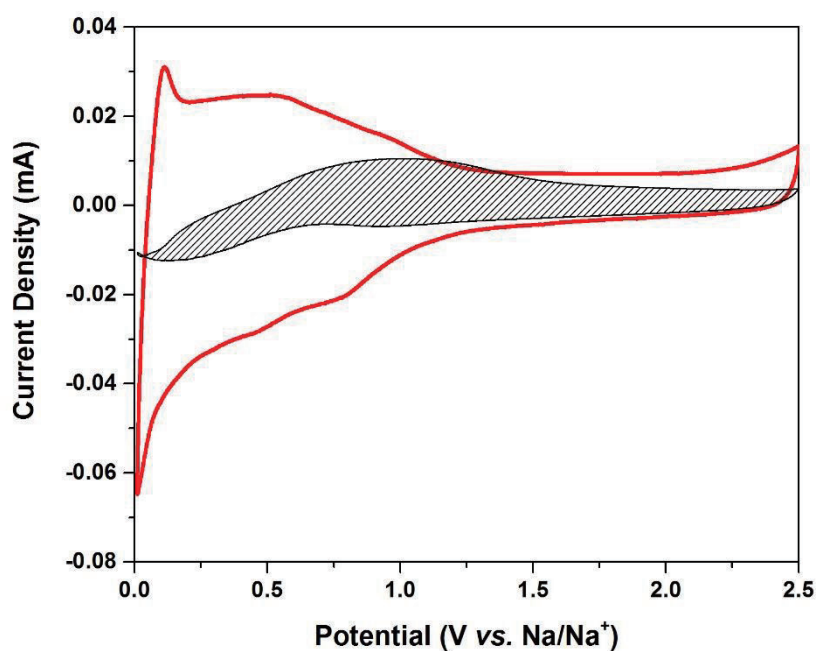
Figure S14. Red curve shows the CV curve of $Na_2Ti_3O_7$@C HHSs and the shaded region indicates the capacitive contribution measured at 0.1mV s^{-1}
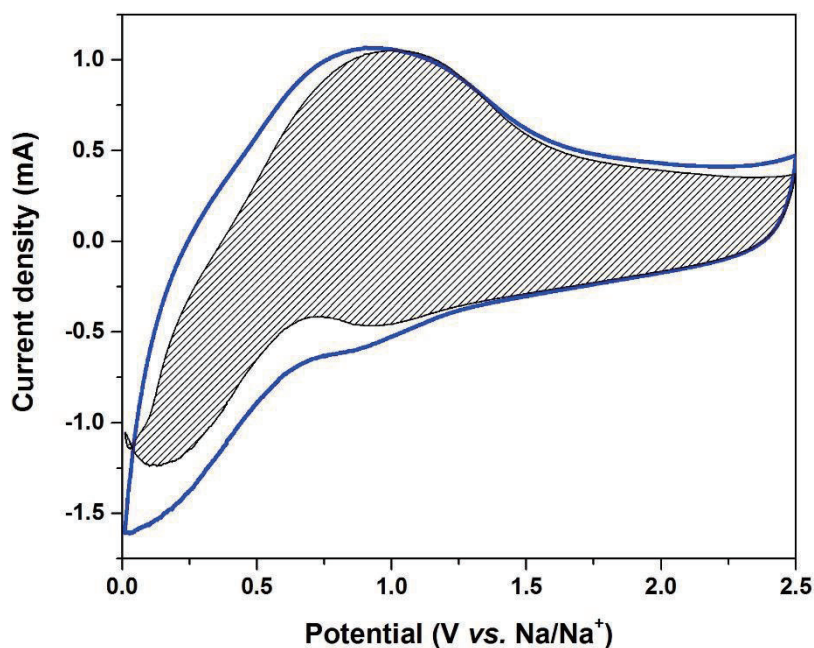
Figure S15. Blue curve shows the CV curve of $Na_2Ti_3O_7$@C HHSs and the shaded region indicates the capacitive contribution measured at 10mV s^{-1}
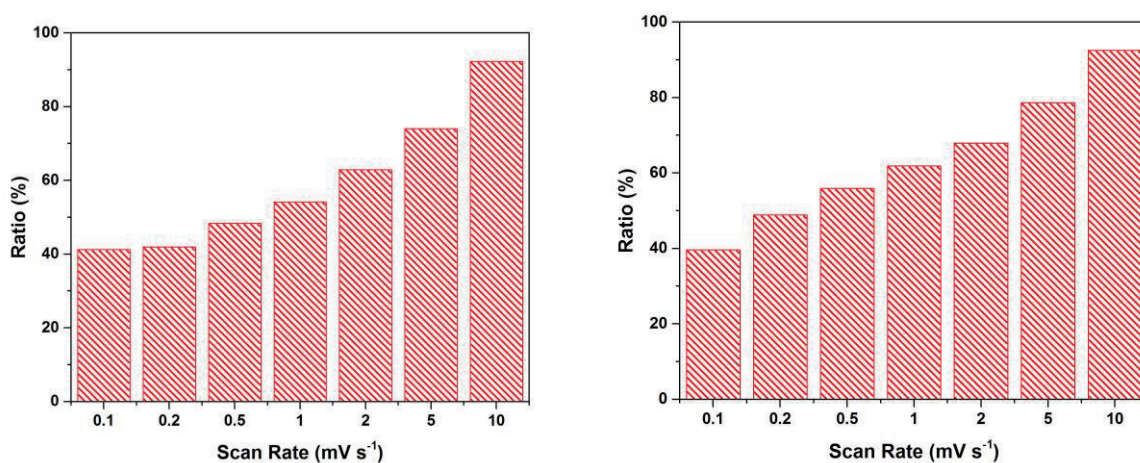
Figure S16. Diagram of the capacitive contribution to the total capacity of $Na_2Ti_3O_7$ HHSs (left) and $Na_2Ti_3O_7$ HSs (right)

Chapter 4 : Dual-Shell Titanate Cubes to Optimize Transport of Large Radii Alkali Ions

4.1 Introduction and Significance

Due to their relatively abundant content in the Earth's crust, the sodium and potassium ion batteries are considered as alternatives with much lower cost to the conventional lithium-ion batteries. However, the sodium and potassium ions are with larger ion radiuses than lithium ions. Therefore, these two sets of batteries are facing the issue of sluggish ion transportation kinetics. Herein, we report the rational design and synthesis of dual-shell structured titanate materials with optimized ion transportation on two levels.

The highlights of this work include:

1. Rational design and synthesis of dual-shell structured titanate materials
   Dual-shell materials are considered as with higher energy density and enhanced durability than their single-shell counterparts. Therefore, the dual-shell structured titanate cubes assembled from ultrathin nanosheets are constructed, considering with enhanced ion transportation on the material level.

2. Atomic understanding of the introducing of oxygen vacancies
   Several high-end spectroscopy approaches are employed to offer an atomic understanding of the introducing of oxygen vacancies. Apart from that, density functional theory calculation is also included to offer more understanding of the optimization on the atomic level.

3. A general approach to optimize ion transportation kinetics
   This structure is applied in both sodium and potassium ion batteries. It is demonstrated that this structure makes significant improvements in rate performance for both systems, demonstrating the versatility of this approach.

4.2 Dual-Shell Titanate Cubes to Optimize Transport of Large Radii Alkali Ions

This chapter is included as it appears as a journal paper published by Fangxi Xie, Lei Zhang, Yan Jiao, Anthony Vasileff, Shizhang Qiao, Dual-shell titanate cubes to optimize transport of large radii alkali ions, *to be submitted*

Statement of Authorship

Title of Paper	Dual-Shell Titanate Cubes with Dual-Level Optimized Ion Transportation for Alkaline Ions with Larger Radius
Publication Status	☐ Published ☐ Accepted for Publication ☐ Submitted for Publication ☑ Unpublished and Unsubmitted work written in manuscript style
Publication Details	Fangxi Xie, Lei Zhang, Yan Jiao, Shizhang Qiao, Dual-shell titanate cubes to optimize transport of large radii alkali ions, *to be submitted*

Principal Author

Name of Principal Author (Candidate)	Fangxi Xie
Contribution to the Paper	Research Plan, material synthesis, most of the characterizations and data analysis, electrochemical characterization, and manuscript Draft
Overall percentage (%)	60%
Certification:	This paper reports on original research I conducted during the period of my Higher Degree by Research candidature and is not subject to any obligations or contractual agreements with a third party that would constrain its inclusion in this thesis. I am the primary author of this paper.
Signature	Date 2019. May. 10.

Co-Author Contributions

By signing the Statement of Authorship, each author certifies that:

    i.   the candidate's stated contribution to the publication is accurate (as detailed above);

    ii.   permission is granted for the candidate in include the publication in the thesis; and

    iii.   the sum of all co-author contributions is equal to 100% less the candidate's stated contribution.

Name of Co-Author	Lei Zhang
Contribution to the Paper	Discussion of the research plan, synthesizing procedure and manuscript revision 10%
Signature	Date 11St of 2019

Name of Co-Author	Jiao Yan		
Contribution to the Paper	Discussion of this calculation and manuscript revision10%		
Signature		Date	11 May 2019

Name of Co-Author	Anthony Vasileff		
Contribution to the Paper	Discussion of this manuscript and manuscript revision10%		
Signature		Date	11/06/19

Name of Co-Author	Shizhang Qiao		
Contribution to the Paper	Supervision of the work, discussion of this manuscript and manuscript evaluation 10%		
Signature		Date	May 13, 2019

Please cut and paste additional co-author panels here as required.

COMMUNICATION

Dual-Shell Titanate Cubes to Optimize Transport of Large Radii Alkali Ions

Fangxi Xie, [a] Lei Zhang, [a] Yan Jiao, [a] Anthony Vasileff, [a] and Shi-Zhang Qiao*[a]

Optimizing the transport of larger ions like sodium and potassium ions is of great significance for sodium and potassium ion batteries. Herein, we rationally construct dual-shell structured titanates with oxygen vacancies to optimize ion transport. Serving as anodes for batteries, the as-prepared samples exhibit enhanced rate performance compared to samples without oxygen vacancies. This demonstrates an effective approach to optimize ion transport for enhancing rate performance.

Introduction

Lithium-ion batteries have been widely applied as electrical energy storage devices in portable electronic devices and electric vehicles.[1-4] Due to the scarcity of lithium in the Earth's crust (20 ppm), growing demand from the electric vehicle industry is significantly increasing the commodity's price.[3, 5, 6] Sodium and potassium ion batteries are considered cheaper replacements of lithium-ion batteries due to the relative abundance of sodium and potassium.[5, 7-9] However, due to their larger atomic radii, a major concern of these two new battery alternatives is the diffusion of these relatively larger ions in the electrode materials.[10, 11]

Two-dimensional layered electrode materials have been widely applied as cathodes and anodes for rocking-chair batteries.[11, 12] With close-packed layered structures, the ions can be inserted and diffused along the layers. Among these electrode materials, Ti-based layered materials have attracted great attention due to their unique properties of high activity, low cost, and environmental friendliness.[11, 13-16] Especially, due to their high energy density and capacity, layered sodium and potassium titanates show great potential as anodes for sodium and potassium ion batteries.[17-19] However, because of the larger radii of sodium and potassium ions, ion transport kinetics are generally poorer in these materials. Therefore, rational design and engineering to optimize ion transport in these layered titanate materials is highly desired.

Generally, there are two levels of optimization pertaining to ion transport kinetics: the structure level and the atomic level.[20, 21] Specifically, regarding the structure level, fabricating various nanostructures of the electrode material is one of the most common and widely applied strategies.[11] For instance when optimizing the ion transport kinetics of titanate, some reports constructed three-dimensional net-like structures and tube structures.[22-24] However, most of those as-reported optimizations ignore its unique two-dimensional layered structure. Therefore, the rational design and engineering of layered Ti-based anodes remains limited. Furthermore, on the atomic level, heteroatom-doping and vacancy introduction exhibit great improvements in enhancing the electrochemical performance of the electrodes.[22, 23] However, despite these great improvements, a deeper understanding of the performance origin remains elusive.

Herein, we report the design and synthesis of hydrogenated titanate boxes with dual-shell structures assembled from nanosheets. From electrochemical characterization, the materials exhibited excellent rate performance, demonstrating that the nanosheet building units can enhance the electrochemical performance of layered titanate anode materials. Additionally, several state-of-the-art spectroscopy techniques and density functional theory calculations were employed to offer an atomic level understanding of the origins of their improved electrochemical performance. This study demonstrates a versatile approach to enhance ion transport of larger radius ions and the performance of rocking chair batteries.

Result and discussion

The synthesis route of dual-shell sodium titanate is illustrated in Fig. 1a. Firstly, iron oxide cubes were synthesized through a reported approach.[25] As seen in Fig. S1, the as-prepared iron oxide cubes have a highly uniform size and rough surface. After that, an ultra-thin silica shell was synthesized through the coating of silica derived from the hydrolysis of tetraethyl orthosilicate and the subsequent removal of the inner iron-oxide core. Detailed morphology characterizations are shown in Fig. 1b and S2.
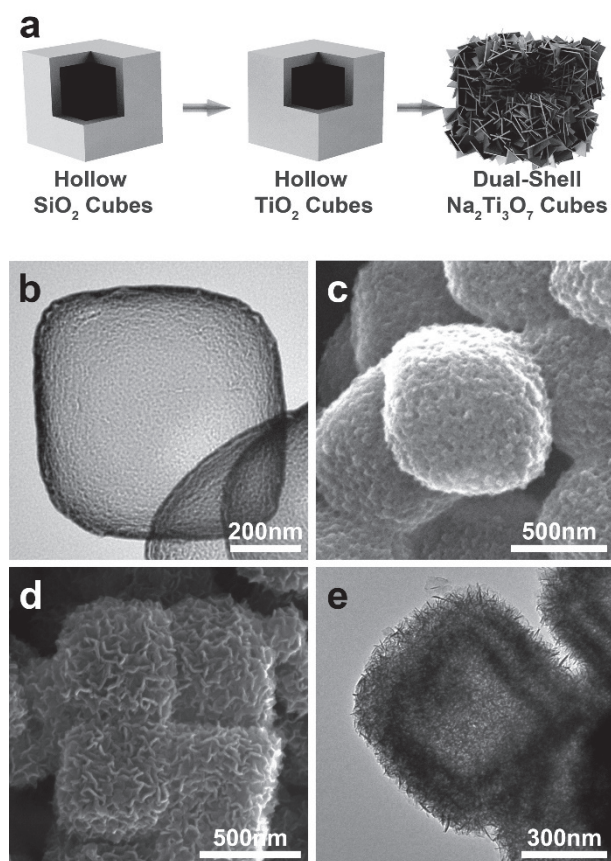
Fig. 1 a.) Scheme of the synthesis procedure of dual-shell $Na_2Ti_3O_7$ nanocubes; b.) TEM image of a silica hollow shell; c.) SEM image of titanate coated silica; d.) SEM and e.) TEM images of dual-shell $Na_2Ti_3O_7$ nanocubes.

transmission electron microscopy (TEM; Fig 1e) in which two different dark lines are found on the shell edge. It is also confirmed that both shells consist of nanosheets, which is beneficial for ion transport on the structure level.
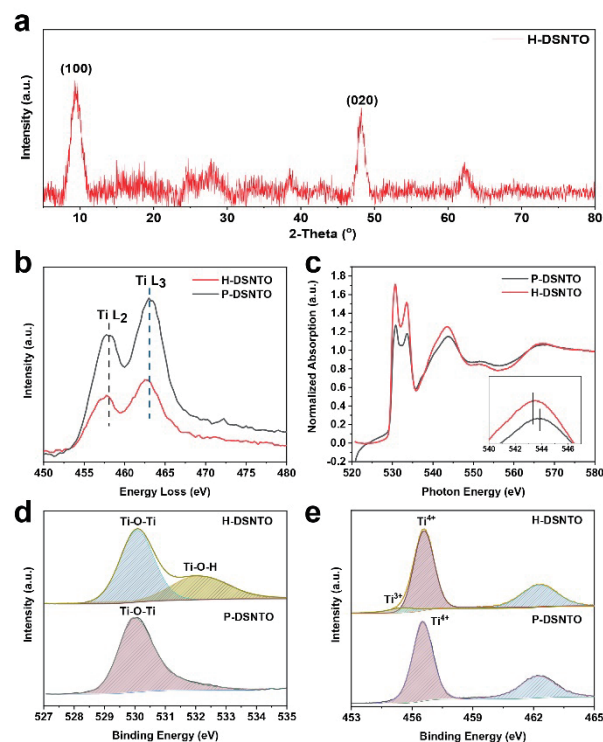

Fig. 2 a.) XRD spectrum of H-DSNTO; b.) EELS and c.) O K-edge spectra of both H-DSNTO and P-DSNTO; high-resolution XPS spectra of H-DSNTO and P-DSNTO d.) O 1s and e.) Ti 2p.

From these images, the thickness of the silica shell is tens of nanometers, demonstrating the ultrathin nature of the silica shell. Subsequently, the titanate shell was coated by a similar method reported previously (see supporting information).[11] Compared with the smooth surface of the ultrathin silica shell, the as-prepared particles have a rough surface (in Fig. 1c) indicating that the titanate layer was successfully coated on the hollow silica cubes. The ultrathin silica shell was then removed with sodium hydroxide aqueous solution to obtain titanate hollow boxes. Given the reaction of titanate and sodium hydroxide is a surface-dominated reaction, the Ti-based central mass would transfer toward the outer region to react with the sodium hydroxide, resulting in double-shell structured cubes. After calcination in an argon and hydrogen gas mixture, hydrogenated dual-shell $Na_2Ti_3O_7$ was obtained, which is denoted as H-DSNTO. Additionally, in order to make a comparison, a dual-shell sample was calcinated in pure argon and is denoted P-DSNTO.

Detailed morphology characterizations of dual-shell $Na_2Ti_3O_7$ are shown in Fig. 1d and 1e. Specifically, from scanning electron microscopy (SEM), it can be seen that the as-prepared particles are of uniform size (Fig. 1d). More importantly, many nanosheets are formed on the surface of the as-prepared particles, indicating that the cubes consists of nanosheets. Additionally, the dual-shell structure is revealed through

Apart from the morphology characterizations, various spectroscopic techniques were applied to investigate the crystal structure and electronic structure of H-DSNTO and P-DSNTO. As shown in Figure 2a, the X-Ray powder diffraction (XRPD) pattern of H-DSNTO is similar to our previous report, demonstrating that the phase of the as-prepared sample is $Na_2Ti_3O_7$.[11] Two significant peaks in the corresponding powder diffraction patterns with a two-theta angle of around 10° and 48° can be attributed to the (100) and (020) peaks of $Na_2Ti_3O_7$, demonstrating that the phase of H-DSNTO is mainly $Na_2Ti_3O_7$. From electron energy loss spectroscopy (EELS; Fig. 2b), the titanium L_2 and L_3 edges of H-DSNTO and P-DSNTO were investigated. Compared with the titanium L_2 and L_3 edges in P-DSNTO, both peaks in H-DSNTO shift to lower energy loss, indicating the presence of oxygen vacancies and enhanced conductivity of H-DSNTO. Additionally, O K-edge XANES was employed to further evaluate the impact of hydrogenation. In the O 2p region (Fig. 2c), the relatively lower delta$E$(e_g-t_{2g}) shows the partial reduction of H-DSNTO, indicating the present of oxygen vacancies and the consequent enhancement of conductivity.[26] Furthermore, X-ray photoelectron spectroscopy (XPS) was employed to evaluate the chemical differences between these two samples (Fig. S3 and S4). When comparing the high-resolution XPS O 1s spectra of both samples (Fig. 2d), H-DSNTO shows an additional peak located at 532.1 eV,

corresponding to Ti-O-H species.[23] Similar to the results mentioned above, in the high resolution Ti 2p spectra of the hydrogenated sample (Fig. 2e), there is an additional Ti^{3+} peak which appear at 455 eV. Both XPS results demonstrate the presence of oxygen vacancies in the crystal lattice of $Na_2Ti_3O_7$. To summarize, various techniques were employed to evaluate the difference between H-DSNTO and P-DSNTO. The key difference between these two samples is the presence of oxygen vacancies in H-DSNTO.
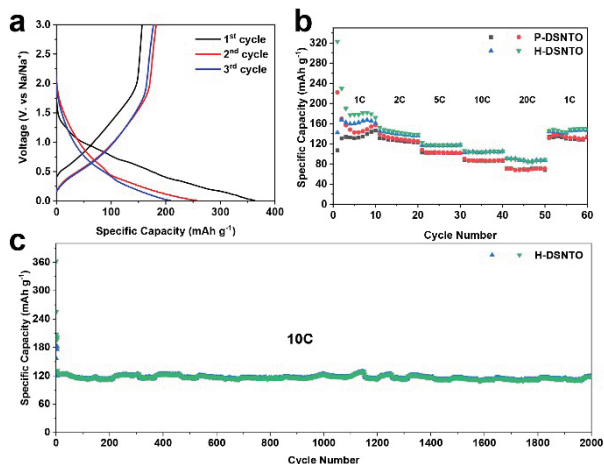

Fig. 3 a.) Initial cycle curves of H-DSNTO; b.) Comparison of rate performance of H-DSNTO and P-DSNTO; c.) Long cycling performance test of H-DSNTO.

To evaluate the impact of oxygen vacancies on electrochemical performance, both H-DSNTO and P-DSNTO were employed as anodes for sodium ion batteries. In the initial cycles as shown in Fig. 3a, H-DSNTO exhibited an initial discharge capacity of 360 mAh g^{-1} and an initial charge capacity of 163 mAh g^{-1}, corresponding with a coulombic efficiency of 45.3%. The coulombic efficiency of P-DSNTO is slightly higher (48.2%) as shown in Fig. S5. The relatively low coulombic efficiencies of H-DSNTO and P-DSNTO might originate for two reasons. Firstly, some surface functional groups may have reacted with sodium ions, causing irreversible capacity in the initial cycle. Additionally, the formation of a solid electrolyte interface (SEI) film might be another reason for the initial irreversible capacity. After the initial cycles, the rate performance of these two samples was compared. As shown in Fig.3b and Fig. S6, H-DSNTO exhibited reversible capacities of 165, 141, 116, 107 and 90 mAh g^{-1} under current densities of 1, 2, 5, 10, and 20C, respectively. On the contrary, as shown in Fig. S7, the P-DSNTO exhibited reversible capacities of 143, 126, 101, 88 and 68 mAh g^{-1} under the same current densities mentioned above. It is worth noting that H-DSNTO showed significant improvement in rate performance. Especially under high current density of 20C, H-DSNTO exhibited significantly enhanced reversible capacity of over 20 mAh g^{-1}, corresponding to over 30% increase. This improvement demonstrates that the introduction of oxygen vacancies significantly increases the rate performance of $Na_2Ti_3O_7$. Additionally, H-DSNTO also exhibited excellent durability (Fig. 3c). Initially, H-DSNTO exhibited an initial reversible capacity of 125 mAh g^{-1} under a current density of 10 C. After 2000 cycles under 10C current density, H-DSNTO

maintained reversible capacities of over 120 mAh g^{-1}, corresponding with a total capacity loss of 4%. This low capacity loss demonstrates the excellent stability of the as-prepared sample. Additionally, its stability is evidence that no significant change to the crystal lattice occurred and the oxygen vacancies might remain after long cycling.
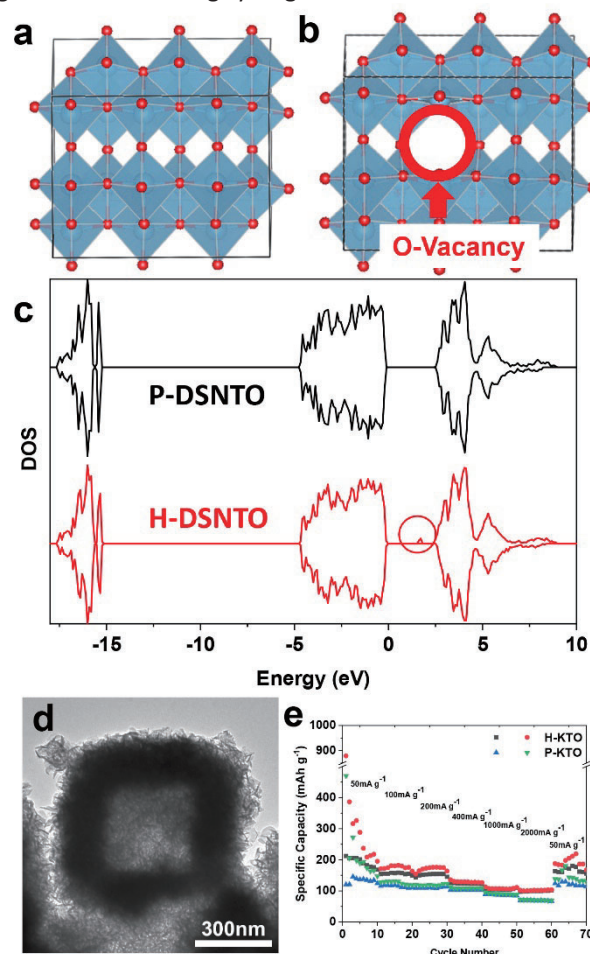

Fig. 4 The interlayer in the DFT calculation models of a.) pristine $Na_2Ti_3O_7$ and b.) $Na_2Ti_3O_7$ with oxygen vacancy; c.) Density of states of P-DSNTO and H-DSNTO; d.) TEM image as-prepared H-KTO; e.) Comparison of rate performance of H-KTO and P-KTO.

To reveal the origin of the enhanced electrochemical performance of H-DSNTO, a fundamental understanding of the impact of oxygen vacancies on the electronic structure was investigated by density functional theory (DFT) calculation. The schemes show the interlayer structures of the two models of pristine $Na_2Ti_3O_7$ (Fig. 4a) and $Na_2Ti_3O_7$ with an oxygen vacancy (Fig. 4b). As indicated in the density of states (DOS; Fig. 4c), the key difference among these two samples is some new electronic states induced by the oxygen vacancy, which results in enhanced conductivity and consequently the enhanced rate performance of H-DSNTO.[27]

To further evaluate the potential of introduced oxygen vacancies, hydrogenated potassium titanate with oxygen vacancies was synthesized through a similar synthesis procedure by simply employing potassium hydroxide to replace sodium hydroxide. In the TEM image (Fig. 4d), a similar feature

COMMUNICATION

of hollow cubes assembled with nanosheets was observed in the as-prepared samples of hydrogenated potassium titanate (denoted H-KTO, while the calcinated sample in argon is denoted P-KTO). In the evaluation of its potential to serve as an anode for potassium ion batteries, its performance under various current density was tested. Specifically, as shown in Fig. 4e, the H-KTO exhibited reversible capacities of 200, 156, 152, 126, 110, and 100 mAh g^{-1} under current densities of 50, 100, 200, 400, 1000, and 2000 mA g^{-1}, respectively. On the contrary, the P-KTO only exhibited reversible capacities of 143, 118, 108, 101, 85, and 71 mAh g^{-1} under current densities of 50, 100, 200, 400, 1000, and 2000 mA g^{-1}, respectively. From the results shown above, it can be inferred that the introduced oxygen vacancies can not only enhance the performance of sodium titanate but also improve the reversible capacity of potassium titanate, demonstrating it as a versatile approach to boost the transport of alkali metal ions.

Conclusions

In summary, this study reports the rational synthesis of dual-shell sodium titanate and potassium titanate boxes assembled from nanosheets with oxygen vacancies. As optimization at the structure level, the rationally synthesized nanosheet structures facilitate the transport of ions with larger radii. Additionally, both DFT calculations and electrochemical characterizations show that hydrogenated-induced oxygen vacancies enhance the conductivity of pristine materials, demonstrating optimization of ion transport at the atomic level. Overall, this work provides a methodology that can be applied to enhance ion transport in sodium and potassium ion batteries at both structure and atomic levels and offers novel guidance for improving the transport of larger radii ions in novel rocking chair batteries.

Conflicts of interest

The authors declare no competing financial interest.

ACKNOWLEDGMENT

Notes and references

1. M. Armand and J. M. Tarascon, *Nature*, 2008, **451**, 652-657.
2. J. M. Tarascon and M. Armand, *Nature*, 2001, **414**, 359-367.
3. D. Larcher and J. M. Tarascon, *Nat. Chem.*, 2015, **7**, 19-29.
4. M. R. Palacin, *Chem. Soc. Rev.*, 2009, **38**, 2565-2575.
5. N. Yabuuchi, K. Kubota, M. Dahbi and S. Komaba, *Chem. Rev.*, 2014, **114**, 11636-11682.
6. J. M. Tarascon, *Nat. Chem.*, 2010, **2**, 510-510.
7. H. Kim, J. C. Kim, M. Bianchini, D. H. Seo, J. Rodriguez-Garcia and G. Ceder, *Adv. Energy Mater.*, 2018, **8**, 1702384.
8. J. Y. Hwang, S. T. Myung and Y. K. Sun, *Adv. Funct. Mater.*, 2018, **28**, 1802938.
9. J. Y. Hwang, S. T. Myung and Y. K. Sun, *Chem. Soc. Rev.*, 2017, **46**, 3529-3614.
10. V. Palomares, P. Serras, I. Villaluenga, K. B. Hueso, J. Carretero-Gonzalez and T. Rojo, *Energy Environ. Sci.*, 2012, **5**, 5884-5901.
11. F. Xie, L. Zhang, D. Su, M. Jaroniec and S. Z. Qiao, *Adv. Mater.*, 2017, **29**, 1700989.
12. A. J. Perez, Q. Jacquet, D. Batuk, A. Iadecola, M. Saubanère, G. Rousse, D. Larcher, H. Vezin, M.-L. Doublet and J.-M. Tarascon, *Nat. Energy*, 2017, **2**, 954-962.
13. G. N. Zhu, Y. G. Wang and Y. Y. Xia, *Energy Environ. Sci.*, 2012, **5**, 6652-6667.
14. J. Liu, W. K. Pang, T. Zhou, L. Chen, Y. Wang, V. K. Peterson, Z. Yang, Z. Guo and Y. Xia, *Energy Environ. Sci.*, 2017, **10**, 1456-1464.
15. Y. Zhang, C. W. Foster, C. E. Banks, L. Shao, H. Hou, G. Zou, J. Chen, Z. Huang and X. Ji, *Adv. Mater.*, 2016, **28**, 9391-9399.
16. H. Pan, X. Lu, X. Yu, Y. S. Hu, H. Li, X. Q. Yang and L. Chen, *Adv. Energy Mater.*, 2013, **3**, 1186-1194.
17. C. C. Chen, J. B. Wang, Q. Zhao, Y. J. Wang and J. Chen, *ACS Energy Lett.*, 2016, **1**, 1165-1172.
18. J. Xu, C. Ma, M. Balasubramanian and Y. S. Meng, *Chem. Commun.*, 2014, **50**, 12564-12567.
19. M. A. Tsiamtsouri, P. K. Allan, A. J. Pell, J. M. Stratford, G. Kim, R. N. Kerber, P. C. M. M. Magusin, D. A. Jefferson and C. P. Grey, *Chem. Mater.*, 2018, **30**, 1505-1516.
20. Y. M. Sun, N. A. Liu and Y. Cui, *Nat. Energy*, 2016, **1**, 16071.
21. R. Bi, C. Zeng, T. Ma, A. Etogo, X. Wang and L. Zhang, *Electrochim. Acta*, 2018, **284**, 287-293.
22. J. F. Ni, S. D. Fu, C. Wu, Y. Zhao, J. Maier, Y. Yu and L. Li, *Adv. Energy Mater.*, 2016, **6**, 1502568.
23. S. Fu, J. Ni, Y. Xu, Q. Zhang and L. Li, *Nano Lett.*, 2016, **16**, 4544-4551.
24. Y. Zhang, L. Guo and S. Yang, *Chem. Commun.*, 2014, **50**, 14029-14032.
25. X. Y. Yu, H. B. Wu, L. Yu, F. X. Ma and X. W. Lou, *Angew. Chem. Int. Ed.*, 2015, **54**, 4001-4004.
26. Y. Ye, M. Kapilashrami, C. H. Chuang, Y. S. Liu, P. A. Glans and J. Guo, *MRS Communications*, 2017, **7**, 53-66.
27. T. Ling, D. Y. Yan, Y. Jiao, H. Wang, Y. Zheng, X. Zheng, J. Mao, X.-W. Du, Z. Hu, M. Jaroniec and S.-Z. Qiao, *Nat. Commun.*, 2016, **7**, 12876.

Supporting Information

Dual-shell Titanate Cubes to Optimize Transport of Large Radii Alkali Ions

Fangxi Xie,[a] Lei Zhang,[a] Yan Jiao,[a] Anthony Vasileff,[a] and Shi-Zhang Qiao*[a]

[a]School of Chemical Engineering, The University of Adelaide, Adelaide, SA 5005, Australia.

Corresponding Author: Shi-Zhang Qiao, E-mail address: s.qiao@adelaide.edu.au

Preparation of Materials

The preparation of Fe₂O₃ cubes: The Fe_2O_3 sub-microcubes were first synthesized by a previously reported method (Colloids Surf., A 1998, 134, 265; Angew. Chem. Int. Ed., 2015, 54: 4001). Typically, 50 mL of 5.4 M NaOH solution was added to the same volume of 2 M $FeCl_3$ solution in 5 min under continuous stirring at 75 °C. The resulting $Fe(OH)_3$ gels were continuously stirred at the same temperature for 5 min, and afterward aged at 100 °C in a preheated oven for 96 hours. After the reaction, the red products were collected by filtration and washed three times with deionized water and ethanol before drying in a vacuum oven overnight.

The preparation of hollow silica boxes: 1.5 g of iron oxide cubes were dispersed in a mixed solution of 130 ml ethanol and 13 ml water using ultrasonication (10 min). Subsequently, 12 ml of ammonium hydroxide solution was added in the as-prepared solution. After that, a mixed solution of 9.7 ml ethanol and 0.3 ml TEOS was added dropwise at 1.0 ml per minute under continuous stirring. After 6 hours reaction time, the sediment was collected by centrifugation. The precipitate was re-dispersed in 500 ml of 0.5 M oxalic acid to react for 18 hours at 90°C. In this time, the color of the solution turns a chartreuse yellow. All the sediments were collected by centrifugation.

The preparation of titanate coated hollow silica boxes: 30 mg of silica boxes was dispersed in a mixed solution of 120 ml of ethanol and 1.2 ml of distilled water using ultrasonication (10 min). 0.3g of hydroxypropyl cellulose (average M_w=~80,000, Sigma-Aldrich) was added to the solution. After stirring for 30 minutes, a mixed solution of 2.0 ml of titanium butoxide and 10.0 ml of ethanol were added to the mixed solution at a rate of 1.5 ml min⁻¹. Next, the temperature of the oil bath was increased to 80 °C and maintained for 100 minutes. The as-prepared titanate coated hollow silica boxes were collected by centrifugation and washed with ethanol three times.

Preparation of sodium titanate dual-shell structured boxes: The as-prepared titanate coated hollow silica boxes were re-dispersed ultrasonically in 19 ml of distilled water. This as-prepared suspension was added to a 50 ml autoclave with an additional 1.0 ml of 5 M sodium hydroxide aqueous solution. After sealing, the autoclave was kept at 120 °C in a

preheated oven for 6 hours. Finally, the as-prepared sample was collected by centrifugation and washed with ethanol three times.

Characterization

X-Ray Powder Diffraction (XRD) spectra were collected on Rigaku MiniFlex 600 X-Ray Diffractometer. The field-emission scanning electron microscope (SEM) images were acquired on a FEI Quanta 450 FEG scanning electron microscope. The transmission electron microscope (TEM) images and the high-resolution transmission electron microscope (HRTEM) images were taken on JEOL JEM 2100F. X-ray photoelectron spectroscopy (XPS) measurements were conducted on a X-ray microprobe from Thermo (Escalab 250Xi) with monochromatic Al Kα radiation. The synchrotron-based XANES measurements were carried out on the soft X-ray spectroscopy beamline at the Australian Synchrotron, which is equipped with a hemispherical electron analyzer and a microchannel plate detector that enables simultaneous recording of the total electron yield and partial electron yield.

Electrochemical Measurements

The electrochemical performance tests were carried out in 3025 type coin cells at room temperature. The working electrode consisted of active material (i.e., P-DSNTO, H-DSNTO), carbon black (Super P from VWR, supplied by Alfa Aesar) and binder (CMC, average M_w= ~700,000, Sigma-Aldrich) in a mass ratio of 60:30:10 and a mass loading of about 1.0 mg cm^2, while copper foil was employed as the current collector. The electrolyte was composed of 1.0 M $NaClO_4$ in a mixture of ethylene carbonate and diethyl carbonate (1:1 by volume) with 5% Fluoroethylene carbonate. Galvanostatic tests were performed on a Landt CT2001A.

Computational Details

Density functional theory calculations were performed using the Vienna Ab Initio Simulation Package (VASP).[1] The exchange-correlation interaction was described by generalized gradient approximation (GGA) with the Perdew-Burke-Ernzerhof (PBE) functional.[2] The Monkhorst-Pack k-point mesh was set to 2 × 3 × 4. The convergence criteria on the total energy for each ionic step was set to be 1.2×10^{-5} eV. Atoms were

relaxed until the residual forces were less than 0.01 eV Å^{-1} in each system. For the density of state calculations, the k-points was set to be $6 \times 9 \times 12$.
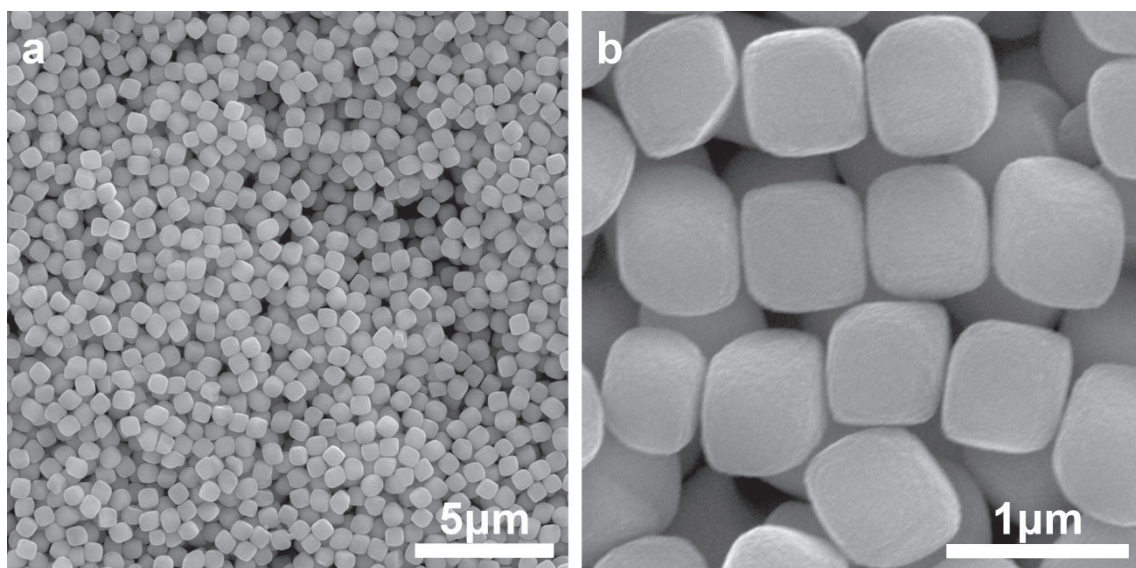
Supporting Figures:

Fig. S1 SEM images of iron oxide cubes at different magnifications: a) low magnification; b) high magnification.
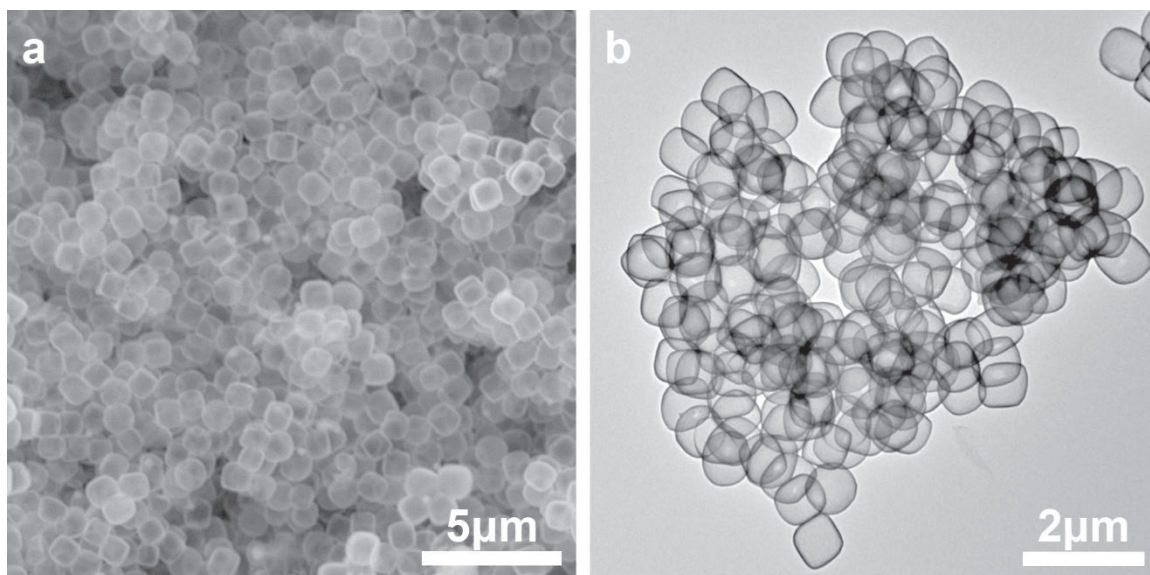

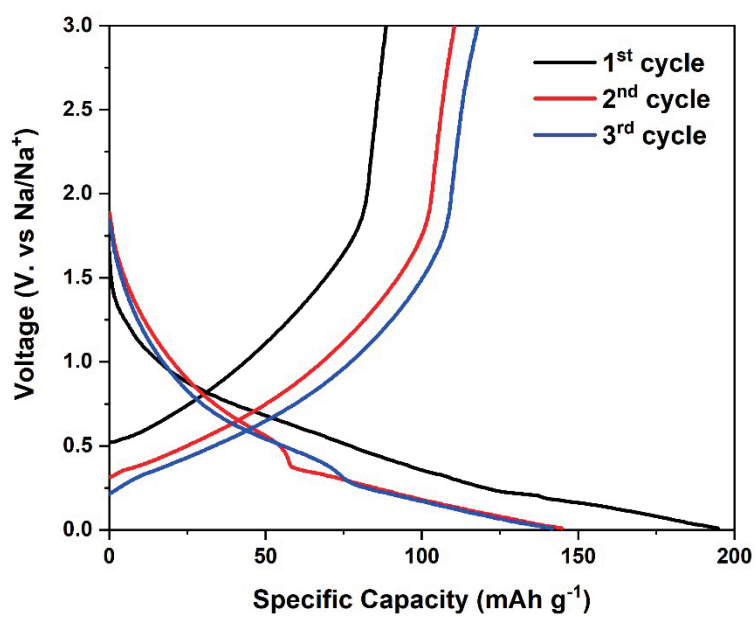Fig. S2 a) SEM image, b) TEM image of hollow silica cubes with ultrathin shells.
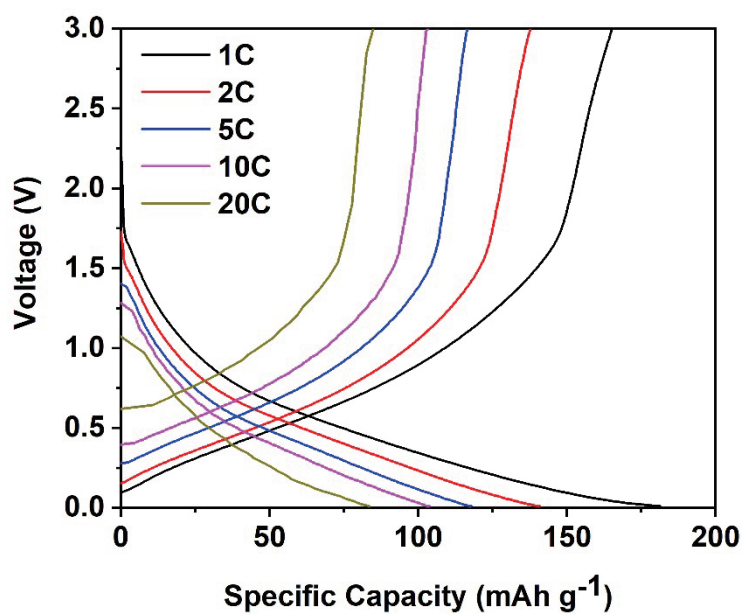
Fig. S3 XPS survey spectrum of H-DSNTO.

Fig. S4 XPS survey spectrum of P-DSNTO.

Fig. S5 Initial cycle curves of P-DSNTO.

Fig. S6 Discharging and charging curves of H-DSNTO under various current densities.
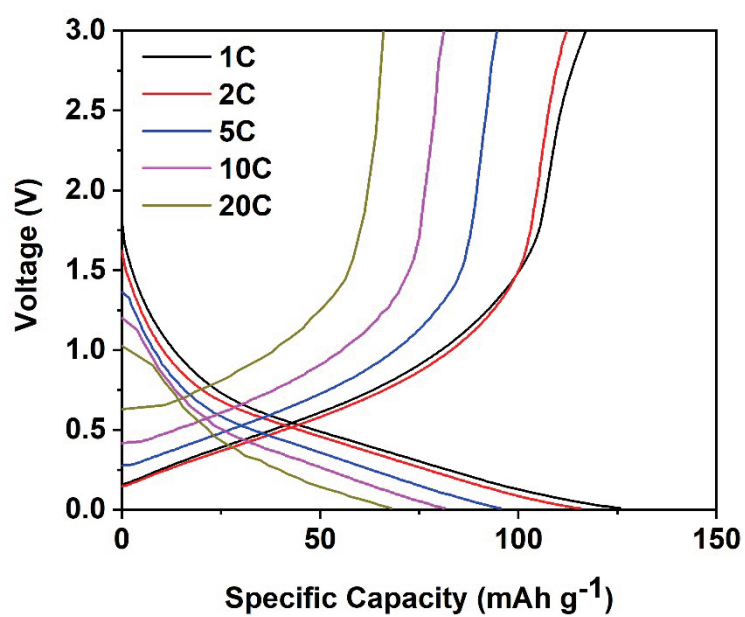
Fig. S7 Discharging and charging curves of P-DSNTO under various current densities.

Supplementary References

[1]   G. Kresse, J. Furthmüller, *Phys. Rev. B* **1996**, 54, 11169-11186.

[2]   J. P. Perdew, *Phys. Rev. Lett.* **1996**, 77, 3865-3868.

Chapter 5 : Multi-Shell Hollow Structured Sb₂S₃ for Sodium-Ion Batteries with Enhanced Energy Density

5.1 Introduction and Significance

Low energy density is the key barrier for sodium ion batteries. Simple hollow structures with large inward voids enable to accommodate the volume expansion and offer high gravimetric energy density. However, the large inward voids significantly decrease the volumetric energy density. Thus, even though high gravimetric energy density can be achieved due to the hollow structure, it is a great challenge to achieve high volumetric energy density in hollow structure. Here, multi-shell antimony sulfide (Sb_2S_3) particles were successfully synthesized. As compared with the single-shell counterparts, the multi-shell structured hollow Sb_2S_3 exhibited higher volumetric energy density and enhanced durability. Additionally, this unique multi-shell structured material exhibited enhanced gravimetric energy density than the pristine Sb_2S_3. *Operando* synchrotron-based powder diffraction was employed to reveal that the origin of high gravimetric energy density is the more complete conversion reaction thanks to the novel structure. And the proposed mechanism points out an important direction for the future development of sodium anodes.

The highlights of this work include:

1. **Hollow structured Sb₂S₃ with higher volumetric energy density**

   Hollow structured Sb_2S_3 can offer enhanced electrochemical reactivity and consequently, high gravimetric energy density. However, the large inward voids also decrease the volumetric energy density. Multi-shell hollow structured Sb_2S_3 with complex internal feature is synthesized, which not only maintains the high electrochemical reactivity but exhibits enhanced volumetric energy density.

2. **Enhanced sodium storage performance and durability**

   The multi-shell sample delivered high reversible capacity of over 600 mAh g^{-1} under the current density of 2000 mA g^{-1}, which is about three times of that of the pristine Sb_2S_3. As compared with its single-shell counterparts, the multi-shell sample exhibited high reversible capacity of over 500 mAh g^{-1} under the current density of 1000 mA g^{-1} after

50 cycles, while the single-shell sample could only deliver about 200 mAh g^{-1}, demonstrating the enhanced durability of the former due to the complex internal feature.

3. Convincing mechanism

Due to the ultra-small size nature of products from electrochemical reaction, the impact of structure on the electrochemical reactions remains elusive. With the high intensity and consequently, excellent time-resolution, synchrotron-based *operando* powder diffraction was employed to confirm the enhanced electrochemical reactivity of multi-shell samples via comparison of the *operando* powder diffraction patterns.

5.2 Multi-shell hollow structured Sb$_2$S$_3$ for sodium-ion batteries with enhanced energy density

This chapter is included as it appears as a journal paper published by Fangxi Xie, Lei Zhang, Qinfen Gu, Dongliang Chao, Mietek Jaroniec, Shizhang Qiao, Multi-shell hollow structured Sb$_2$S$_3$ for sodium-ion batteries with enhanced energy density, ***Nano Energy***, 2019, 591-599.

Statement of Authorship

Title of Paper	Multi-Shell Hollow Structured Sb$_2$S$_3$ for Sodium-Ion Batteries with Enhanced Energy Density
Publication Status	☑ Published ☐ Accepted for Publication ☐ Submitted for Publication ☐ Unpublished and Unsubmitted work written in manuscript style
Publication Details	Fangxi Xie, Lei Zhang, Qinfen Gu, Dongliang Chao, Mietek Jaroniec, Shizhang Qiao, Multi-shell hollow structured Sb$_2$S$_3$ for sodium-ion batteries with enhanced energy density, Nano Energy, 2019, 591-599.

Principal Author

Name of Principal Author (Candidate)	Fangxi Xie
Contribution to the Paper	Research Plan, material synthesis, most of the characterizations and data analysis, electrochemical characterization, and manuscript Draft
Overall percentage (%)	60%
Certification:	This paper reports on original research I conducted during the period of my Higher Degree by Research candidature and is not subject to any obligations or contractual agreements with a third party that would constrain its inclusion in this thesis. I am the primary author of this paper.
Signature	Date 2019. May. 10.

Co-Author Contributions

By signing the Statement of Authorship, each author certifies that:

    i.   the candidate's stated contribution to the publication is accurate (as detailed above);

    ii.   permission is granted for the candidate in include the publication in the thesis; and

    iii.   the sum of all co-author contributions is equal to 100% less the candidate's stated contribution.

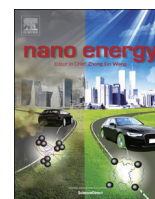| Name of Co-Author	Lei Zhang
Contribution to the Paper	Design of research plan, discussion of synthesizing procedure and manuscript revision 15%
Signature	Date 11St of 2019

Name of Co-Author	Qinfen Gu
Contribution to the Paper	Discussion of Operando powder diffraction characterization 5%
Signature		Date	12end 05 2019

Name of Co-Author	Dongliang Chao
Contribution to the Paper	Discussion of this manuscript and manuscript revision 5%
Signature		Date	11st. 05, 2019.

Name of Co-Author	Mietek Jaroniec
Contribution to the Paper	Discussion of this manuscript and manuscript revision 5%
Signature		Date	May 12, 2019

Name of Co-Author	Shizhang Qiao
Contribution to the Paper	Supervision of the work, discussion of this manuscript and manuscript evaluation 10%
Signature		Date	May 13, 2019

Please cut and paste additional co-author panels here as required.

Full paper

Multi-shell hollow structured Sb_2S_3 for sodium-ion batteries with enhanced energy density

Fangxi Xie[a], Lei Zhang[a], Qinfen Gu[b], Dongliang Chao[a], Mietek Jaroniec[c], Shi-Zhang Qiao[a,d,*]

[a] *School of Chemical Engineering, The University of Adelaide, Adelaide, SA, 5005, Australia*
[b] *Australian Synchrotron (ANSTO), 800 Blackburn Rd, Clayton, VIC, 3168, Australia*
[c] *Department of Chemistry and Biochemistry, Kent State University, Kent, OH, 44240, USA*
[d] *School of Materials Science and Engineering, Tianjin University, Tianjin, 300072, PR China*

ABSTRACT

Low energy density is the key issue that needs to be addressed for sodium ion batteries. Antimony sulfide (Sb_2S_3) with high theoretical capacity is considered as an ideal anode, but it suffers from poor electrochemical activity and consequently, low energy density. Simple hollow Sb_2S_3 structures with high electrochemical activity offer high gravimetric energy density, while large internal voids significantly decrease the volumetric energy density. Here, multi-shell Sb_2S_3 was synthesized as an anode for sodium ion batteries, exhibiting much higher reversible capacity and gravimetric energy density than the pristine Sb_2S_3. Moreover, the multi-shell structure presents higher volumetric energy density with enhanced durability than its single-shell counterpart due to the optimized utilization of the inner void. *Operando* synchrotron-based X-ray powder diffraction (XRPD) was used to verify the enhanced electrochemical activity originated from more complete conversion electrochemical reactions. The multi-shell Sb_2S_3 design may provide a guide for the development of high-performance hollow structured anodes with preserved high energy density.

1. Introduction

Sodium ion batteries (SIBs) are considered as alternatives for lithium ion batteries (LIBs) due to the significantly reduced price [1–9]. However, due to the higher equivalent weight of Na than Li and the relatively lower cathode voltages of SIBs than LIBs, SIBs usually suffer from the low energy density [5–10]. To improve their low energy density, including volumetric energy density and gravimetric energy density, is the key for the practical applications of sodium ion batteries [2,4,5,10–15]. Linked directly with high energy density, the specific capacity is considered as the most critical evaluation criterion for electrodes [9,16,17]. Thus, with the aim to improve the energy density of sodium ion batteries, one of the most important approaches is the preparation of suitable electrodes with high specific capacity [4,7,9,18–20]. Compared to the intercalation mechanism based on the reversible insertion/extraction of sodium ions, the alloying and conversion anodes are considered more appealing due to their much higher theoretical specific capacity [9,19,21–25]. As a typical anode material with both alloying and conversion sodium-ion storage mechanisms, Sb_2S_3 with a high theoretical capacity of 946 mAh g^{-1} is considered as one of the most ideal anodes for sodium ion batteries [26–30].

However, one of the major issues is that Sb_2S_3-based anodes can only deliver limited reversible capacity, indicating their poor electrochemical activity [27,30,31]. This poor electrochemical activity can be mainly attributed to the poor electrical conductivity due to the formation of electrochemical reaction intermediate Na_2S with poor electrical conductivity and the sluggish ionic diffusion of relatively larger sodium ions in Sb_2S_3 [5,20,26]. Therefore, a limited reversible capacity associated with low gravimetric energy density have been reported so far. It remains a challenge to develop Sb_2S_3 with enhanced electrochemical activity and high reversible capacity and, consequently, high energy density [27,29].

Various nanostructures were synthesized to improve the electrochemical activity of Sb_2S_3, *e.g.,* one-dimensional nanorods and flower-like spheres assembled by nanosheets [27,29,30]. Those nanostructures featured shorten diffusion lengths and enhanced electrochemical activity, resulting in higher gravimetric energy density [29,30]. As regards to the energy density, two types of this quantity are considered, i.e., the gravimetric energy density and the volumetric energy density [12,13,17,32,33]. With the enhanced electrochemical activity, the gravimetric energy density of the aforementioned nanostructured Sb_2S_3 is quite decent, while it made a huge compromise on the volumetric

* Corresponding author. School of Chemical Engineering, The University of Adelaide, Adelaide, SA, 5005, Australia.
E-mail address: s.qiao@adelaide.edu.au (S.-Z. Qiao).

energy density [13,34,35]. Thus, the nanostructured Sb_2S_3 is considered as a low volumetric energy density material [34,35]. To overcome this issue, the hollow micrometer-sized particles with suppressed diffusion length of thin functional shell and enhanced contact with electrolyte due to the relatively large surface area, are considered as optimized structures with enhanced electrochemical activity and preserved volumetric energy density [36–38]. According to the previous reports, both the hollow structured SnS_2 and carbon microspheres exhibited superior rate performance, indicating an improved electrochemical activity of sodium ion anodes with hollow design [21,39–41]. Even though the direct evidence for boosting electrochemical activity remains elusive, the previous reports suggest that the application of hollow structures may afford Sb_2S_3 with enhanced electrochemical activity and consequently, high reversible capacity. Whereas, the large internal voids in hollow structures would significantly decrease the volumetric energy density [13,36–38,42,43]. Challenge remains in achieving high volumetric energy density in hollow Sb_2S_3 structures.

Herein, we firstly report the design of multi-shell Sb_2S_3 structures obtained from the metal-organic frameworks (MOFs) templates. It is suggested that the micrometer-sized multi-shell hollow Sb_2S_3 structures with better utilization of large internal voids can be considered as unique structures to achieve high volumetric energy density but remain high gravimetric energy density of hollow structure. Multi-shelled antimony sulfide used as an anode in sodium ion batteries exhibits an enhanced reversible gravimetric capacity and higher volumetric energy density than the pristine and single-shell hollow counterparts. Additionally, the inner shells provide extra support for the outer shell, benefiting the long-term durability of the multi-shelled hollow anodes. Furthermore, the mechanism of the enhanced electrochemical activity of multi-shelled hollow structures is revealed by synchrotron-based *operando* X-ray powder diffraction technology.

2. Experiment

2.1. Materials synthesis

Synthesis of zeolitic imidazolate framework 8 (ZIF-8): The synthesis of ZIF-8 was performed as reported elsewhere [44,45]. First, 0.734 g of zinc nitrate hexahydrate was dissolved in 50 mL of methanol. On the other hand, another solution was prepared by dissolving 0.81 g of 2-methylimidazole and 0.5 g of 1-methylimidazole in 50 mL of methanol. The latter solution was poured into the former one under magnetic stirring, which was stopped as soon as the two solutions were combined. After aging for 24 h, the precipitate was collected by centrifugation, washed with methanol and then dried overnight at 60 °C in a vacuum oven.

Synthesis of multi-shell Sb_2S_3: 40 mg of the as-prepared ZIF-8 was transferred into a round bottom flask and dispersed in 30 mL of anhydrous ethanol under ultrasonication for 10 min. The flask was soaked into 95 °C oil bath. After that, a mixed-solution of 0.72 g thioacetamide and 10 mL of anhydrous ethanol were added into the flask and the whole reaction was processed under 95 °C for half hour. The intermediate was collected by centrifugation and washed with anhydrous ethanol. Afterward, the intermediate was redispersed in the flask having 30 mL of anhydrous ethanol as a solvent under ultrasonication. A similar process with 0.5-h refluxing and collection process was repeated to create another shell. After another 1.5-h reflux process, the as-obtained sample was collected and washed with anhydrous ethanol twice. After that, the as-prepared sample was redispersed in 20 mL of anhydrous ethanol while another solution was prepared by dissolving 40 mg of antimony chloride in 20 mL of anhydrous ethanol. The former solution was poured into the latter one under magnetic stirring, which was stopped after 2 h. The product was collected and washed with ethanol three times.

Synthesis of single-shell Sb_2S_3: 40 mg of the as-prepared ZIF-8 was transferred into a round bottom flask and dispersed in 30 mL of

anhydrous ethanol under ultrasonication for 10 min. The flask was soaked into 120 °C oil bath. After that, a mixed-solution of 2.0 g thioacetamide and 20 mL of anhydrous ethanol was injected into the flask and the whole reaction was processed under 120 °C for 3 h. After the reflux process, the as-obtained sample was collected and washed with anhydrous ethanol twice. After that, the as-prepared sample was redispersed in 20 mL of anhydrous ethanol while another solution was prepared by dissolving 40 mg of antimony chloride in 20 mL of anhydrous ethanol. The former solution was poured into the latter one under magnetic stirring, which was stopped after 2 h. The product was collected and washed with ethanol three times.

Synthesis of core-shell Sb_2S_3: 40 mg of the as-prepared ZIF-8 was transferred into a round bottom flask and dispersed in 30 mL of anhydrous ethanol under ultrasonication for 10 min. The flask was soaked into 95 °C oil bath. After that, a mixed-solution of 0.72 g thioacetamide and 10 mL of anhydrous ethanol was added into the flask and the whole reaction was processed at 95 °C for half hour. The intermediate was collected by centrifugation and washed with anhydrous ethanol. After washing, the intermediate was redispersed in the flask under ultrasonication with 30 mL of anhydrous ethanol as a solvent. After another 2.5-h reflux process, the as-obtained sample was collected and washed with anhydrous ethanol twice. After that, the as-prepared sample was redispersed in 20 mL of anhydrous ethanol while another solution was prepared by dissolving 40 mg of antimony chloride in 20 mL of anhydrous ethanol. The former solution was poured into the latter one under magnetic stirring, which was stopped after 2 h. The product was collected and washed by ethanol three times.

Synthesis of Sb_2S_3 nanowire: About 0.135 g of antimony potassium tartrate, 0.021 g of sulfur powder and 0.2 g of citric acid were dispersed in 8 mL of water in a 50 mL Teflon-lined autoclave. After 2 min stirring, 20 mL of ethylene glycol was added. After stirring for 40 min and injecting 2 mL of hydrazine hydrate, the autoclave was placed and maintained at 180 °C in an oven for 8 h. After cooling down to room temperature, the product was collected by centrifugation and washed with distilled water twice and ethanol once. Eventually, the product was dried overnight at 80 °C in an oven.

2.2. Materials characterization

X-Ray powder diffraction (XRPD) data were collected on Rigaku MiniFlex 600 X-Ray Diffractometer. The field-emission scanning electron microscope (SEM) images were acquired on the FEI Quanta 450 FEG scanning electron microscope. The transmission electron microscope (TEM) images were taken on FEI Tecnai G2 Spirit. The scanning transmission electron microscope (STEM) and high-resolution transmission electron microscope (HRTEM) images were taken on FEI Titan Themis. The *operando* XRPD was conducted in the Powder Diffraction (PD) beamline of Australian Synchrotron (ANSTO) with a beamline wavelength of 0.6525 Å. The surface area was evaluated from nitrogen adsorption data measured at 77.3 K (ASAP 2020) using the Brunauer–Emmett–Teller (BET) method.

2.3. Electrochemical measurements

The electrochemical performance tests were carried out in 2032 type coin cells at room temperature. All the active materials were calcined at 300 °C for 2 h to enhance the crystallinity. The working electrode consisted of active material (i.e., multi-shell Sb_2S_3, single-shell Sb_2S_3 and pristine Sb_2S_3), carbon black (Super P from VWR, supplied by Alfa Aesar) and binder polyvinylidene fluoride (PVDF) in a weight ratio of 60:30:10, while the copper foil was employed as the current collector. The loading mass of the electrode material is around 1.0–1.4 mg cm^{-2}. The electrolyte was composed of 1.0 M $NaCF_3SO_3$ dissolved in diglyme. Galvanostatic tests were performed on Landt CT2001A battery testing system. The cyclic voltammetry (CV) data were collected on CHI 650D electrochemical station.
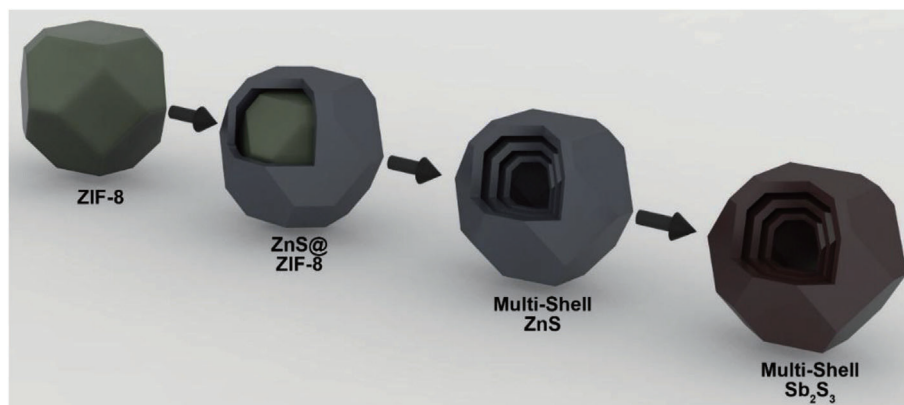
Fig. 1. Scheme illustrating the synthesis route from ZIF-8 to multi-shell Sb₂S₃.

3. Results and discussion

The synthesis procedure of the multi-shell Sb₂S₃ is illustrated in Fig. 1. First, the designed framework and chemical instability of metal-organic frameworks offer feasibility toward their conversion to the desired structures by chemical reaction with certain reagents. Inspired by that, the ZIF-8 particles having shape of truncated octahedrons and uniform particle size of 2 μm were synthesized using a slightly modified strategy reported elsewhere [44–46]. The solid structure of the original ZIF-8 particles is verified by TEM image in Fig. S1. Multi-shell structured ZnS can be formed after facile reflux sulfidation process. The formation process can be described as follows: in the initial sulfidation process, an amorphous but firm shell, consisting of Zn and S, forms on the surface of ZIF-8. Then the inner core shrinks, and the central mass relocates to thicken the outer shell [47,48]. During quenching, the adhesive force from outer shell is released and the fresh surface of inner core ZIF-8 is exposed [49,50]. The yolk-shell particles with an inner core of ZIF-8 and an outer shell of amorphous ZnS are formed, similarly to the previously reported heterogeneous contraction process. After performing another sulfidation, another shell can be formed on the fresh surface of ZIF-8. Hence, multi-shell ZnS particles could be obtained after three quenching and sulfidation processes (Figs. S2 and S3). The as-prepared ZnS particles remain highly uniform after several sulfidation reactions with slight cavities on the surface of truncated octahedron particles (Fig. S2). The multi-shell structure of ZnS is revealed by TEM in Fig. S3. Afterward, the multi-shell structured Sb₂S₃ microparticles can be achieved via a simple ion-exchange method (see details in Experimental Procedures). This successful ion-exchange might rely on the relatively smaller solubility product constant of antimony sulfide than that of zinc sulfide [48]. To further explore this synthesis approach, the reaction conditions were modified to achieve various hollow structures. As shown in the schematic Fig. S4, increasing amount of reactant, prolonging reaction time and performing only one sulfidation reaction leads to one outer shell only during the whole sulfidation process. Afterward, the inner core of ZIF-8 is shrunken during the whole reaction while the central mass is continuously relocated outward driven by the reaction between Zn²⁺ cations that are slowly dissolved from ZIF-8 template and S²⁻ anions that are liberated during hydrolysis of thioacetamide [47]. This process results in the single-shell ZnS and the consequent single-shell Sb₂S₃ (Figs. S5 and S6). For a moderate amount of thioacetamide, moderate reaction time and two sulfidation reactions, core-shell structures are formed (Fig. S7). The outer ZnS shell is formed at the initial stage of the reaction. After quenching, a fresh surface of ZIF-8 is exposed. When the as-obtained sample is placed in the solution containing thioacetamide and the fresh surface of ZIF-8 is exposed to S²⁻ anions, an inner core of ZnS is formed. This results in the core-shell ZnS particles and leads to the consequent core-shell Sb₂S₃ particles (Figs. S8 and S9). When being

with three sulfidation reactions, two ZnS shells were formed, resulting in the multi-shell ZnS particles and the consequent multi-shell Sb₂S₃ particles (Figs. 1 and 2). These results suggest the proposed strategy can be applied for the rational design and synthesis of hollow structured materials with complex internal features.

The detailed morphological and structural characterization of multi-shell Sb₂S₃ particles is shown in Figs. 2 and 3. As can be seen from these figures the as-prepared multi-shell Sb₂S₃ particles are highly uniform (see Fig. 2A). The multiple shells of Sb₂S₃ are identified in Fig. 2B. The size of each particle is around 2 μm while the thickness of each shell is around tens of nanometers. The multi-shell structure is further confirmed by STEM images in Fig. 2C and Fig. S10. Additionally, it can be found out that the inner shell of Sb₂S₃ maintains the shape of truncated octahedron. In the HRTEM image (Fig. 2D), the lattice spacing is 0.35 nm, which agrees with the (1$\overline{1}\overline{1}$) plane of Sb₂S₃. Moreover, the elemental mapping and elemental line scan (Fig. 2E and F) provides more evidence to support the triple-shell structure. Especially, two peaks located between 1500 and 2000 nm on the line scan spectra indicate the multi-shell structure of Sb₂S₃. Furthermore, the triple-shell structure is also demonstrated by the scanning electron microscopy image of one particle with a broken shell (Fig. S11), which consists of two outer shells and a truncated octahedron core. Additionally, the X-ray powder diffraction pattern of the Sb₂S₃ sample after calcination demonstrates the pure phase of stibnite antimony sulfide (JCPDS #42–1393) (Fig. 3A). The X-ray photoelectron spectroscopy (XPS) survey spectra and the high-resolution Sb and S spectra (Fig. 3B–D) also prove the successful synthesis of Sb₂S₃ without impurities.

The as-prepared samples were employed as anodes for sodium ion batteries to evaluate the electrochemical performance of antimony sulfide with unique multi-shell structure. Pristine Sb₂S₃ with a morphology of solid wires was prepared as a control sample (Figs. S12 and S13). As shown in Fig. 4A, during the initial cycle, the multi-shell sample achieved an initial reversible capacity of 901 mAh g⁻¹ with an initial Coulombic efficiency of 55% while the initial Coulombic efficiencies of the single-shell and pristine samples are 61.7 and 45.7%, respectively. This low initial Coulombic efficiency can be attributed to the irreversible reaction of Na⁺ with Sb₂S₃, the decomposition of electrolyte and the formation of solid electrolyte interface (SEI), which agrees with the initial cyclic voltammetry profiles showing a large void between the initial cycle curve and the second cycle curve (Fig. 4B) [51]. As shown in Fig. 4C, the cycling performance of the as-prepared samples was evaluated under the current density of 1000 mA g⁻¹. The pristine Sb₂S₃ exhibited an initial reversible capacity of only around 210 mAh g⁻¹. For comparison, both the multi-shell sample and the single-shell sample exhibited initial reversible capacities of over 700 mAh g⁻¹ under the same current density, demonstrating that the hollow structure with thin functional shell and large surface area offers an enhanced electrochemical activity. On the other hand, although the
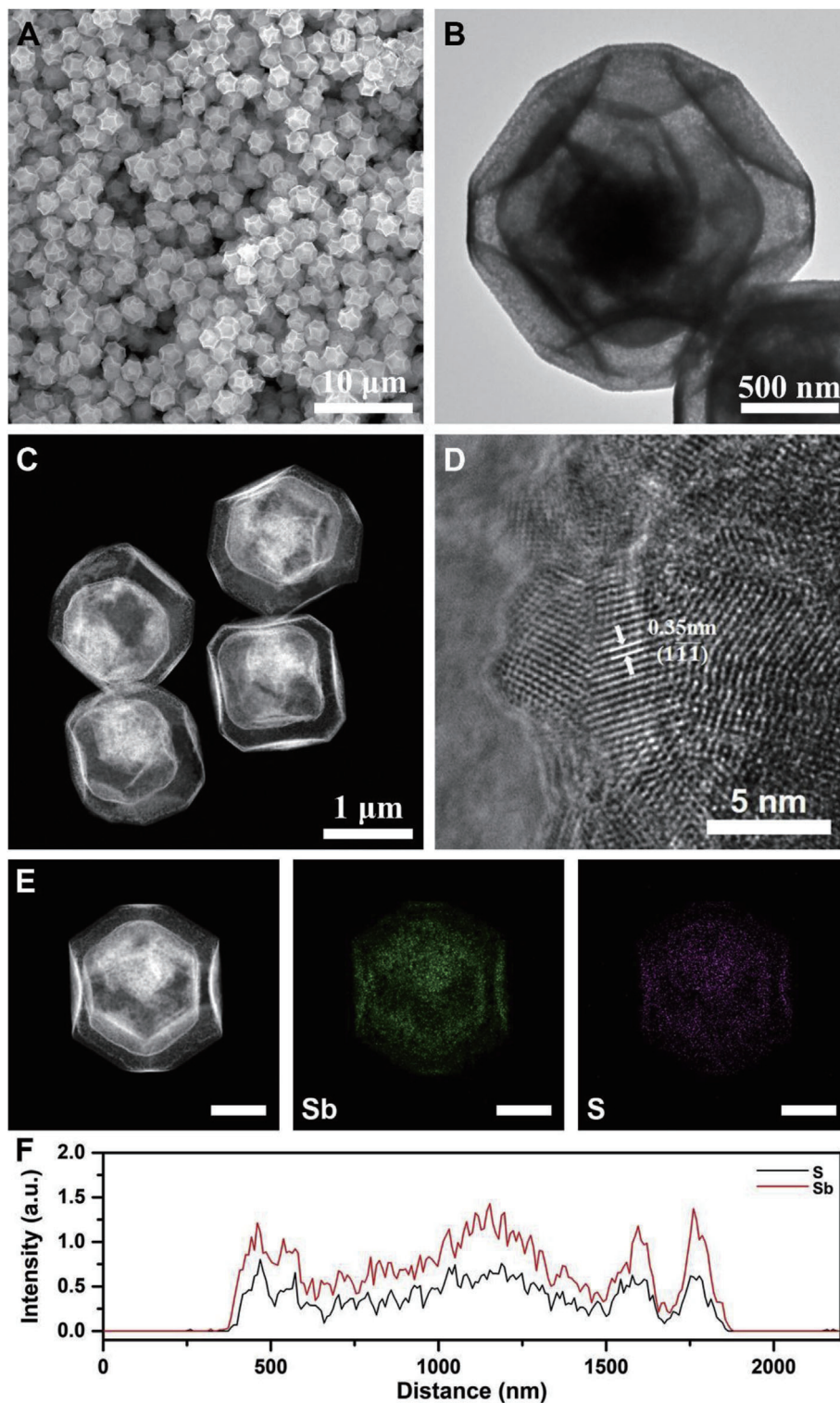
Fig. 2. A) SEM image, B) TEM image, C) STEM image, D) HRTEM image E) STEM elemental mapping images (The scale bar is 500 nm), and F) STEM elemental line scanning spectrum of multi-shell Sb_2S_3.

single-shell Sb_2S_3 presents high initial reversible capacity, the capacity decreases gradually due to the unstable nature of single-shell structure. The poor durability of single-shell Sb_2S_3 is also demonstrated by the discharge/charge profiles from different cycles (Fig. S14), in which the single-shell Sb_2S_3 shows the most significant capacity fading. After 50 cycles, the multi-shell Sb_2S_3 could still maintain a reversible capacity of over 500 mAh g^{-1}, much higher than that of pristine (around 150 mAh g^{-1}) and single-shell Sb_2S_3 (around 200 mAh g^{-1}), demonstrating the

advantages of enhanced durability and higher energy density. In the rate performance test (Fig. 4D, Fig. S15), the pristine sample exhibited the reversible capacities of 308, 299, 273, 198 and 116 mAh g^{-1} at the current densities of 100, 200, 400, 1000 and 2000 mA g^{-1}, respectively. As compared with the pristine sample, the multi-shell Sb_2S_3 exhibited the higher reversible capacities of 909, 871, 806, 725 and 604 mAh g^{-1} at the current densities of 100, 200, 400, 1000 and 2000 mA g^{-1}, respectively. This rate performance is relatively
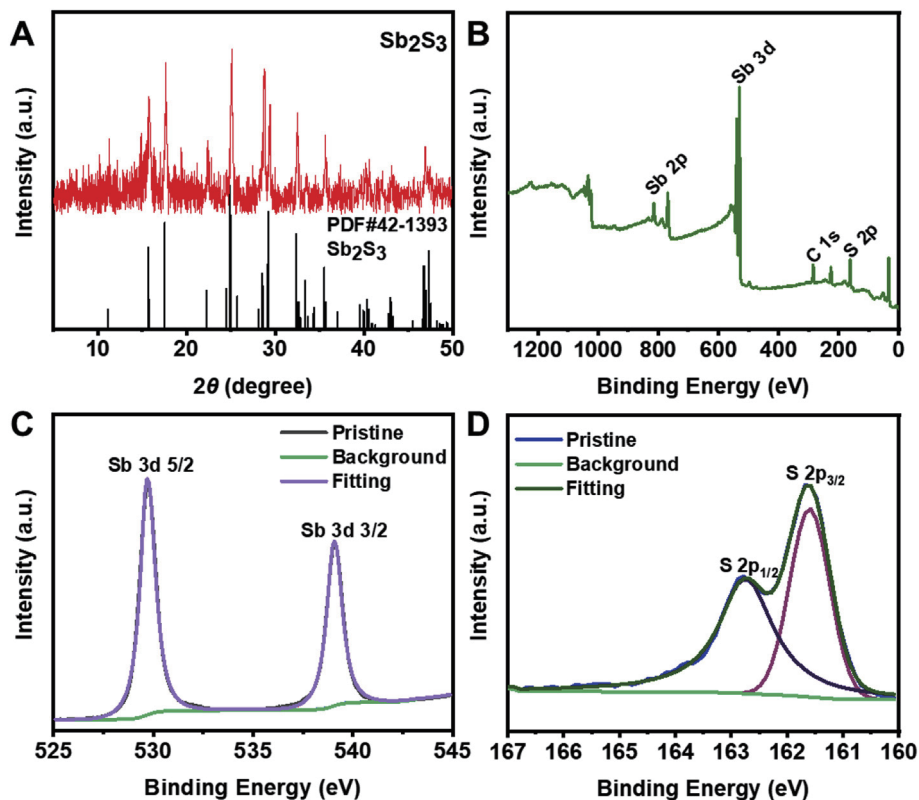
Fig. 3. A) X-ray powder diffraction spectra; B) XPS survey spectrum; C, D) High resolution XPS spectra of Sb and S of multi-shell Sb$_2$S$_3$.

remarkable compared with the state-of-art anode materials for sodium ion batteries (Table S1). The reversible rate capability of multi-shell structured Sb$_2$S$_3$ is significantly higher than that of the pristine sample (116 mAh g^{-1} at 2000 mA g^{-1}), demonstrating an enhanced electrochemical activity and higher gravimetric energy density. Additionally, in the initial cycles, the single-shell Sb$_2$S$_3$ exhibited a similar reversible capacity with multi-shell Sb$_2$S$_3$, also demonstrating the enhanced electrochemical activity of hollow structure. Nonetheless, with the process of cycling, the reversible capacity of single-shell one decreased gradually, exhibiting the poor durability of the single-shell Sb$_2$S$_3$ as an anode for sodium ion batteries. This study shows that the multi-shell structure can offer better durability than the single-shell counterpart, demonstrating the superiority of multi-shell structured Sb$_2$S$_3$.

Operando synchrotron X-ray powder diffraction (XRPD) measurements under high intensity X-ray for both the multi-shell and pristine samples were conducted at PD beamline, Australian Synchrotron (ANSTO) to demonstrate the origin of higher reversible capacities of multi-shell samples [52,53]. The electrochemical reactions of Sb$_2$S$_3$ with sodium-ion can be represented by the following equations [26,51,54]:

Conversion reaction:

$$Sb_2S_3 + 6Na^+ + 6e^- \Leftrightarrow 2Sb + 3Na_2S \tag{1}$$

Alloying/dealloying reaction:

$$2Sb + 6Na^+ + 6e^- \Leftrightarrow 2Na_3Sb \tag{2}$$

In order to make a comparison between the patterns of the multi-shell structured Sb$_2$S$_3$ and the pristine one, all the diffraction intensities were normalized with the intensity of initial (221) diffraction peak of Sb$_2$S$_3$. In the XRPD plots of Sb$_2$S$_3$ (Fig. 5A and B), the peaks located at around 13.5°, 14.0° and 14.3° can be assigned to (221), (301) and (311) of Sb$_2$S$_3$, respectively. During the discharge process of the multi-shell sample (Fig. 5A), these peaks disappear gradually until the voltage of 0.75 V. On the contrary, the diffraction peaks of the pristine Sb$_2$S$_3$

remain to the voltage of 0.5 V. This phenomenon demonstrates that antimony sulfide in the multi-shell sample reacts efficiently with sodium ions while some in the pristine one remains, indicating more complete conversion reaction in the multi-shell sample. This result is consistent with the initial discharge curves showing a small plateau around 0.75 V for the multi-shell sample while the corresponding plateau is missing for the pristine sample. This can be attributed to the better contact of multi-shell Sb$_2$S$_3$ with the electrolyte than with the pristine sample, resulting in the enhanced electrochemical activity and higher reversible capacity. Larger surface area of multi-shell samples supports this conclusion (Fig. S16). From Fig. 5C and D, the reflection of Sb (012) facet located at ~12.3° appears with the diminution of Sb$_2$S$_3$ peaks, indicating the occurrence of the conversion reaction between sodium ion and antimony sulfide. It should be noticed that the intensity of Sb reflection in the multi-shell is higher than that in the pristine sample. This indicates that more antimony is generated in the multi-shell sample during conversion reactions, revealing that this reaction is more complete. Consequently, the intensity of Na$_3$Sb reflection at ~17.5° of the pristine sample is significantly lower than that for the multi-shell sample due to smaller amount of the generated antimony (Fig. 5E and F). In conclusion, the key difference between these two samples is in the conversion reactions. Due to smaller amount of generated Sb in the conversion reaction between the pristine sample and sodium, a large amount of Sb$_2$S$_3$ remains unreacted. The lack of antimony limits the sodium ion storage capability, leading to the lower reversible capacity of the pristine sample. As regards the multi-shell sample, more antimony is generated due to the high conversion efficiency, which enhances alloying reaction. As can be seen from the scheme, higher reversible capacity of the multi-shell sample in comparison to the pristine Sb$_2$S$_3$ solid rods can be ascribed to more complete reaction with sodium ions.

Apart from the superior performance under low current density, the multi-shell structured sample exhibited excellent performance under high current density. Therefore, the sodium-storage mechanism under
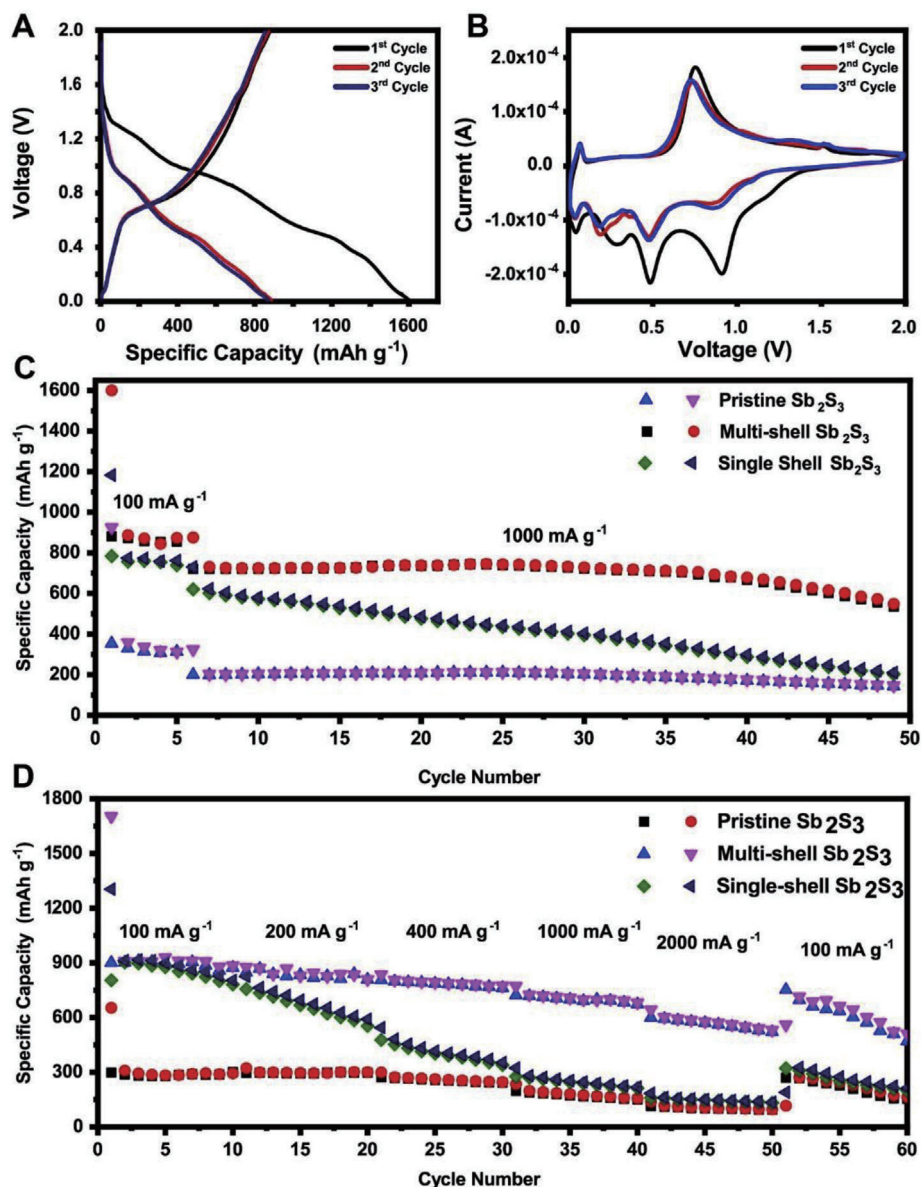
Fig. 4. A) Initial discharging/charging profiles of multi-shell Sb_2S_3; B) Initial CV curves of multi-shell Sb_2S_3; C) Comparison of long cycling performance of multi-shell Sb_2S_3, single-shell Sb_2S_3 and pristine Sb_2S_3; D) Comparison of the rate performance of multi-shell Sb_2S_3, single-shell Sb_2S_3 and pristine Sb_2S_3.

high current density is also investigated by CV technique. The degree of capacitive effect can be qualitatively analyzed by separating the current response into the contributions associated with diffusion-controlled process and pseudocapacitive charge storage. Among these two storage processes, the capacitive charge storage is considered to be advantageous because of high charging rate and consequently, high power density [24,25]. Fig. 6A and Fig. 6B show the CV curves at various sweep rates from 0.1 to 10 mV s^{-1} of multi-shell Sb_2S_3 and pristine Sb_2S_3, respectively. As shown in Fig. 6C, the pseudocapacitive contributions of multi-shell Sb_2S_3 are 44.2, 46.0, 48.2, 53.2, 65.8 and 84.0% under the sweep rate of 0.2, 0.5, 1, 2, 5 and 10 mV s^{-1}, respectively. Additionally, the pristine sample exhibits the contribution of 31.2, 33.8, 37.3, 42.8, 55.9 and 74.6% under the same sweep rate, correspondingly (Fig. 6D). According to the previous report, the as-achieved multi-shell structure assembled by nanoparticles enables a better Na$^+$ or electrolyte access to the surface of active material. Additionally, the multi-shell structure also offers both the exterior and interior surfaces for the electrochemical reaction. Consequently, this multi-shell structure can achieve a higher pseudocapacitive

contribution [25]. Therefore, the high pseudocapacitive contribution of the multi-shell sample can be considered as the origin of its high capacity under high current densities.

There are several implications of the multi-shell Sb_2S_3 anodes in sodium ion batteries. Specifically, as compared with pristine Sb_2S_3, the diameter of multi-shell Sb_2S_3 is larger than that of pristine one. However, due to the significantly smaller thickness, the multi-shell structure offers the better contact with electrolyte, which offers more electrochemical active sites for the electrochemical reactions with Na ions. Additionally, taking account of the large volume expansion during the electrochemical reaction between Sb_2S_3 and sodium ions, the multi-shell structure offers extra room to accommodate large volume expansion and alleviate strain. These two reasons lead to the enhanced electrochemical activity and, consequently, a more complete reaction with sodium ions. As can be seen from the *operando* synchrotron-based XRPD patterns, the key difference is more complete conversion reaction and more intermediate antimony to alloy with sodium ions, resulting in higher reversible capacity of the multi-shell sample. Therefore, the latter offers much higher reversible capacity and consequently, higher
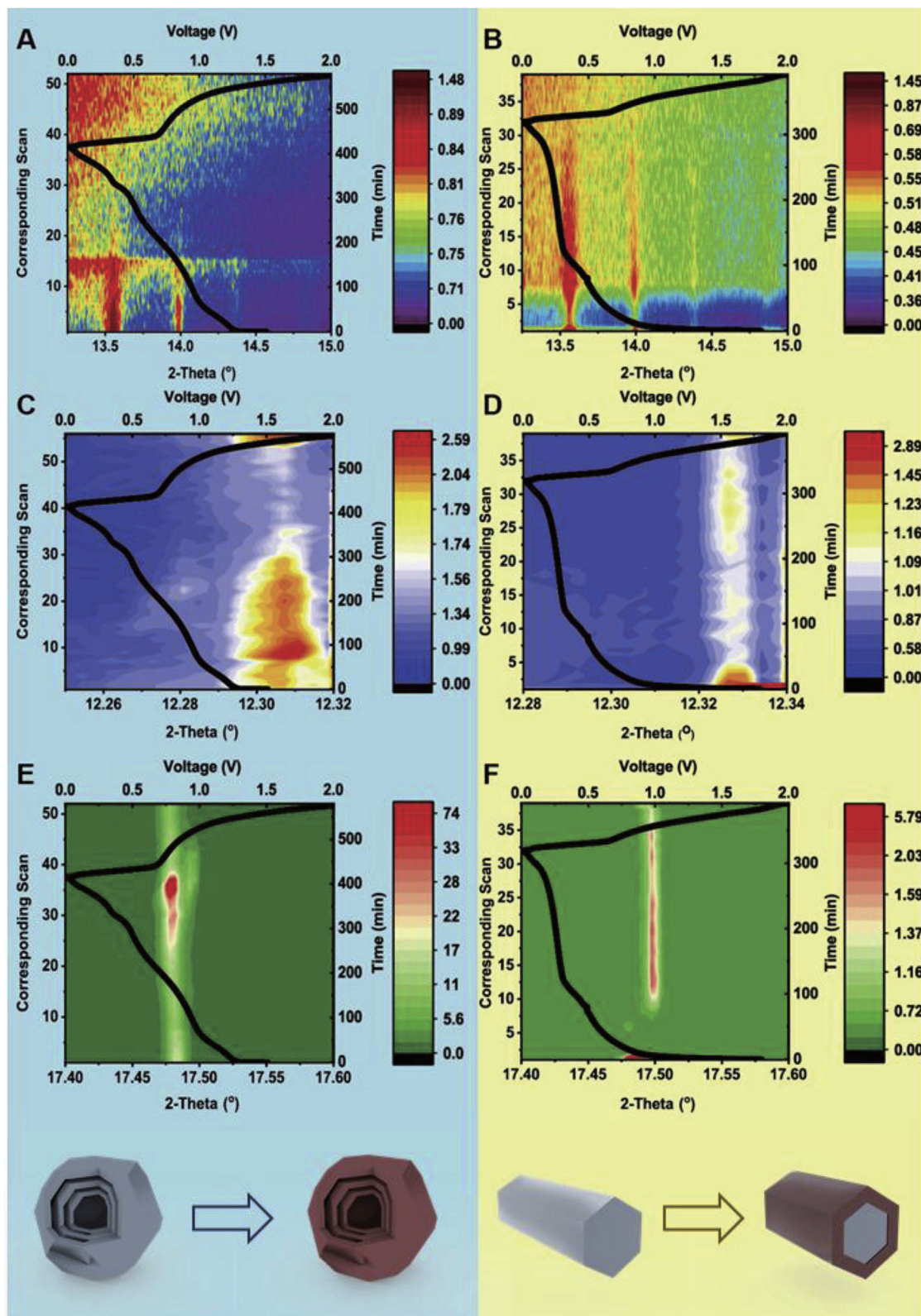
Fig. 5. Comparison of contour plots of the *operando* synchrotron X-ray powder diffraction with superimposed voltage profiles shown for selected ranges of different samples
A, B) Sb_2S_3 C, D) Sb E, F) Na_3Sb.

gravimetric energy density. On the other hand, as compared with the single-shell sample, the multi-shell Sb_2S_3 with large internal voids offers higher volumetric energy density, which is a crucial concern for anodes in sodium ion batteries. Furthermore, as compared with the

single-shell counterparts, the multi-shell sample also offers an enhanced durability, which can be attributed to the extra support from different shells and the exterior shell protecting the interior shells [37,38,42]. To sum up, the multi-shell Sb_2S_3 can maintain the high gravimetric energy
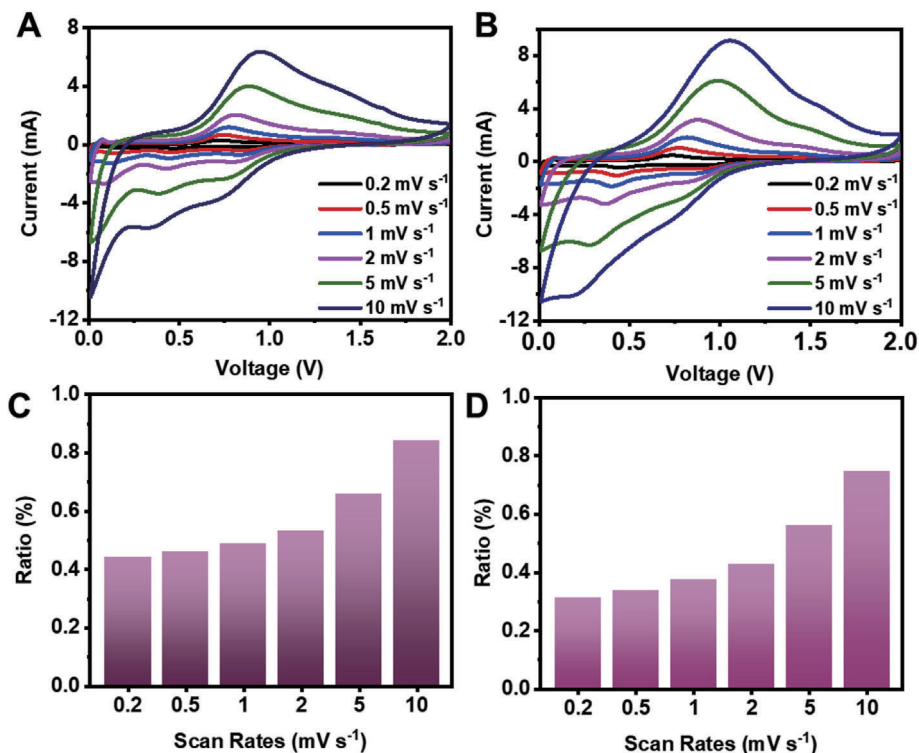
Fig. 6. CV curves of (A) multi-shell Sb_2S_3, and (B) pristine Sb_2S_3 at various sweep rates. Diagram of capacitive contribution to the total capacity of (C) multi-shell Sb_2S_3, and (D) pristine Sb_2S_3.

density of hollow structure with maintained volumetric energy density and better durability than the single-shell one.

4. Conclusion

In summary, we report the synthesis of Sb_2S_3 hollow structures with complex interior multi-shells. As compared with the single-shell Sb_2S_3, the multi-shell one exhibited an enhanced durability and higher volumetric energy density. On the other hand, the multi-shell one exhibited much higher reversible capacity because of the enhanced electrochemical activity originating from the hollow structure. The *operando* synchrotron-based X-ray diffraction reveals that the key difference is more complete conversion reaction. The design of multi-shell Sb_2S_3 as the anode for sodium ion batteries opens new opportunities for the development of electrodes with high energy density and enhanced durability for similar electrochemical energy storage systems.

Conflicts of interest

The authors declare no competing financial interests.

Acknowledgments

Appendix A. Supplementary data

Supplementary data to this article can be found online at https://doi.org/10.1016/j.nanoen.2019.04.008.

References

[1] D. Larcher, J.M. Tarascon, Towards greener and more sustainable batteries for electrical energy storage, Nat. Chem. 7 (2015) 19–29.
[2] N. Yabuuchi, K. Kubota, M. Dahbi, S. Komaba, Research development on sodium-ion batteries, Chem. Rev. 114 (2014) 11636–11682.
[3] Z. Yang, J. Zhang, M.C.W. Kintner-Meyer, X. Lu, D. Choi, J.P. Lemmon, J. Liu, Electrochemical energy storage for green grid, Chem. Rev. 111 (2011) 3577–3613.
[4] J.Y. Hwang, S.T. Myung, Y.K. Sun, Sodium-ion batteries: present and future, Chem. Soc. Rev. 46 (2017) 3529–3614.
[5] V.L. Chevrier, G. Ceder, Challenges for Na-ion negative electrodes, J. Electrochem. Soc. 158 (2011) A1011–A1014.
[6] S.P. Ong, V.L. Chevrier, G. Hautier, A. Jain, C. Moore, S. Kim, X. Ma, G. Ceder, Voltage, stability and diffusion barrier differences between sodium-ion and lithium-ion intercalation materials, Energy Environ. Sci. 4 (2011) 3680–3688.
[7] V. Palomares, M. Casas-Cabanas, E. Castillo-Martinez, M.H. Han, T. Rojo, Update on Na-based battery materials. a growing research path, Energy Environ. Sci. 6 (2013) 2312–2337.
[8] V. Palomares, P. Serras, I. Villaluenga, K.B. Hueso, J. Carretero-Gonzalez, T. Rojo, Na-ion batteries, recent advances and present challenges to become low cost energy storage systems, Energy Environ. Sci. 5 (2012) 5884–5901.
[9] S.W. Kim, D.H. Seo, X. Ma, G. Ceder, K. Kang, Electrode materials for rechargeable sodium-ion batteries: potential alternatives to current lithium-ion batteries, Adv. Energy Mater. 2 (2012) 710–721.
[10] P.K. Nayak, L. Yang, W. Brehm, P. Adelhelm, From lithium-ion to sodium-ion batteries: advantages, challenges, and surprises, Angew. Chem. Int. Ed. 57 (2018) 102–120.
[11] M. Li, J. Lu, Z. Chen, K. Amine, 30 years of lithium-ion batteries, Adv. Mater. 30 (2018) 1800561.
[12] W. Xue, L. Miao, L. Qie, C. Wang, S. Li, J. Wang, J. Li, Gravimetric and volumetric energy densities of lithium-sulfur batteries, Curr. Opin. Electrochem. 6 (2017) 92–99.
[13] Y. Sun, N. Liu, Y. Cui, Promises and challenges of nanomaterials for lithium-based rechargeable batteries, Nat. Energy 1 (2016) 16071.
[14] X. Li, P. Yan, M.H. Engelhard, A.J. Crawford, V.V. Viswanathan, C. Wang, J. Liu, V.L. Sprenkle, The importance of solid electrolyte interphase formation for long cycle stability full-cell Na-ion batteries, Nanomater. Energy 27 (2016) 664–672.
[15] W. Hou, X. Guo, X. Shen, K. Amine, H. Yu, J. Lu, Solid electrolytes and interfaces in all-solid-state sodium batteries: progress and perspective, Nanomater. Energy 52 (2018) 279–291.
[16] J. Sun, H.W. Lee, M. Pasta, H.T. Yuan, G.Y. Zheng, Y.M. Sun, Y.Z. Li, Y. Cui, A phosphorene-graphene hybrid material as a high-capacity anode for sodium-ion batteries, Nat. Nanotechnol. 10 (2015) 980–985.
[17] Z. Lin, T. Liu, X. Ai, C. Liang, Aligning academia and industry for unified battery performance metrics, Nat. Commun. 9 (2018) 5262.

[18] W. Luo, F. Shen, C. Bommier, H. Zhu, X. Ji, L. Hu, Na-ion battery anodes: materials and electrochemistry, Acc. Chem. Res. 49 (2016) 231–240.

[19] H. Zhang, I. Hasa, S. Passerini, Beyond insertion for Na-ion batteries: nanostructured alloying and conversion anode materials, Adv. Energy Mater. 8 (2018) 1702582.

[20] M.R. Palacin, Recent advances in rechargeable battery materials: a chemist's perspective, Chem. Soc. Rev. 38 (2009) 2565–2575.

[21] F. Xie, L. Zhang, D. Su, M. Jaroniec, S.Z. Qiao, $Na_2Ti_3O_7$@N-doped carbon hollow spheres for sodium-ion batteries with excellent rate performance, Adv. Mater. 29 (2017) 1700989.

[22] F. Xie, L. Zhang, C. Ye, M. Jaroniec, S.Z. Qiao, The application of hollow structured anodes for sodium-ion batteries: from simple to complex systems, Adv. Mater. 30 (2018) 1800492.

[23] C. Wu, S.X. Dou, Y. Yu, The state and challenges of anode materials based on conversion reactions for sodium storage, Small 14 (2018) 1703671.

[24] D. Chao, B. Ouyang, P. Liang, T.T.T. Huong, G. Jia, H. Huang, X. Xia, R.S. Rawat, H.J. Fan, C-plasma of hierarchical graphene survives SnS bundles for ultrastable and high volumetric Na-ion storage, Adv. Mater. 30 (2018) 1804833.

[25] D. Chao, C. Zhu, P. Yang, X. Xia, J. Liu, J. Wang, X. Fan, S.V. Savilov, J. Lin, H.J. Fan, Z.X. Shen, Array of nanosheets render ultrafast and high-capacity Na-ion storage by tunable pseudocapacitance, Nat. Commun. 7 (2016) 12122.

[26] D.Y.W. Yu, P.V. Prikhodchenko, C.W. Mason, S.K. Batabyal, J. Gun, S. Sladkevich, A.G. Medvedev, O. Lev, High-capacity antimony sulphide nanoparticle-decorated graphene composite as anode for sodium-ion batteries, Nat. Commun. 4 (2013) 2922.

[27] H. Hou, M. Jing, Z. Huang, Y. Yang, Y. Zhang, J. Chen, Z. Wu, X. Ji, One-dimensional rod-like Sb_2S_3-based anode for high-performance sodium-ion batteries, ACS Appl. Mater. Interfaces 7 (2015) 19362–19369.

[28] Y. Zhao, A. Manthiram, Amorphous Sb_2S_3 embedded in graphite: a high-rate, long-life anode material for sodium-ion batteries, Chem. Commun. 51 (2015) 13205–13208.

[29] Y. Zhu, P. Nie, L. Shen, S. Dong, Q. Sheng, H. Li, H. Luo, X. Zhang, High rate capability and superior cycle stability of a flower-like Sb_2S_3 anode for high-capacity sodium ion batteries, Nanoscale 7 (2015) 3309–3315.

[30] S. Yao, J. Cui, Z. Lu, Z.-L. Xu, L. Qin, J. Huang, Z. Sadighi, F. Ciucci, J.K. Kim, Unveiling the unique phase transformation behavior and sodiation kinetics of 1d van der waals Sb_2S_3 anodes for sodium ion batteries, Adv. Energy Mater. 7 (2017) 1602149.

[31] F. Strauss, G. Rousse, D. Alves Dalla Corte, M. Ben Hassine, M. Saubanère, M. Tang, H. Vezin, M. Courty, R. Dominko, J.M. Tarascon, Electrochemical activity and high ionic conductivity of lithium copper pyroborate $Li_6CuB_4O_{10}$, Phys. Chem. Chem. Phys. 18 (2016) 14960–14969.

[32] S. Chae, M. Ko, K. Kim, K. Ahn, J. Cho, Confronting issues of the practical implementation of Si anode in high-energy lithium-ion batteries, Joule 1 (2017) 47–60.

[33] D. Andre, H. Hain, P. Lamp, F. Maglia, B. Stiaszny, Future high-energy density anode materials from an automotive application perspective, J. Mater. Chem. 5 (2017) 17174–17198.

[34] P.G. Bruce, B. Scrosati, J.M. Tarascon, Nanomaterials for rechargeable lithium batteries, Angew. Chem. Int. Ed. 47 (2008) 2930–2946.

[35] N. Liu, Z. Lu, J. Zhao, M.T. McDowell, H.W. Lee, W. Zhao, Y. Cui, A pomegranate-inspired nanoscale design for large-volume-change lithium battery anodes, Nat. Nanotechnol. 9 (2014) 187–192.

[36] L. Yu, H. Hu, H.B. Wu, X.W. Lou, Complex hollow nanostructures: synthesis and energy-related applications, Adv. Mater. 29 (2017) 1604563.

[37] J. Qi, X. Lai, J. Wang, H. Tang, H. Ren, Y. Yang, Q. Jin, L. Zhang, R. Yu, G. Ma, Z. Su, H. Zhao, D. Wang, Multi-shelled hollow micro-/nanostructures, Chem. Soc. Rev. 44 (2015) 6749–6773.

[38] J. Wang, H. Tang, H. Wang, R. Yu, D. Wang, Multi-shelled hollow micro-/nanostructures: promising platforms for lithium-ion batteries, Mater. Chem. Front. 1 (2017) 414–430.

[39] P. He, Y. Fang, X.Y. Yu, X.W. Lou, Hierarchical nanotubes constructed by carbon-coated ultrathin SnS nanosheets for fast capacitive sodium storage, Angew. Chem. Int. Ed. 56 (2017) 12202–12205.

[40] D. Zhang, W. Sun, Y. Zhang, Y. Dou, Y. Jiang, S.X. Dou, Engineering hierarchical hollow nickel sulfide spheres for high-performance sodium storage, Adv. Funct. Mater. 26 (2016) 7479–7485.

[41] K. Tang, L. Fu, R.J. White, L. Yu, M.M. Titirici, M. Antonietti, J. Maier, Hollow carbon nanospheres with superior rate capability for sodium-based batteries, Adv. Energy Mater. 2 (2012) 873–877.

[42] J. Wang, H. Tang, L. Zhang, H. Ren, R. Yu, Q. Jin, J. Qi, D. Mao, M. Yang, Y. Wang, P. Liu, Y. Zhang, Y. Wen, L. Gu, G. Ma, Z. Su, Z. Tang, H. Zhao, D. Wang, Multi-shelled metal oxides prepared via an anion-adsorption mechanism for lithium-ion batteries, Nat. Energy 1 (2016) 16050.

[43] L. Zhou, Z. Zhuang, H. Zhao, M. Lin, D. Zhao, L. Mai, Intricate hollow structures: controlled synthesis and applications in energy storage and conversion, Adv. Mater. 29 (2017) 1602914.

[44] N.L. Torad, M. Hu, Y. Kamachi, K. Takai, M. Imura, M. Naito, Y. Yamauchi, Facile synthesis of nanoporous carbons with controlled particle sizes by direct carbonization of monodispersed ZIF-8 crystals, Chem. Commun. 49 (2013) 2521–2523.

[45] H.B. Wu, S. Wei, L. Zhang, R. Xu, H.H. Hng, X.W. Lou, Embedding sulfur in MOF-derived microporous carbon polyhedrons for lithium-sulfur batteries, Chem. Eur J. 19 (2013) 10804–10808.

[46] Y. Pan, D. Heryadi, F. Zhou, L. Zhao, G. Lestari, H. Su, Z. Lai, Tuning the crystal morphology and size of zeolitic imidazolate framework-8 in aqueous solution by surfactants, CrystEngComm 13 (2011) 6937.

[47] Z. Jiang, H. Sun, Z. Qin, X. Jiao, D. Chen, Synthesis of novel ZnS nanocages utilizing ZIF-8 polyhedral template, Chem. Commun. 48 (2012) 3620–3622.

[48] P. Zhang, B.Y. Guan, L. Yu, X.W. Lou, Facile synthesis of multi-shelled ZnS-CdS cages with enhanced photoelectrochemical performance for solar energy conversion, Chemistry 4 (2018) 162–173.

[49] J. Guan, F. Mou, Z. Sun, W. Shi, Preparation of hollow spheres with controllable interior structures by heterogeneous contraction, Chem. Commun. 46 (2010) 6605–6607.

[50] L. Yu, X.Y. Yu, X.W. Lou, The design and synthesis of hollow micro-/nanostructures: present and future trends, Adv. Mater. 30 (2018) 1800939.

[51] S. Dong, C. Li, X. Ge, Z. Li, X. Miao, L. Yin, ZnS- Sb_2S_3@C core-double shell polyhedron structure derived from metal-organic framework as anodes for high performance sodium ion batteries, ACS Nano 11 (2017) 6474–6482.

[52] Q. Gu, J.A. Kimpton, H.E.A. Brand, Z. Wang, S. Chou, Solving key challenges in battery research using in situ synchrotron and neutron techniques, Adv. Energy Mater. 7 (2017) 1602831.

[53] S.M. Bak, Z. Shadike, R. Lin, X. Yu, X.Q. Yang, In situ/operando synchrotron-based x-ray techniques for lithium-ion battery research, NPG Asia Mater. 10 (2018) 563–580.

[54] X. Xiong, G. Wang, Y. Lin, Y. Wang, X. Ou, F. Zheng, C. Yang, J. Wang, M. Liu, Enhancing sodium ion battery performance by strongly binding nanostructured Sb_2S_3 on sulfur-doped graphene sheets, ACS Nano 10 (2016) 10953–10959.

74

Multi-Shell Hollow Structured Sb$_2$S$_3$ for Sodium-Ion Batteries with Enhanced Energy Density

Fangxi Xie, [a] Lei Zhang, [a] Qinfen Gu, [b] Dongliang Chao, [a] Mietek Jaroniec,[c] Shi-Zhang Qiao [a,d]*

[a] School of Chemical Engineering, The University of Adelaide, Adelaide, SA 5005, Australia

[b] Australian Synchrotron (ANSTO), 800 Blackburn Rd, Clayton, VIC 3168, Australia

[c] Department of Chemistry and Biochemistry, Kent State University, Kent, Ohio 44240, USA

[d] School of Materials Science and Engineering, Tianjin University, Tianjin, 300072, P. R. China

* Correspondence: s.qiao@adelaide.edu.au (S.-Z.Q.)

Supplementary Results
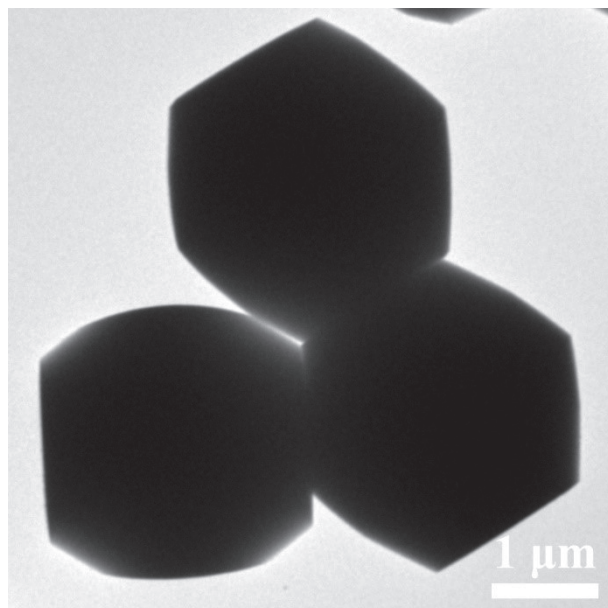
Fig. S1. TEM image of ZIF-8.
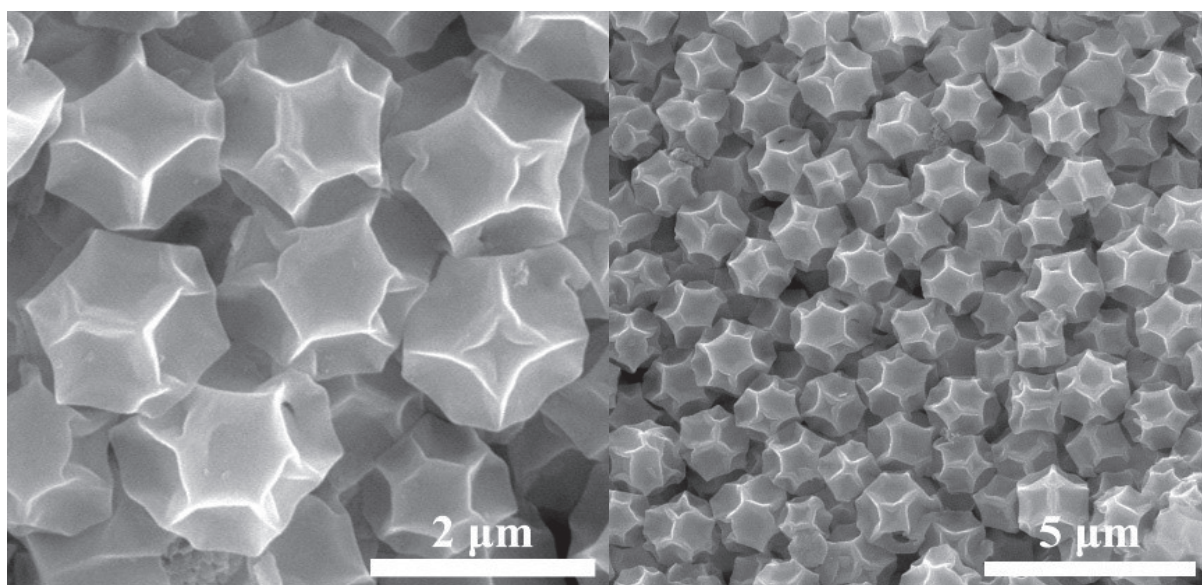
Fig. S2 SEM images of multi-shell ZnS.
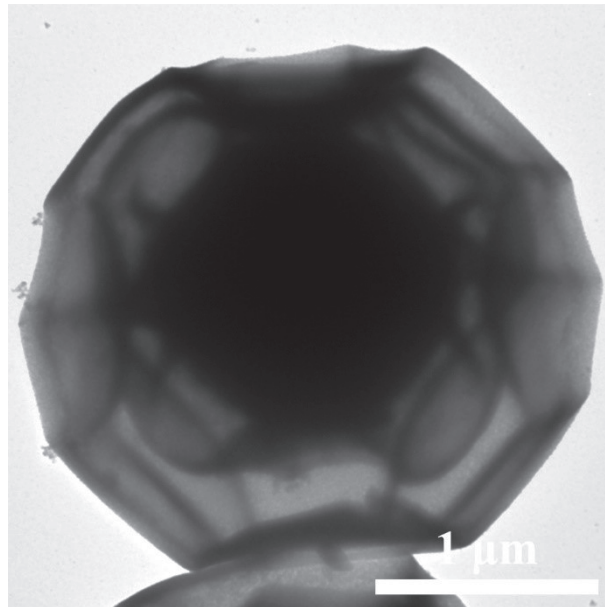
Fig. S3 TEM image of multi-shell ZnS.
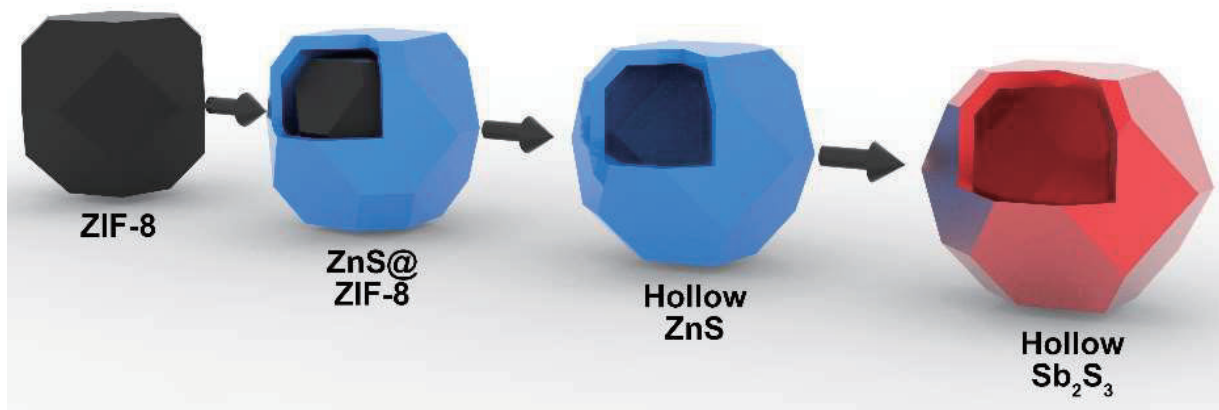
Fig. S4 Scheme illustrating the synthesis route from ZIF-8 to hollow Sb_2S_3.
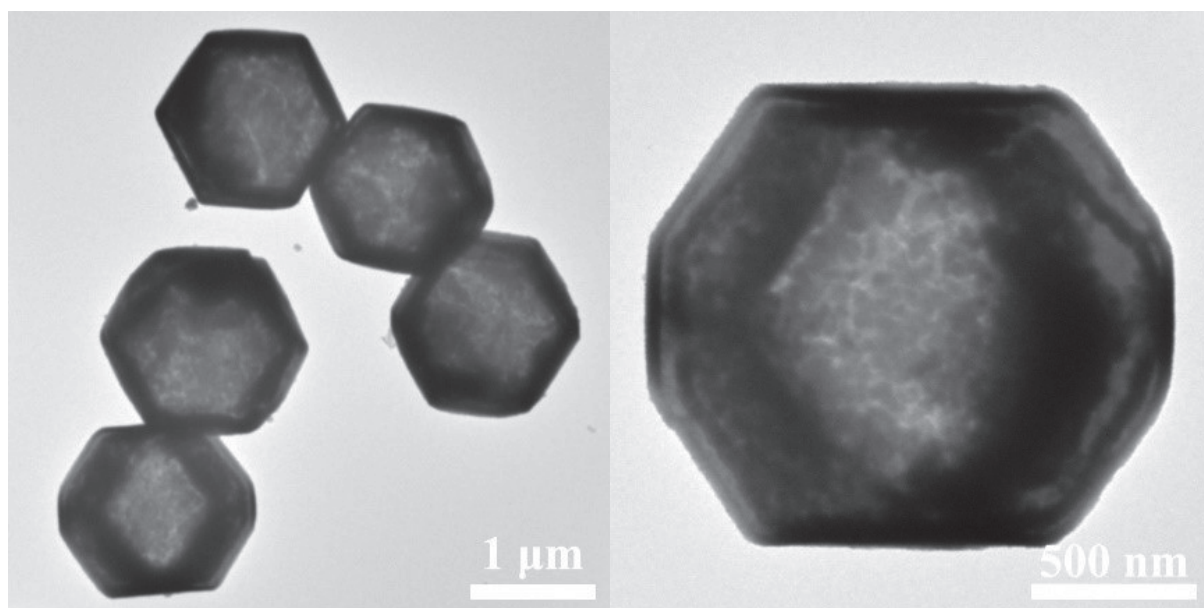
Fig. S5 TEM images of hollow ZnS.
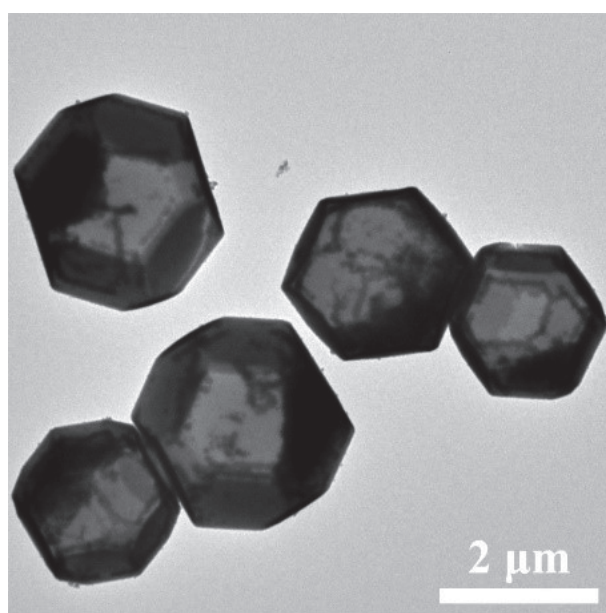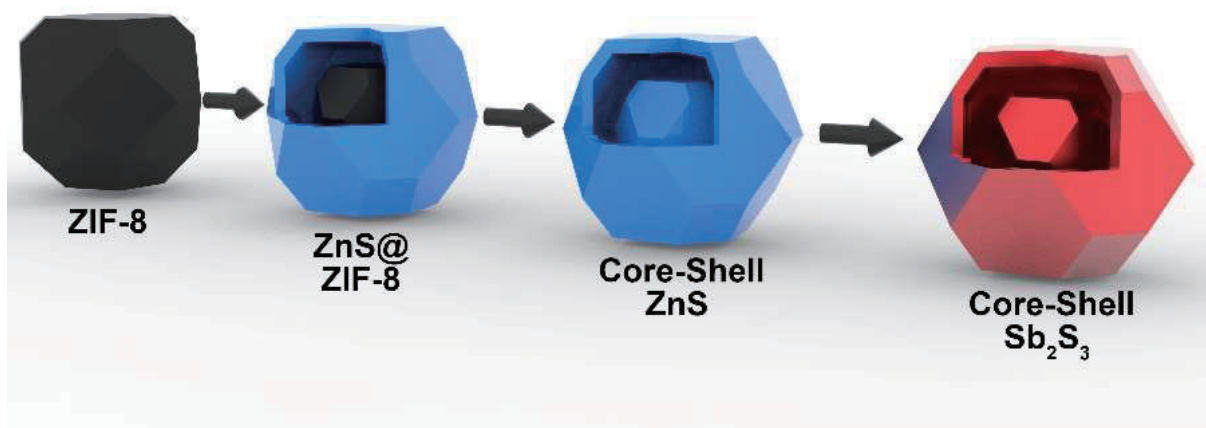

Fig. S6 TEM image of hollow Sb$_2$S$_3$.

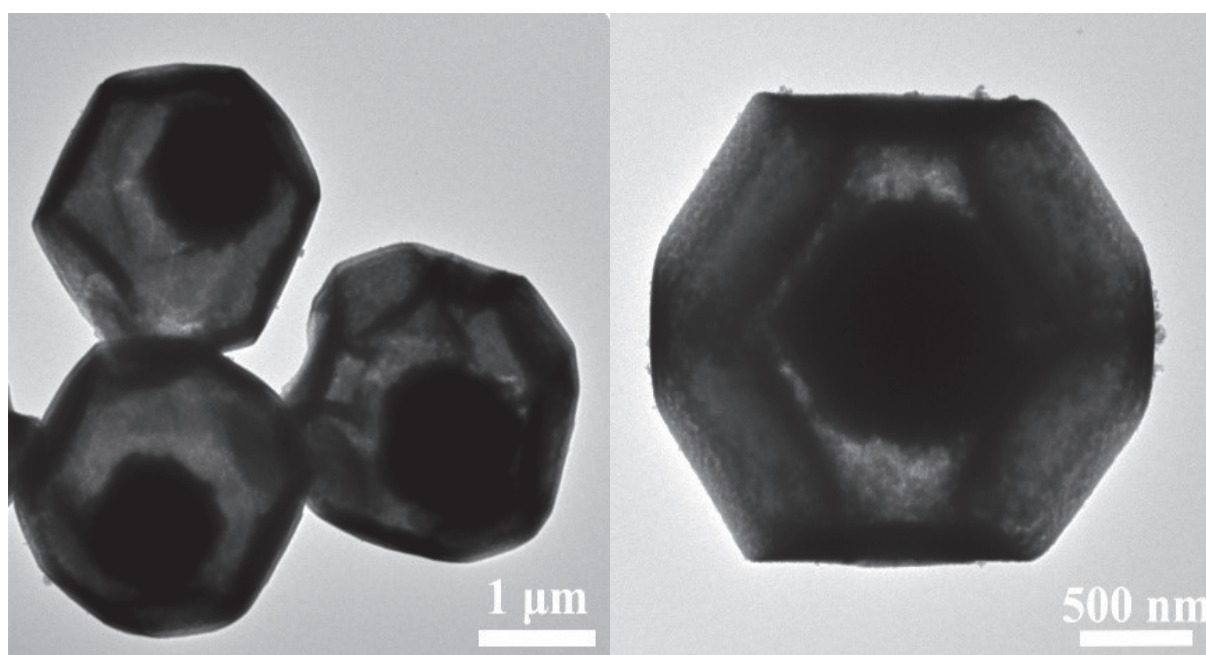**Fig. S7** Scheme illustrating the synthesis route from ZIF-8 to core-shell Sb₂S₃.
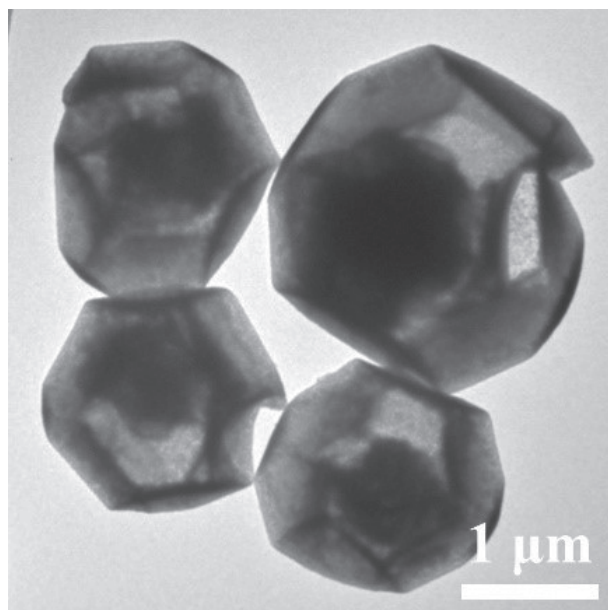

Fig. S8 TEM images of core-shell ZnS.

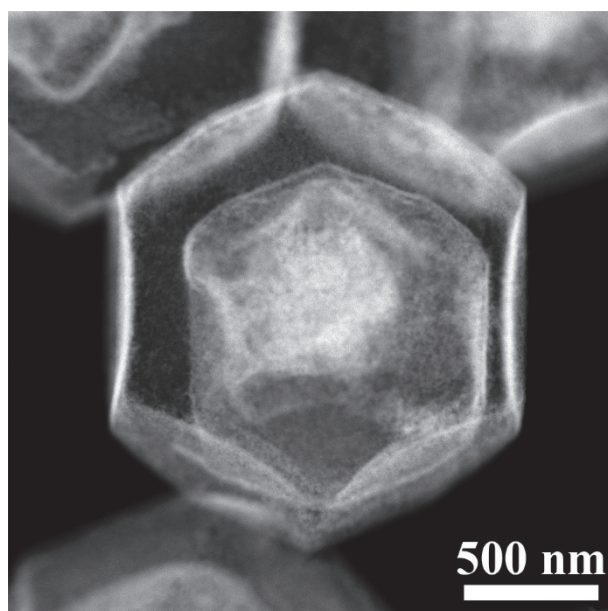**Fig. S9** TEM image of core-shell Sb_2S_3.

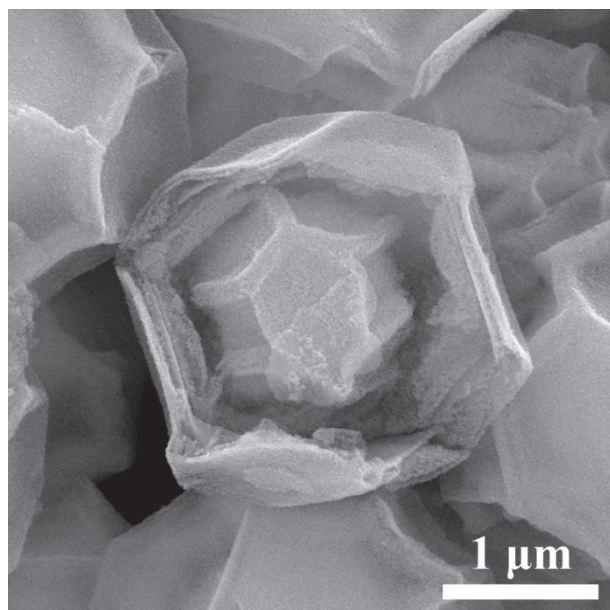**Fig. S10** STEM image of multi-shell Sb_2S_3 nanoparticle.

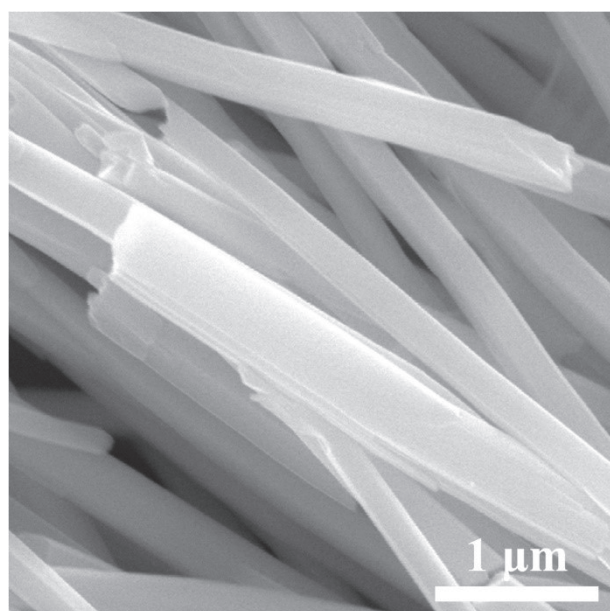**Fig. S11** SEM image of broken multi-shell Sb_2S_3 nanoparticle.

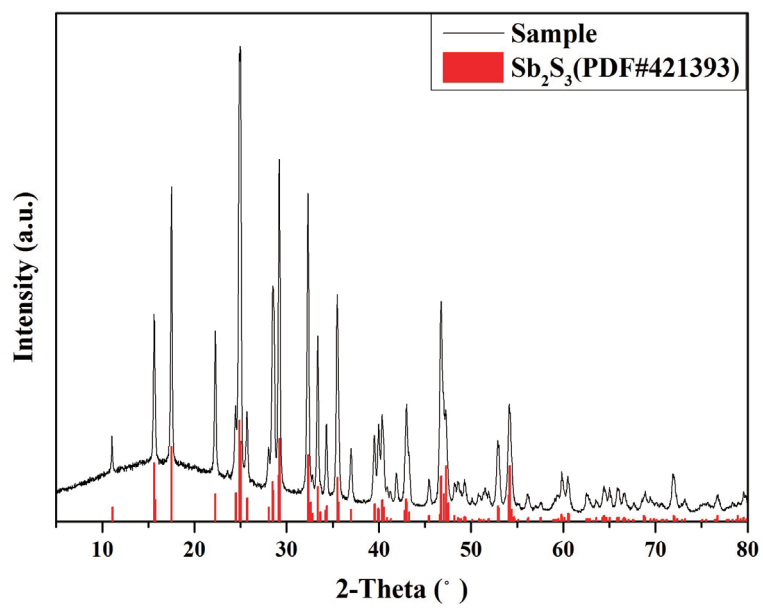

Fig. S12 SEM image of pristine Sb_2S_3.

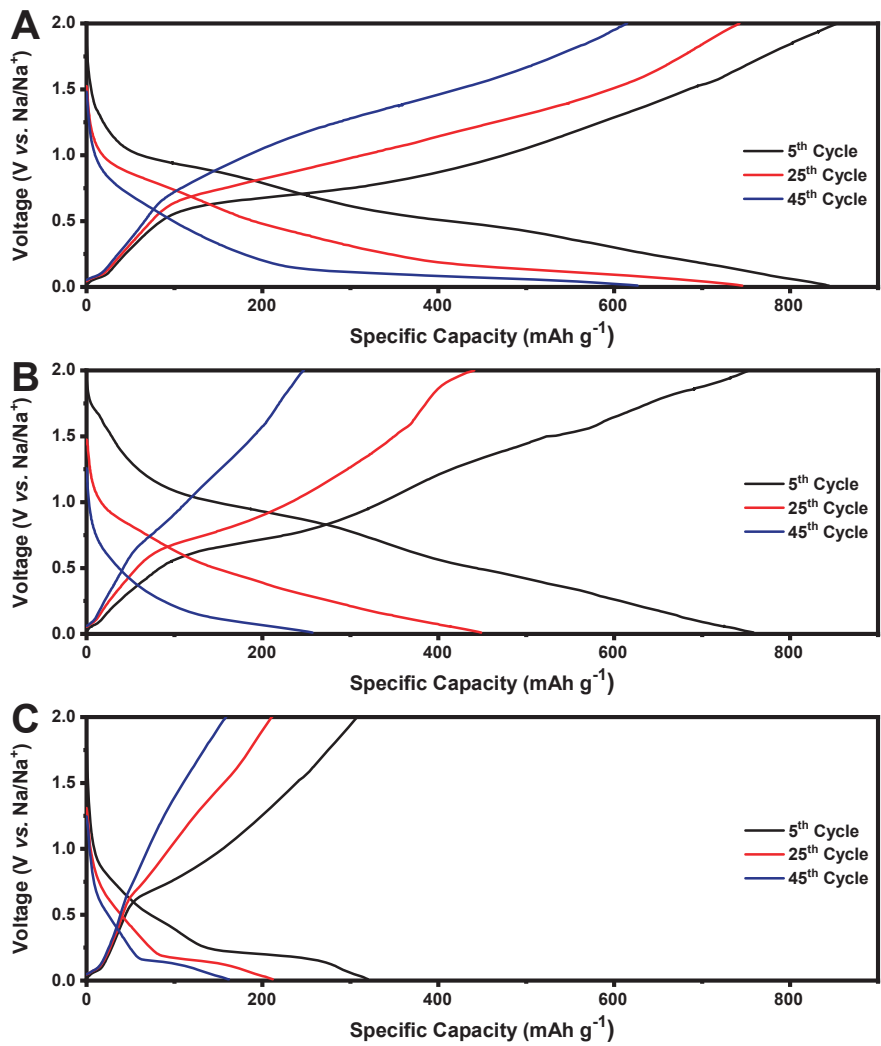**Fig. S13** XRPD pattern of pristine Sb_2S_3.

Fig. S14 Discharge/charge profiles of different cycles from long cycle performance test of different samples A) multi-shell Sb_2S_3, B) single-shell Sb_2S_3, C) pristine Sb_2S_3.
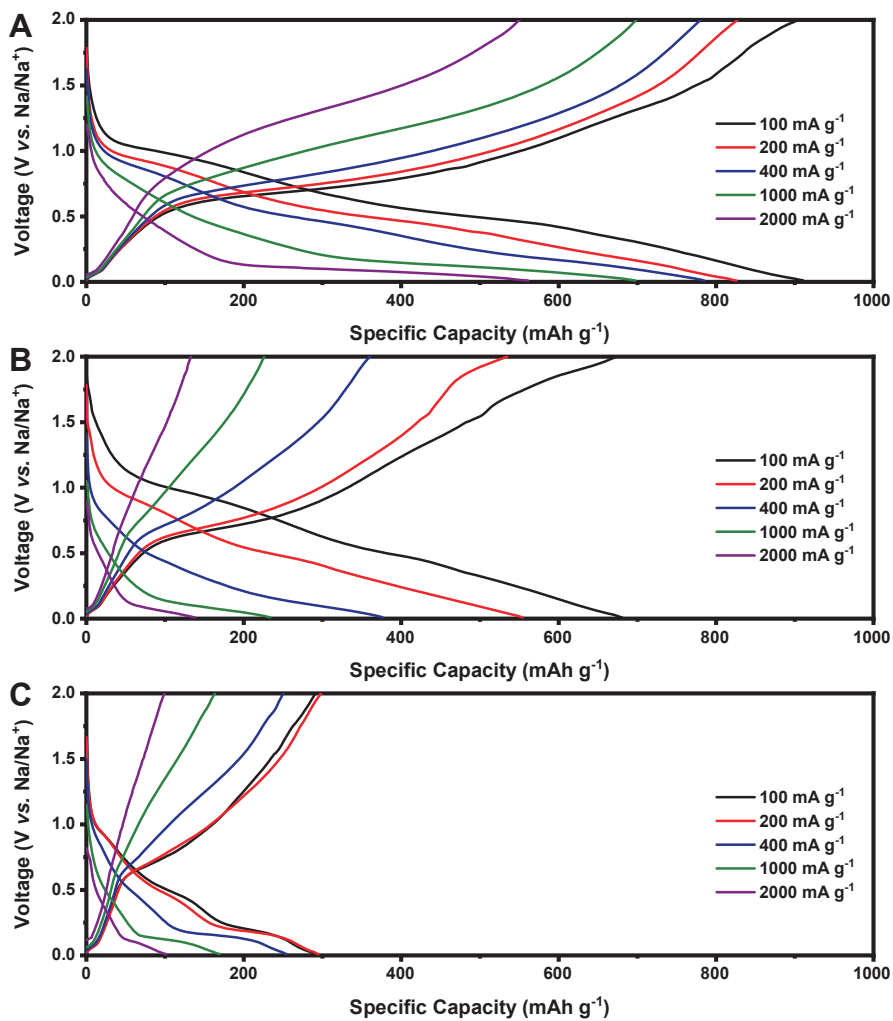
Fig. S15 Discharge/charge profiles under various current densities of different samples A) multi-shell Sb_2S_3, B) single-shell Sb_2S_3, C) pristine Sb_2S_3.
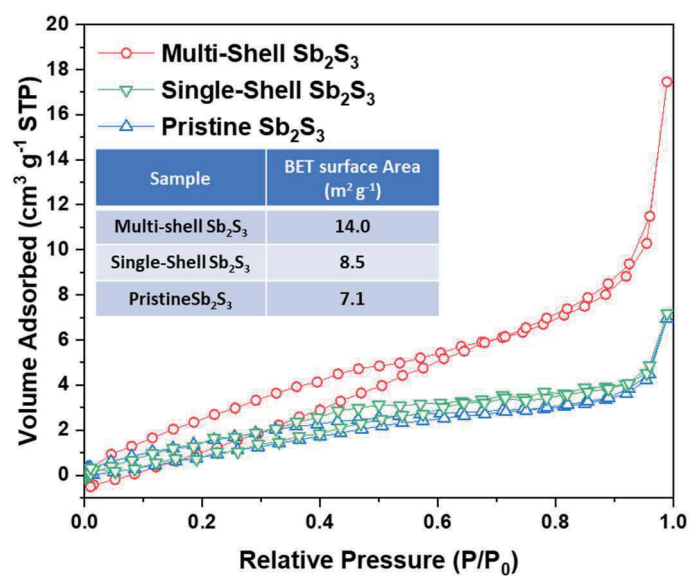
Fig. S16 Nitrogen adsorption isotherms measured for various Sb_2S_3 samples. The BET surface areas of the corresponding samples are listed in this figure.

Table S1 Comparison of as-synthesized multi-shell Sb_2S_3 in this work with some state-of-art anodes in the literatures

Material	Low current density	Reversible capacity under low current density	Highest current density	Reversible capacity under Highest current density	Ref.
Multi-shell Sb_2S_3	**0.1 A g^{-1}**	**909 mAh g^{-1}**	**2 A g^{-1}**	**604 mAh g^{-1}**	**This work**
ZnS-Sb_2S_3@C Core-Double Shell Polyhedron	0.1 A g^{-1}	630 mAh g^{-1}	0.8 A g^{-1}	391 mAh g^{-1}	[1]
Sb_2S_3 added bio-carbon	0.1 A g^{-1}	1113 mAh g^{-1}	6 A g^{-1}	369 mAh g^{-1}	[2]
1D van der Waals Sb_2S_3	0.1 A g^{-1}	863 mAh g^{-1}	2 A g^{-1}	337 mAh g^{-1}	[3]
Sb_2S_3/carbon fiber cloth	0.5 A g^{-1}	758 mAh g^{-1}	15 A g^{-1}	416 mAh g^{-1}	[4]
SnS_2/Sb_2S_3@rGO	0.1 A g^{-1}	685 mAh g^{-1}	4 A g^{-1}	567 mAh g^{-1}	[5]
SnS@NC microboxes	0.1 A g^{-1}	607 mAh g^{-1}	1 A g^{-1}	456 mAh g^{-1}	[6]
Cobalt sulfide MSNB	0.1 A g^{-1}	524 mAh g^{-1}	5 A g^{-1}	346 mAh g^{-1}	[7]
MoS_2/C microtubes	0.2 A g^{-1}	564 mAh g^{-1}	10 A g^{-1}	401 mAh g^{-1}	[8]
Ultrathin $Ti_2Nb_2O_9$ Nanosheets	0.05 A g^{-1}	237 mAh g^{-1}	4 A g^{-1}	134 mAh g^{-1}	[9]
N-Doped C@$Zn_3B_2O_6$	0.1 A g^{-1}	358 mAh g^{-1}	1 A g^{-1}	173 mAh g^{-1}	[10]
Hierarchical Hollow	0.2 A g^{-1}	383 mAh g^{-1}	10 A g^{-1}	339 mAh g^{-1}	[11]

NiSe$_2$@Carbon					
Sb Nanorod Encapsulated in Carbon	0.1 A g^{-1}	621 mAh g^{-1}	10 A g^{-1}	375 mAh g^{-1}	[12]
N/S-rGO@ZnSnS$_3$	0.1 A g^{-1}	655 mAh g^{-1}	2 A g^{-1}	257 mAh g^{-1}	[13]

[1]   S. Dong, C. Li, X. Ge, Z. Li, X. Miao, L. Yin, *ACS Nano* **2017**, 11, 6474.

[2]   V. Mullaivananathan, N. Kalaiselvi, *Carbon* **2019**, 144, 772.

[3]   S. Yao, J. Cui, Z. Lu, Z.-L. Xu, L. Qin, J. Huang, Z. Sadighi, F. Ciucci, J. K. Kim, *Adv. Energy Mater.* **2017**, 7, 1602149.

[4]   S. Liu, Z. Cai, J. Zhou, M. Zhu, A. Pan, S. Liang, *J. Mater. Chem. A* **2017**, 5, 9169.

[5]   S. Wang, S. Liu, X. Li, C. Li, R. Zang, Z. Man, Y. Wu, P. Li, G. Wang, *Chem. Eur. J.* **2018**, 24, 3873.

[6]   S. Wang, Y. Fang, X. Wang, X. W. Lou, *Angew. Chem. Int. Ed.* **2019**, 58, 760.

[7]   X. Wang, Y. Chen, Y. Fang, J. Zhang, S. Gao, X. W. Lou, *Angew. Chem. Int. Ed.* **2019**, 58, 2675.

[8]   Q. Pan, Q. Zhang, F. Zheng, Y. Liu, Y. Li, X. Ou, X. Xiong, C. Yang, M. Liu, *ACS Nano* **2018**, 12, 12578.

[9]   L. Shen, Y. Wang, H. Lv, S. Chen, P. A. van Aken, X. Wu, J. Maier, Y. Yu, *Adv. Mater.* **2018**, 30, 1804378.

[10]   S. Wang, X. B. Zhang, *Adv. Mater.* **2019**, 31, 1805432.

[11]   P. Ge, S. Li, L. Xu, K. Zou, X. Gao, X. Cao, G. Zou, H. Hou, X. Ji, *Adv. Energy Mater.* **2019**, 9, 1803035.

[12]   C. Cui, J. Xu, Y. Zhang, Z. Wei, M. Mao, X. Lian, S. Wang, C. Yang, X. Fan, J. Ma, C. Wang, *Nano Lett.* **2019**, 19, 538.

[13]   X. Liu, Y. Hao, J. Shu, H. M. K. Sari, L. Lin, H. Kou, J. Li, W. Liu, B. Yan, D. Li, J. Zhang, X. Li, *Nano Energy* **2019**, 57, 414.

Chapter 6 : Revealing the Origin of Improved Reversible Capacity of Dual-Shell Bismuth Boxes Anode for Potassium Ion Batteries

6.1 Introduction and Significance

A significant improvement in the reversible capacity was achieved for nanostructured alloy anodes. However, even though a large amount of nanostructured alloy anodes were applied in rocking-chair batteries, due to the poor temporal resolution of lab-based X-ray powder diffraction and the lack of sufficient information about chemical properties of these anodes, the origin of their improved reversible capacity remains unclear. Here, we combine *operando* synchrotron-based X-ray powder diffraction with high temporal resolution and *ex-situ* X-ray absorption near edge structure spectroscopy to study the double-shell nanostructured bismuth boxes as alloy anodes to reveal the origin of their improved reversible capacity.

The key findings of this work are:

1. The first synthesis of double-shell nanostructured bismuth boxes;

2. Identifying the key role of nanostructure in improving the reversible capacities;

3. Revealing different origins of the improved reversible capacities of nanostructured alloy anodes under various current densities;

4. Guidance for the rational design and engineering of nanostructured alloy anodes

6.2 Revealing the origin of improved reversible capacity of dual-shell bismuth boxes anode for potassium ion batteries

This chapter is included as it appears as a journal paper published by Fangxi Xie, Lei Zhang, Biao Chen, Dongliang Chao, Qinfen Gu, Bernt Johannessen, Mietek Jaroniec, Shizhang Qiao, Revealing the origin of improved reversible capacity of dual-shell bismuth boxes anode for potassium ion batteries, *Matter*, 2019, *accepted for publication*.

Statement of Authorship

Title of Paper	Revealing the Origin of Improved Reversible Capacity of Dual-Shell Bismuth Boxes Anode for Potassium Ion Batteries
Publication Status	☐ Published ☐ Accepted for Publication ☑ Submitted for Publication ☐ Unpublished and Unsubmitted w ork w ritten in manuscript style
Publication Details	Fangxi Xie, Lei Zhang, Biao Chen, Dongliang Chao, Qinfen Gu, Bernt Johannessen, Mietek Jaroniec, Shizhang Qiao, Revealing the origin of improved reversible capacity of dual-shell bismuth boxes anode for potassium ion batteries, Matter, submitted.

Principal Author

Name of Principal Author (Candidate)	Fangxi Xie
Contribution to the Paper	Research Plan, material synthesis, most of the characterizations and data analysis, electrochemical characterization, and manuscript Draft
Overall percentage (%)	54%
Certification:	This paper reports on original research I conducted during the period of my Higher Degree by Research candidature and is not subject to any obligations or contractual agreements with a third party that would constrain its inclusion in this thesis. I am the primary author of this paper.
Signature	Date 2019. May. 10.

Co-Author Contributions

By signing the Statement of Authorship, each author certifies that:

i.   the candidate's stated contribution to the publication is accurate (as detailed above);

ii.   permission is granted for the candidate in include the publication in the thesis; and

iii. the sum of all co-author contributions is equal to 100% less the candidate's stated contribution.

Name of Co-Author	Lei Zhang
Contribution to the Paper	Design of research plan, discussion of synthesizing procedure and manuscript revision 11%
Signature	Date 11st of 2019

Name of Co-Author	Biao Chen
Contribution to the Paper	Design of research plan, and manuscript revision 5%

Signature		Date	May.10, 2019

Name of Co-Author	Dongliang Chao
Contribution to the Paper	Discussion of this manuscript and manuscript revision 5%

Signature		Date	11st. 05, 2019.

Name of Co-Author	Qinfen Gu
Contribution to the Paper	Discussion of Operando powder diffraction characterizations and X-ray Absorption Spectroscopy 5%

Signature		Date	12end 05 2019

Name of Co-Author	Bernt Johannessen
Contribution to the Paper	Discussion of X-ray Absorption Spectroscopy 5%

Signature		Date	10.5.19

Name of Co-Author	Mietek Jaroniec			
Contribution to the Paper	Discussion of this manuscript and manuscript revision 5%			
Signature		Date	May 12, 2019	

Name of Co-Author	Shizhang Qiao			
Contribution to the Paper	Supervision of the work, discussion of this manuscript and manuscript evaluation 10%			
Signature		Date	May 13, 2019	

Please cut and paste additional co-author panels here as required.

Revealing the origin of improved reversible capacity of dual-shell bismuth boxes anode for potassium ion batteries

Fangxi Xie,[1‡] Lei Zhang,[1‡] Biao Chen,[1] Dongliang Chao,[1] Qinfen Gu,[2] Bernt Johannessen,[2] Mietek Jaroniec,[3] and Shi-Zhang Qiao*[1,4]

[1] School of Chemical Engineering, The University of Adelaide, Adelaide, SA 5005, Australia

[2] Australian Synchrotron (ANSTO), 800 Blackburn Rd, Clayton, VIC 3168, Australia

[3] Department of Chemistry and Biochemistry, Kent State University, Kent, Ohio 44242, United States

[4] Lead Contact

E-mail: s.qiao@adelaide.edu.au

Summary

Nanostructured alloy anodes have been successfully used in several kinds of rocking-chair batteries. However, a full picture of the origin of their improved reversible capacity remains elusive. Here, we combine *operando* synchrotron-based X-ray powder diffraction (XRPD) and *ex-situ* X-ray absorption near edge structure spectroscopy (XANES) to study the double-shell structured bismuth boxes as anodes in potassium ion batteries to reveal the origin of their improved capacity. The nanostructured bismuth anode offers an enhanced capability to tolerate the volume expansion under a low current density of 0.2 C, resulting in a more complete alloy reaction and improved reversible capacity. Additionally, under a high current density of 2 C, nanostructured bismuth anode with larger surface area offers more sites to electrochemically alloy with potassium and results in a lower average oxidation state of bismuth. These findings offer a guidance for the

1

rational design and engineering of electrode materials according to the current density for rocking chair batteries.

KEYWORDS: multi-shell particles, hollow structures, potassium-ion batteries, anode materials, *operando* synchrotron XRPD

Introduction

Rocking-chair batteries, such as lithium, sodium, potassium, and calcium ion batteries, are widely applied as electrical energy storage devices for portable electronic devices and electrical vehicles. On their anode side, alloy anodes with much higher theoretical capacity than the conventional intercalation anodes are considered as a superior choice.[1-11] Nonetheless, these alloy anodes often suffer the larger volume expansion and consequently, the capacity fading.[5-7,9] Therefore, various nanostructured alloy anodes have been developed.[3,4,9] Although a significant improvement of their reversible capacity has been achieved, its origin remains still unclear.[6,7]

To reveal the origin of the improved capacity, various approaches have been explored. The most common approach involves X-ray powder diffraction (XRPD) to observe the electrochemical alloying process. Especially, the previous studies involving the XRPD monitoring of the alloying process of silicon anodes in lithium ion batteries, suggest that the reduction of the particle size or film thickness leads to the suppression of $Li_{15}Si_4$ phase, which results in the change of the final product of electrochemical reaction and increases the reversible capacity.[7,12,13] Additionally, the final product of the alloying reaction of bismuth, another alloy anode, in sodium ion batteries is affected by varying the particle size. The final product derived from nanosized bismuth and sodium is cubic Na_3Bi, while the one originating from microsized bismuth is hexagonal Na_3Bi.[14] The change in the electrochemical reaction-path due to nanosizing the alloy anodes could be the reason of the improved reversible capacity.[7,14,15] However, most of the reported results refer to the

2

electrochemical reaction paths under small current density. The difference in the behavior of nanostructured and bulky alloy anodes under high current density remains elusive due to the poor temporal resolution of lab-sourced XRPD, which might require a relatively long acquisition time for obtaining proper crystallographic information.[16-19] To resolve this issue, electrochemical characterization approaches with high temporal resolution have been applied. Several reports about anodes which contains alloy elements suggest that the origins of higher reversible capacity are the enhanced pseudocapacitive response or fast ion kinetics.[20-24] However, the characterization of electrochemical reactions bases mainly on the electrical signals while the information about chemical properties, such as the phase evolution or the oxidation states, is lacking. More importantly, the conclusion about the enhanced pseudocapacitive contribution is in contradiction with the suppression of certain electrochemical reactions observed by X-ray powder diffraction. At present, most of the reports are devoted to either the phase evolution under low current density or the electrochemical response under high current density. Therefore, due to the rarely reported phase evolution of nanostructured alloy anodes under high current density and the lack of chemical properties from electrochemical characterization, a full picture of the origin of increasing reversible capacity of nanostructured alloy anodes remains unclear.

Herein, we report the first synthesis of double-shell structured bismuth boxes. Their electrochemical process as an anode for potassium ion batteries is studied by combining an *operando* synchrotron-based XRPD with high temporal resolution and *ex-situ* X-ray absorption near edge structure (XANES).[16,18,19] By employing this nanostructured bismuth material and comparing its electrochemical behavior with that of microsized bismuth, a full picture of the origin of the improved reversible capacity of nanostructured alloy anodes is revealed. The improved reversible capacity of nanostructured bismuth under low current density originates from numerous

3

internal voids able to accommodate the large volume expansion, while that under high current density originates from large amount of electrochemical active sites associated with high surface area. This study points out that the origins of the improved reversible capacities under various current densities are different. This demonstrates the key role of the nanostructure in improving the reversible capacity of alloy anodes. These findings offer guidance for the future rational design and engineering of nanostructured alloy anodes for rocking-chair batteries.

Results and discussion

The complete synthesis route of nanostructured bismuth anodes is illustrated in **Figure 1A**. As shown in Figure 1A and **Figure S1**, the uniform ZIF-8 (zeolitic imidazolate framework-8) cubes with a size of around 500 nm were selected as the initial template and synthesized by using a slightly modified approach reported elsewhere.[25] After a series of modified sulfidations reported by us previously, the double-shell zinc sulfide boxes with slight indentations on their surface are clearly seen (**Figure S2**).[26] As suggested in our previous report, due to the difference in the solubility product constants, the zinc cations in the as-prepared sample are replaced by bismuth cations via a facile room temperature cation-exchange method.[26] The scanning electron microscope (SEM) and transmission electron microscope (TEM) images (**Figure S3**, **S4**) show that the double-shell box structure is maintained during this exchange process. After surface coating with polydopamine and subsequent calcination, the carbon-coated double-shell bismuth hollow boxes (C@DSBC) are obtained and studied by SEM and TEM imaging analysis. As shown in **Figure 1B** and **Figure S5**, the uniform cubic shape remains after coating and subsequent calcination. The TEM and scanning transmission electron microscopy (STEM) images (**Figure 1C** and **S6**) show a porous dual-shell structure of these boxes with the thickness of each shell estimated to be around several nanometers. The high-angle annular dark-field STEM (HAADF-
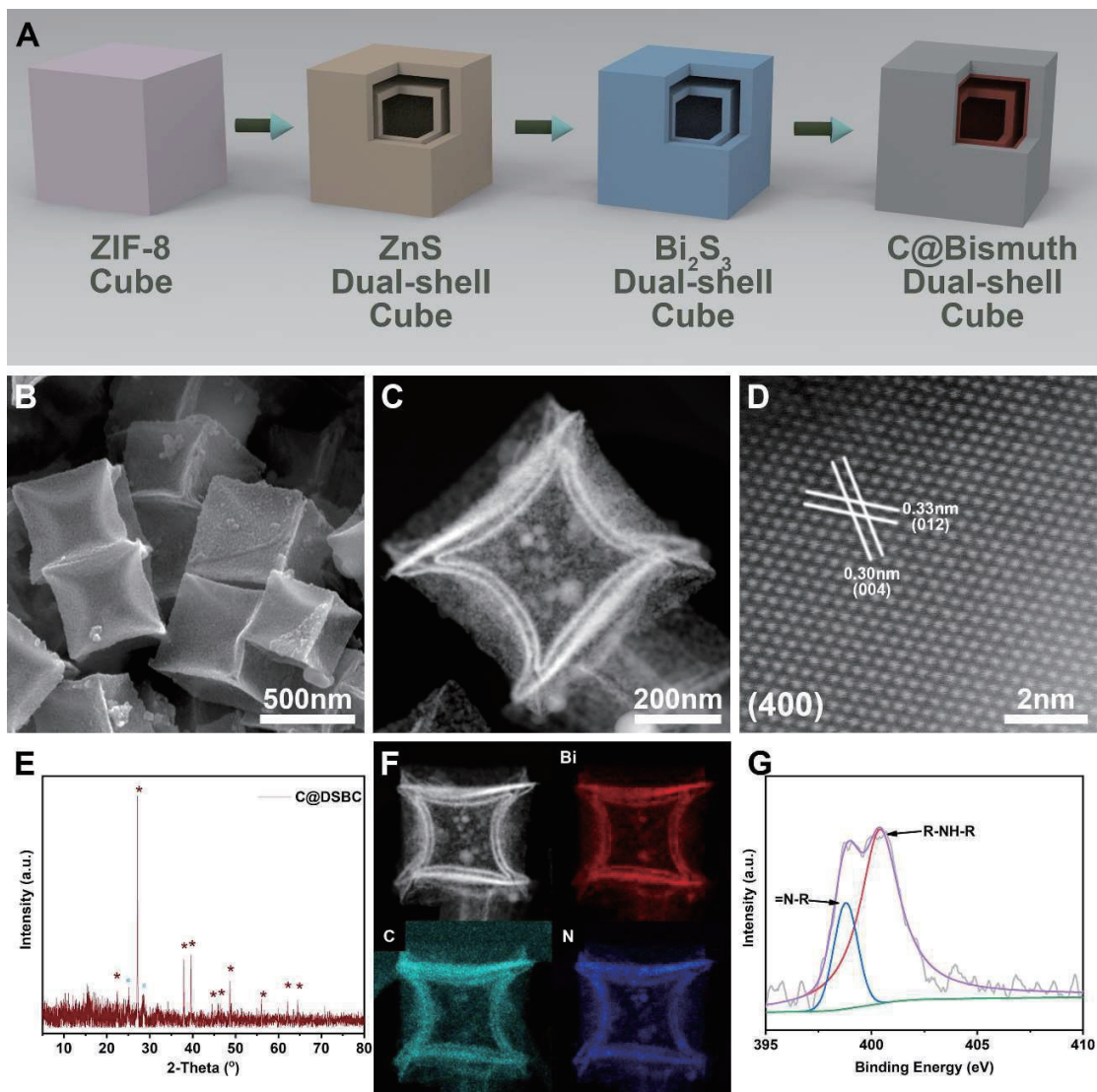
4

Figure 1. Synthesis procedure, morphology and physicochemical characterization of C@DSBC: A.) Scheme illustrating the synthetic procedure of C@DSBC; B.) SEM image of C@DSBC; C, D) HAADF-STEM images; E.) XRPD-spectrum (* represents bismuth and # represents bismuth sulfide); F.) HAADF-STEM elemental mapping; G.) high-resolution nitrogen XPS spectrum.

STEM) image (**Figure 1D**) shows the lattice spacings of 0.33 nm and 0.30 nm with an interfacial angle of 56° indexed as (012) and (004) facets of bismuth, respectively. A combination of these data with those of XRPD data shown in **Figure 1E** reveals that the composition in the as-prepared

sample is mainly rhombohedral bismuth phase. Additionally, the STEM elemental mapping images (**Figure 1F**) illustrate the even distribution of bismuth, carbon, and nitrogen, indicating that the nitrogen-doped carbon is homogenously coats the surface of bismuth boxes. The N-doped nature of the carbon coating is also demonstrated by X-ray photoelectron spectroscopy (XPS) (**Figure 1G, S7A** and **S7B**).[27,28] Furthermore, the Raman spectrum (**Figure S8**) shows that this carbon coating is highly amorphous, while the carbon content is around 7% according to the thermogravimetric analysis (**Figure S9**). [29-31]

The microsized bismuth is selected as the control sample to offer a more comprehensive understanding of the improved reversible capacity of nanostructured alloy anodes. The detailed characterizations are shown in **Figure S10** (SEM image and XPS survey spectrum). As shown in **Figure 2A**, the C@DSBC sample achieves an initial reversible capacity of 351 mAh g^{-1} with an initial coulombic efficiency of 52%. This low initial coulombic efficiency can be attributed to the irreversible reaction of K$^+$ with Bi, the decomposition of electrolyte and the formation of solid electrolyte interface (SEI).[32,33] Despite of the low initial coulombic efficiency, the subsequent discharging/charging curves of C@DSBC exhibit good overlays, suggesting the good stability of the previously formed SEI, which benefits the subsequent cycling stability. Some slight differences between microsized bismuth and double-shell structure can be found in **Figure** 2A and **2B**. The initial discharging curve for C@DSBC shows several plateaus. On the other side, the discharging curve of microsized bismuth features one plateau. The cyclic voltammetry (CV) curves show only one significant reduction peak for microsized bismuth (**Figure S11**), while much higher anodic current response can be observed before 0.25V on the CV curves of C@DSBC (**Figure 2C**). This indicates that there are differences between C@DSBC and microsized bismuth samples during their initial cycling processes. After the initial cycles, as shown in **Figure 2D**, C@DSBC exhibited
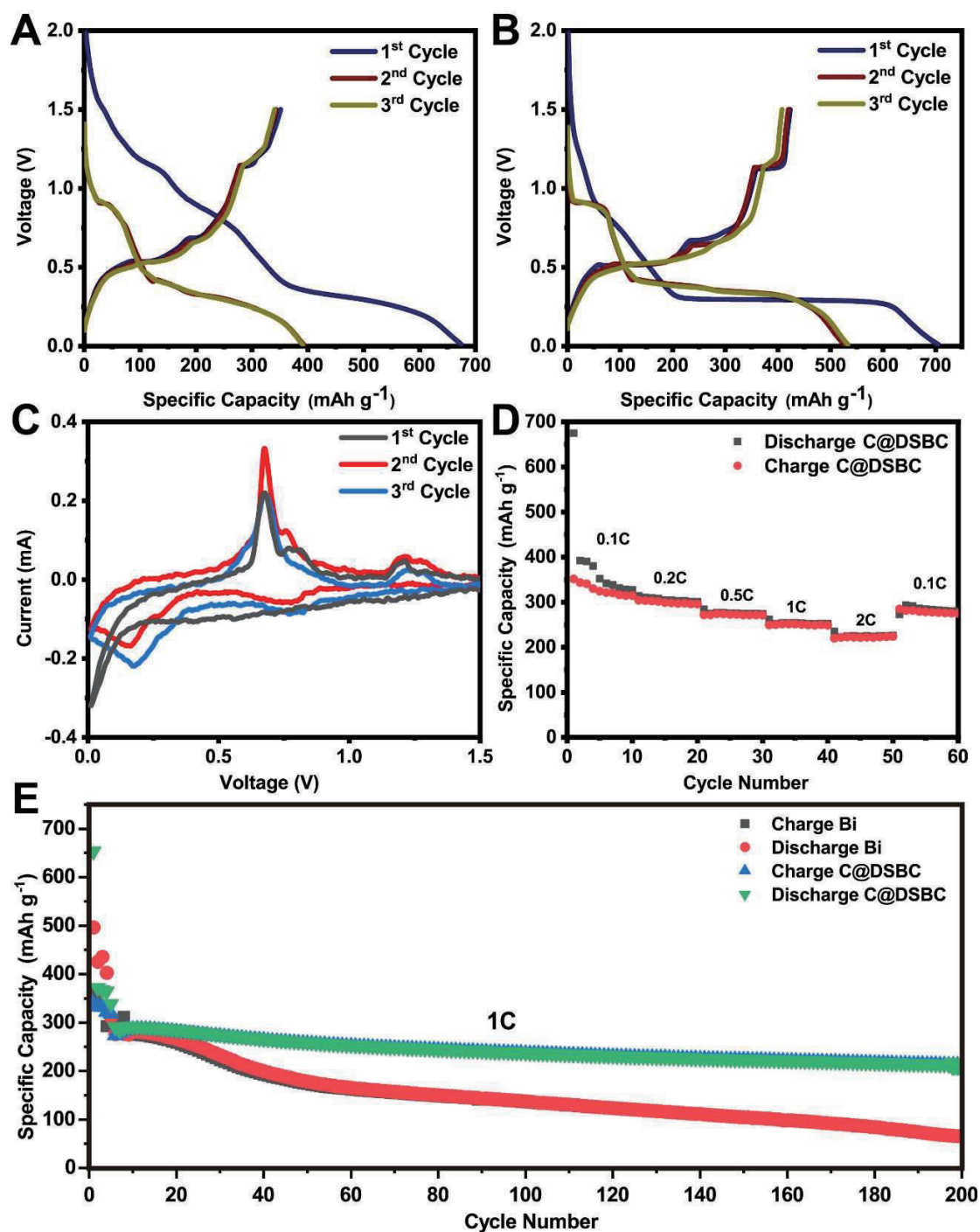
6

Figure 2 Electrochemical performance of bismuth samples: Initial cycling curves of A.) C@DSBC; B.) microsized bismuth; C.) initial CV curves of C@DSBC; D.) rate performance of C@DSBC; E.) long cycling performance of C@DSBC and microsized bismuth.

a good rate performance as an anode for potassium ion batteries. Specifically, it delivered the reversible capacities of 340, 302, 274, 251, and 222 mAh g^{-1} under the current densities of 40, 80, 200, 400, and 800 mA g^{-1}, corresponding to 0.1, 0.2, 0.5, 1, and 2C, respectively. As regards the long-cycling durability, C@DSBC exhibited an enhanced durability as compared to that of the microsized bismuth. Specifically, as shown in **Figure 2E**, during the initial period, both bismuth samples exhibited stable reversible specific capacities of around 300 mAh g^{-1}. After being cycled for around 20 cycles, a more significant decrease is observed for the reversible capacity of the microsized bismuth, while the reversible capacity of C@DSBC remains over 300 mAh g^{-1}. After cycling for 200 cycles, the reversible capacity of the microsized bismuth is 65 mAh g^{-1}, corresponding to the capacity loss of 77.0% during 200 cycles. On the contrary, the reversible capacity of C@DSBC is maintained over 200 mAh g^{-1}, which corresponds to the capacity decay of 0.13% per cycle, showing a good durability of C@DSBC as an anode for potassium ion batteries.

The electrochemical characterization suggests that C@DSBC behaves differently from microsized bismuth during the initial cycling. The difference in electrochemical reactions during the cycling process shown by various synchrotron-based techniques reveals the origin of the improved capacity.

Firstly, the cycling process of both C@DSBC and microsized bismuth under low current densities are monitored by *operando* XRPD. As previously reported, the electrochemical reaction of bismuth and potassium ion during the discharging process can be represented by the following equations[32,33]:

$Bi \rightarrow KBi_2 \rightarrow K_3Bi_2 \rightarrow K_3Bi$

In our *operando* XRPD study, during the cycling process of double-shell bismuth and microsized bismuth, the most significant difference appears during transformation from K_3Bi_2 to K_3Bi. During
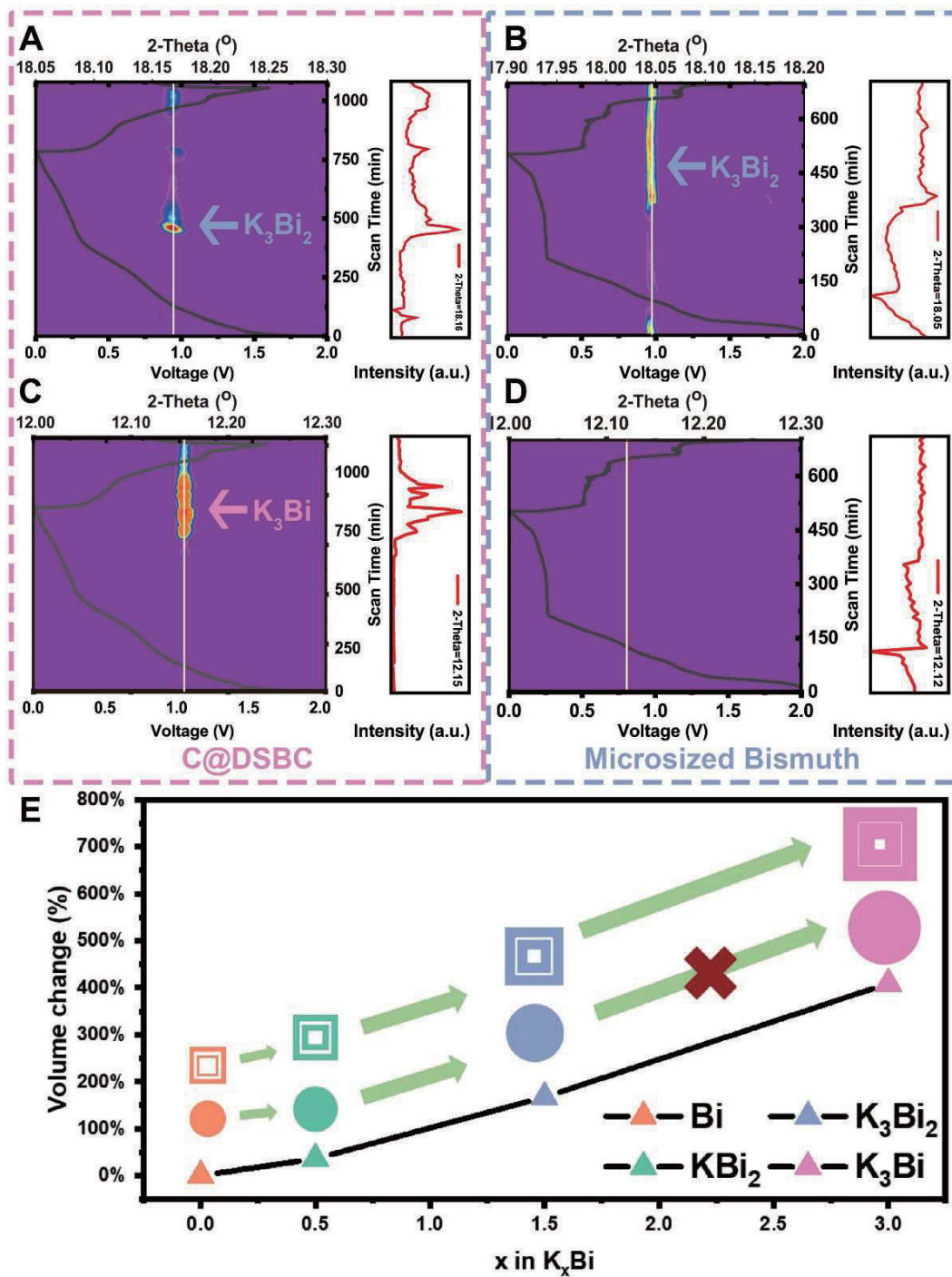
8

Figure 3. Origin of superior electrochemical performance under low current density: Comparison of contour plots of the *operando* XRPD with superimposed voltage profiles shown for selected ranges of K_3Bi_2 (A, B) and K_3Bi (C, D). Scheme of superior electrochemical performance of C@DSBC under low current density (panel E).

the initial discharging process of double-shell bismuth, as shown in **Figure 3A**, the reflection peak is assigned to $(11\bar{5})$ facet of K_3Bi_2, which is located at $18.18°$, and appears for the discharging taking place to the voltage of around 0.3V. With the progress of electrochemical alloying reaction, the intensity of reflection peak of K_3Bi_2 starts to decrease and the reflection peak almost disappears when the voltage approaches a value of 0.2V. Subsequently, as shown in **Figure 3C**, when the intensity of reflection of K_3Bi_2 decreases, the (222) peak of K_3Bi, which is located at $12.16°$, appears, indicating the K_3Bi_2 phase is going through a transformation to K_3Bi. When the charging process starts, the intensity of K_3Bi decreases significantly and the intensity of K_3Bi_2 increases subsequently and decreases afterward, indicating the superior reversibility of C@DSBC as an anode for potassium ion batteries. As a comparison, the microsized bismuth was also subjected to the same process with the same current density. Interestingly, as shown in **Figure 3B**, the reflection of K_3Bi_2 appears around the middle of the discharging plateau. The intensity of this reflection peaks only decreases partially with proceeding electrochemical reaction. Afterward, at the initial stage of charging the intensity of reflection for K_3Bi_2 only slightly decreases, indicating that most of K_3Bi_2 remains unreacted and the reversibility of microsized bismuth is poor. More importantly, during the discharging process of bismuth, as shown in **Figure 3D**, the intensity of K_3Bi phase is low. As compared with the high intensity of K_3Bi reflection peak in the case of C@DSBC, one can conclude that there is no significant formation of K_3Bi phase. Therefore, under the low current density, the main difference between the electrochemical reactions of these two materials is the transformation from K_3Bi_2 to K_3Bi. This result indicates that the electrochemical alloy reaction between C@DSBC and potassium is more complete than that between microsized bismuth and potassium. Initially, the main final product from electrochemical reaction of C@DSBC is K_3Bi, while the one in the case of microsized bismuth is K_3Bi_2. In the previous reports, both Huang *et.al*

10

and Lei *et.al* reported that the normalized volume expansion during the electrochemical reaction is over 400% from Bi to K_3Bi.[32,33]Combining with the data of the volume expansion from previous studies, as shown in the scheme (**Figure 3E**), this difference might come from the much higher strain and volume expansion during the phase transformation process from K_3Bi_2 to K_3Bi. With the large internal voids, the C@DSBC sample is capable to accommodate larger volume expansion. On the contrary, the microsized bismuth can only tolerate smaller volume expansion, resulting in a change of electrochemical reaction path. Therefore, the final main product after initial electrochemical reaction of microsized bismuth is K_3Bi_2, corresponding to the volume expansion of around 167%. To sum up, nanostructured alloy anodes offer the enhanced capability to accommodate large volume expansion, resulting in a more complete alloy reaction and consequently higher reversible capacity under low current density.

When the electrochemical reaction occurs under a relatively high current density, the electrochemical reaction might be quite different from that under low current density. The electrochemical reaction taking place on C@DSBC under high current density (2C) is explored by combining *operando* XRPD and *ex-situ* XANES. The *operando* XRPD reveals that the reflection intensity of bismuth in C@DSBC decreases significantly with the electrochemical process (**Figure 4A**). On the contrary, the reflection intensity observed for microsized bismuth is only slightly reduced (**Figure 4B**), indicating that more bismuth in this sample remains unreacted. This finding demonstrates that the electrochemical alloying reaction of bismuth in C@DSBC with potassium is more complete than that in microsized bismuth. However, surprisingly, unlike the electrochemical process under low current density mentioned above, there is no significant change in the intensities of both K_3Bi_2 phase and K_3Bi phase (**Figure S12**) on the spectra of C@DSBC. This finding indicates that the main electrochemical reaction of C@DSBC under the relatively
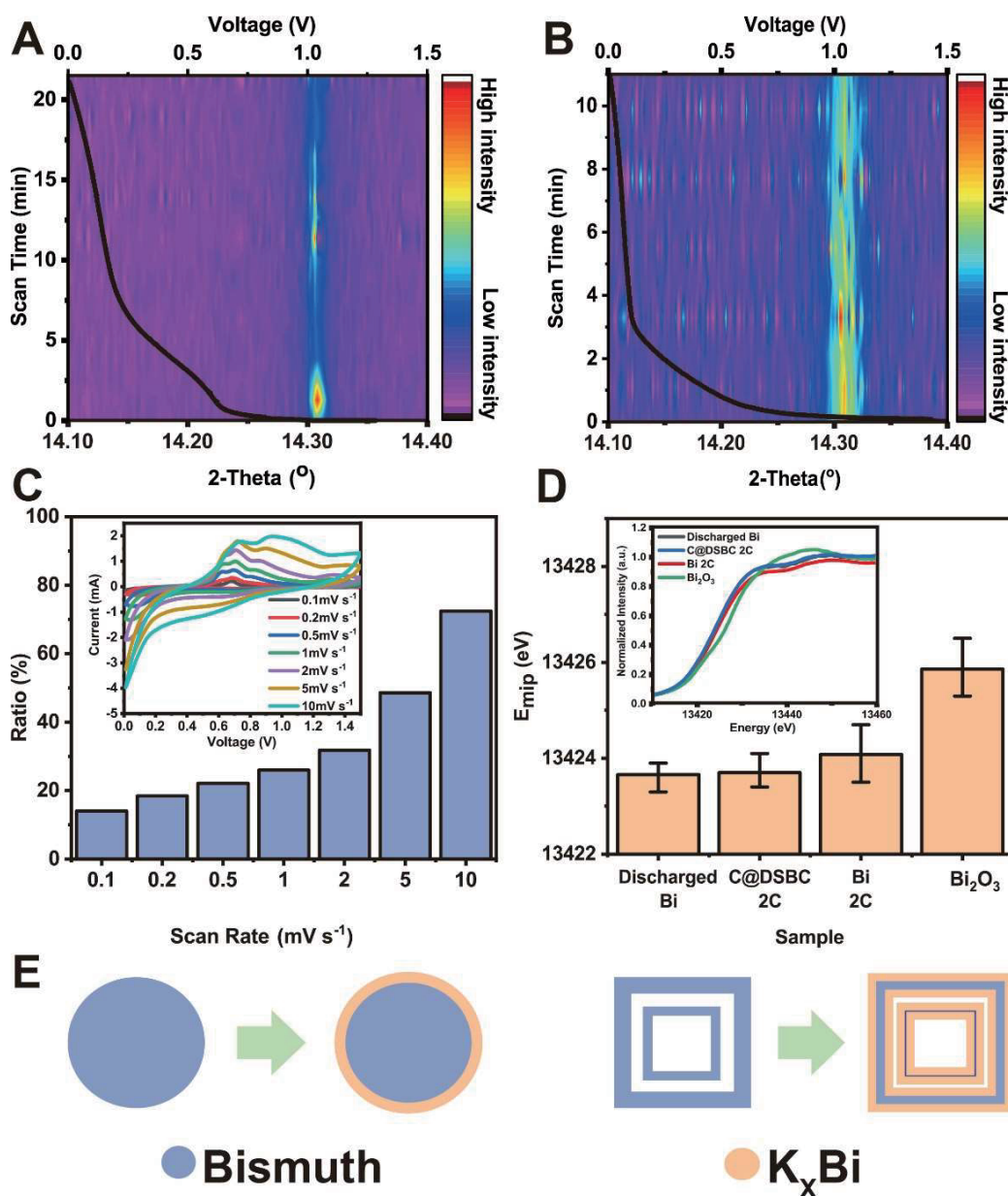
11

Figure 4. Origin of superior electrochemical performance under high current density: Comparison of contour plots of the *operando* XRPD with superimposed voltage profiles shown for bismuth reflection of different samples: C@DSBC (A) and microsized bismuth (B). The pseudocapacitive contribution obtained for C@DSBC (panel C with inset showing the CV curves of C@DSBC at various sweep rates). The corresponding E_{mip} for various samples (panel D with inset showing the XANES spectra of various samples. Scheme illustrating the superior electrochemical performance of C@DSBC under high current density (panel E).

high current density could be a surface-driven adsorption reaction. This finding is also confirmed by the kinetics analysis of C@DSBC. As shown in **Figure 4C**, the contribution arising from pseudocapacitive behavior of double-shelled structured bismuth, which is calculated from the CV data for various sweep rates (Figure 4C inset), increases to over 70 % at the scan rate of 10 mV s^{-1}. This indicates that the main contribution to the reversible capacity might originate from the surface-driven adsorption reactions but not the alloying reaction with crystallized product mentioned above at the low current density. This might be the reason why no significant crystallized alloy of potassium and bismuth is detected by *operando* XRPD during cycling under a relatively high current density. Therefore, the *ex-situ* XANES spectroscopy was employed to reveal the difference of electrochemical reaction product from both samples.

The microsized bismuth sample discharged to 0.01V with potassium as the counter electrode under a low current density and bismuth oxide (Bi_2O_3) were selected as the standard samples. In the XANES spectra, the energy inflection point of the Bi-L_{III} edge indicates the average oxidation state of bismuth in the corresponding samples. On these *ex-situ* spectra (Figure 4D inset), the Bi-L_{III} edge of C@DSBC after discharging under the current density of 2C is closer to that of the discharged Bi standard sample, compared with that of the discharged microsized bismuth. To illustrate clearly this point, the position of the main inflection point (E_{mip}) is selected as the descriptor of oxidation state of bismuth in the corresponding samples (**Figure S13**). As shown in the bar graph (**Figure 4D**), the bismuth in C@DSBC shows similar average oxidation state corresponding to E_{mip} of 13423.7 eV to the discharged Bi sample (13423.66 eV), while the microsized bismuth sample shows higher oxidation state (13424.08 eV). As suggested by **Figure 4E**, this difference in the oxidation state might indicate that the electrochemical reaction under high current density is dominated by surface-driven adsorption reactions. The lower average

13

oxidation state of C@DSBC indicates that its electrochemical reaction generates more alloy product, resulting in lower average oxidation state. This might come from the higher surface area of 33.1 m^2 g^{-1} of C@DSBC as compared to 9.2 m^2 g^{-1} of microsized bismuth (**Figure S14**). Therefore, the nanostructured alloy anodes offer larger surface area and more electrochemical active sites to react with alkaline ions, resulting in larger consumption of electrode materials, lower average oxidation states and consequently, higher reversible capacities under high current density.

Combination of the results from *operando* XRPD and *ex-situ* XANES allows for two main conclusions. First, the improved reversible capacities of nanostructured alloy anodes in batteries under various current densities have different origins. For cycling under low current density, the key is a more complete alloy reaction resulting from the change of electrochemical alloying reaction path. Under the condition of high current density, the surface-driven adsorption reactions are more important, which result in larger consumption of electrode materials and consequently, lower average oxidation state. Second, the key role of the nanostructure in enhancing the electrochemical performance of alloy anodes is identified. Specifically, the higher reversible capacity under low current density originates from high capability of nanostructured alloy anode to accommodate larger volume expansion than that in the microsized sample. In the case of high current density, the higher reversible capacity originates from larger surface area of nanostructured alloy anode, which offers more electrochemical active sites to react with alkali ions.

Conclusions

In summary, we have constructed new dual-shell structured bismuth boxes as anodes for potassium ion batteries. Through combining several synchrotron-based techniques and employing dual-shell bismuth boxes permitted us to reveal the origins of the improved reversible capacity of nanostructured alloy anodes under various current densities. The origin under low current density

14

is the change of electrochemical reaction path, which is derived from the enhanced capability of nanostructured anode on tolerating the larger volume expansion. Under high current density, the origin of this improvement is associated with surface-driven electrochemical reactions promoted by larger surface area of nanostructured anodes. This finding offers guidance for the rational design and engineering electrodes for various applications.

Experimental Procedure:

Synthesis of materials: Synthesis of ZIF-8 Cubes: First, 55 mg of zinc acetate dihydrate, 8 mg of hexadecyl trimethyl ammonium bromide (CTAB), and 1.14 g of 2-methylimidazole were dissolved in 80 mL of deionized (DI) water. [25] Next, the resulting solution was mixed and stirred for 5 min at room temperature. The as-prepared mixed solution was transferred into a Teflon-lined autoclave and placed in a 120 °C oven for 6 hours. After synthesis, the sample was washed with deionized water and ethanol for three times and dried at 60 °C overnight.

Synthesis of C@DSBC: 40 mg of the as-prepared ZIF-8 was transferred into a round bottom flask and dispersed in 30 mL of anhydrous ethanol under ultrasonication for 10 minutes. The flask was soaked into 80 °C oil bath. After that, a mixed solution containing 0.54 g of thioacetamide and 10 mL of anhydrous ethanol was added into the flask and the reaction was processed at 80 °C for half hour. The intermediate was collected by centrifugation and washed with anhydrous ethanol twice. Next, the as-prepared sample was redispersed in 20 mL of acetone, while another solution was prepared by dissolving 0.1 g of bismuth chloride in 20 mL of acetone. The former solution was poured into the latter one under magnetic stirring, which was stopped after three hours. The product was collected and washed with acetone and ethanol three times. Next, the as-prepared sample was redispersed in a solution containing 40 mg of Trizma® Base and 30 mL of distilled water. Finally, 6 mg of dopamine hydrochloride was added rapidly into the suspension under

15

intense stirring. The product was washed with ethanol and collected by centrifugation after 3-hour reaction at room temperature. The resulting sample was dried overnight in a vacuum oven and calcined in a tube furnace at 400 ^{O}C for 3 hours with a ramping rate of 3 ^{o}C per minute.

Materials characterization: XRPD data were collected on Rigaku MiniFlex 600 X-Ray Diffractometer. The field-emission SEM images were acquired on the FEI Quanta 450 FEG scanning electron microscope. The TEM images were taken on FEI Tecnai G2 Spirit. The STEM and HAADF-STEM images were taken on FEI Titan Themis. The *Operando* XRPD was conducted in the Powder Diffraction (PD) beamline of Australian Synchrotron (ANSTO) with a beamline wavelength of 0.5904 angstrom in a transmission mode. The coin-cells for *Operando* powder diffraction are modified from 2032 coin-cells with X-ray transparent windows made from Kapton film.[18] The *ex-situ* XANES spectra were collected in the X-ray Absorption Spectroscopy (XAS) beamline of Australian Synchrotron (ANSTO). The electrodes tested in XAS were taken from disassembled coin-cells and sealed by Kapton tape in an Argon-filled glove box. The electrodes were tested in a fluorescence mode. The discharged bismuth sample was prepared in a coin-cell using microsized bismuth and potassium as the cathode and anode, respectively. The coin-cell was discharged to 0.01V under a current density of 0.05C. The surface area was evaluated from nitrogen adsorption data measured at 77.3 K (ASAP 2020) using the Brunauer–Emmett–Teller (BET) method.

Electrochemical measurements: The electrochemical performance tests were carried out in 2032 type coin cells at room temperature. The working electrode consisted of active material (i.e., dual-shell bismuth and pristine bismuth), carbon black (Super P from VWR, supplied by Alfa Aesar) and binder (CMC, average M_w=~700,000, Sigma-Aldrich) using a weight ratio of 60:30:10, while the copper foil was employed as the current collector. The electrolyte was composed of 2.0 M

16

potassium bis(fluorosulfonyl) imide dissolved in 1,2-dimethoxyethane. Galvanostatic tests were performed on a Landt CT2001A battery testing system. The cyclic voltammetry data were collected on a Gamry 1000e electrochemical station.

ASSOCIATED CONTENT

Supporting Information. The Supporting Information is available free of charge. Figures of SEM, TEM images, XPS, Raman, thermogravimetric analysis, nitrogen adsorption isotherms, other electrochemical and other *Operando* powder diffraction data are available in Supporting Information.

AUTHOR INFORMATION

Corresponding Author and lead contact

*E-mail: s.qiao@adelaide.edu.au (S. Z. Qiao)

Author Contributions

F. Xie, L. Zhang, B. Chen and D. Chao designed the synthesis procedure and conducted all the electrochemical performance tests. F. Xie and Q. Gu carried out the *Operando* XRPD. F. Xie and B. Johannessen carried out the *ex-situ* XANES. S. Qiao supervised the project and co-wrote the manuscript. All authors discussed the results and contributed to writing the manuscript. All authors have approved the final version of the manuscript. ‡These authors contributed equally.

17

DECLARATION OF INTERESTS

The authors declare no competing financial interest.

References

1. Wang, M., Jiang, C., Zhang, S., Song, X., Tang, Y., and Cheng, H.M. (2018). Reversible calcium alloying enables a practical room-temperature rechargeable calcium-ion battery with a high discharge voltage. Nat. Chem. *10*, 667-672.

2. Li, Y., Yan, K., Lee, H.W., Lu, Z., Liu, N., and Cui, Y. (2016). Growth of conformal graphene cages on micrometre-sized silicon particles as stable battery anodes. Nat. Energy *1*, 15029.

3. Liu, N., Lu, Z., Zhao, J., McDowell, M.T., Lee, H.W., Zhao, W., and Cui, Y. (2014). A pomegranate-inspired nanoscale design for large-volume-change lithium battery anodes. Nat. Nanotechnol. *9*, 187-192.

4. Sun, J., Lee, H.W., Pasta, M., Yuan, H.T., Zheng, G.Y., Sun, Y.M., Li, Y.Z., and Cui, Y. (2015). A phosphorene-graphene hybrid material as a high-capacity anode for sodium-ion batteries. Nat. Nanotechnol. *10*, 980-U184.

5. Sultana, I., Rahman, M.M., Chen, Y., and Glushenkov, A.M. (2018). Potassium-ion battery anode materials operating through the alloying-dealloying reaction mechanism. Adv. Funct. Mater. *28*, 1703857

6. Lao, M., Zhang, Y., Luo, W., Yan, Q., Sun, W., and Dou, S.X. (2017). Alloy-based anode materials toward advanced sodium-ion batteries. Adv. Mater. *29*, 1700622.

7. Obrovac, M.N., and Chevrier, V.L. (2014). Alloy negative electrodes for Li-ion batteries. Chem. Rev. *114*, 11444-11502.

8. Yang, Z., Zhang, J., Kintner-Meyer, M.C.W., Lu, X., Choi, D., Lemmon, J.P., and Liu, J. (2011). Electrochemical energy storage for green grid. Chem. Rev. *111*, 3577-3613.

9. Sun, Y., Liu, N., and Cui, Y. (2016). Promises and challenges of nanomaterials for lithium-based rechargeable batteries. Nat. Energy *1*, 16071.

10. Jian, Z., Luo, W., and Ji, X. (2015). Carbon electrodes for K-ion batteries. J. Am. Chem. Soc. *137*, 11566-11569.

18

11. Zhang, W.C., Mao, J.F., Li, S.A., Chen, Z.X., and Guo, Z.P. (2017). Phosphorus-based alloy materials for advanced potassium-ion battery anode. J. Am. Chem. Soc. *139*, 3316-3319.

12. Hatchard, T.D., and Dahn, J.R. (2004). In situ XRD and electrochemical study of the reaction of lithium with amorphous silicon. J. Electrochem. Soc. *151*, A838-A842.

13. Wang, F., Wu, L., Key, B., Yang, X.Q., Grey, C.P., Zhu, Y., and Graetz, J. (2013). Electrochemical reaction of lithium with nanostructured silicon anodes: A study by in-situ synchrotron X-ray diffraction and electron energy-loss spectroscopy. Adv. Energy Mater. *3*, 1324-1331.

14. Sottmann, J., Herrmann, M., Vajeeston, P., Hu, Y., Ruud, A., Drathen, C., Emerich, H., Fjellvåg, H., and Wragg, D.S. (2016). How crystallite size controls the reaction path in nonaqueous metal ion batteries: The example of sodium bismuth alloying. Chem. Mater. *28*, 2750-2756.

15. Cook, J.B., Lin, T.C., Kim, H.S., Siordia, A., Dunn, B.S., and Tolbert, S.H. (2019). Suppression of electrochemically driven phase transitions in nanostructured MoS_2 pseudocapacitors probed using operando X-ray diffraction. ACS Nano *13*, 1223-1231.

16. Lu, J., Wu, T.P., and Amine, K. (2017). State-of-the-art characterization techniques for advanced lithium-ion batteries. Nat. Energy *2,* 17011.

17. Lin, F., Liu, Y., Yu, X., Cheng, L., Singer, A., Shpyrko, O.G., Xin, H.L., Tamura, N., Tian, C., Weng, T.C.*, et al.* (2017). Synchrotron X-ray analytical techniques for studying materials electrochemistry in rechargeable batteries. Chem. Rev. *117*, 13123-13186.

18. Gu, Q., Kimpton, J.A., Brand, H.E.A., Wang, Z., and Chou, S. (2017). Solving key challenges in battery research using in situ synchrotron and neutron techniques. Adv. Energy Mater. *7*, 1602831.

19. Bak, S.-M., Shadike, Z., Lin, R., Yu, X., and Yang, X.Q. (2018). In situ/operando synchrotron-based X-ray techniques for lithium-ion battery research. NPG Asia Mater. *10*, 563-580.

20. Xu, X., Zhao, R., Chen, B., Wu, L., Zou, C., Ai, W., Zhang, H., Huang, W., and Yu, T. (2019). Progressively exposing active facets of 2D nanosheets toward enhanced pseudocapacitive response and high-rate sodium storage. Adv. Mater. *31*, 1900526.

19

21. Chao, D., Liang, P., Chen, Z., Bai, L., Shen, H., Liu, X., Xia, X., Zhao, Y., Savilov, S.V., Lin, J., *et al.* (2016). Pseudocapacitive Na-ion storage boosts high rate and areal capacity of self-branched 2D layered metal chalcogenide nanoarrays. ACS Nano *10*, 10211-20219

22. Chao, D., Ouyang, B., Liang, P., Huong, T.T.T., Jia, G., Huang, H., Xia, X., Rawat, R.S., and Fan, H.J. (2018). C-plasma of hierarchical graphene survives SnS bundles for ultrastable and high volumetric Na-ion storage. Adv. Mater. *30*, 1804833.

23. Chao, D., Zhu, C., Yang, P., Xia, X., Liu, J., Wang, J., Fan, X., Savilov, S.V., Lin, J., Fan, H.J., *et al.* (2016). Array of nanosheets render ultrafast and high-capacity Na-ion storage by tunable pseudocapacitance. Nat Commun *7,* 12122.

24. Son, Y., Ma, J., Kim, N., Lee, T., Lee, Y., Sung, J., Choi, S.H., Nam, G., Cho, H., Yoo, Y., *et al.* (2019). Quantification of pseudocapacitive contribution in nanocage‐shaped silicon–carbon composite anode. Adv. Energy Mater. *9*, 1803480.

25. Pan, Y., Heryadi, D., Zhou, F., Zhao, L., Lestari, G., Su, H., and Lai, Z. (2011). Tuning the crystal morphology and size of zeolitic imidazolate framework-8 in aqueous solution by surfactants. CrystEngComm *13*, 6937-6940.

26. Xie, F., Zhang, L., Gu, Q., Chao, D., Jaroniec, M., and Qiao, S.Z. (2019). Multi-shell hollow structured Sb_2S_3 for sodium-ion batteries with enhanced energy density. Nano Energy *60*, 591-599.

27. Xie, F., Zhang, L., Su, D., Jaroniec, M., and Qiao, S.Z. (2017). $Na_2Ti_3O_7$@N-doped carbon hollow spheres for sodium-ion batteries with excellent rate performance. Adv. Mater. *29*, 1700989.

28. Zangmeister, R.A., Morris, T.A., and Tarlov, M.J. (2013). Characterization of polydopamine thin films deposited at short times by autoxidation of dopamine. Langmuir *29*, 8619-8628.

29. Chen, S., Duan, J., Ran, J., Jaroniec, M., and Qiao, S.Z. (2013). N-doped graphene film-confined nickel nanoparticles as a highly efficient three-dimensional oxygen evolution electrocatalyst. Energy Environ. Sci. *6*, 3693-3699.

30. Ferrari, A.C., and Basko, D.M. (2013). Raman spectroscopy as a versatile tool for studying the properties of graphene. Nat. Nanotechnol. *8*, 235-246.

31. Ferrari, A.C., and Robertson, J. (2000). Interpretation of raman spectra of disordered and amorphous carbon. Phys. Rev. B *61*, 14095-14107.

20

32. Huang, J.Q., Lin, X.Y., Tan, H., and Zhang, B. (2018). Bismuth microparticles as advanced anodes for potassium-ion battery. Adv. Energy Mater. *8,* 1703496.

33. Lei, K.X., Wang, C.C., Liu, L.J., Luo, Y.W., Mu, C.N., Li, F.J., and Chen, J. (2018). A porous network of bismuth used as the anode material for high-energy-density potassium-ion batteries. Angew. Chem. Int. Ed. *57*, 4687-4691.

21

Revealing the origin of improved reversible capacity of dual-shell bismuth boxes anode for potassium ion batteries

Fangxi Xie,[1‡] Lei Zhang,[1‡] Biao Chen,[1] Dongliang Chao,[1] Qinfen Gu,[2] Bernt Johannessen,[2] Mietek Jaroniec,[3] and Shi-Zhang Qiao*[1,4]

[1] School of Chemical Engineering, The University of Adelaide, Adelaide, SA 5005, Australia

[2] Australian Synchrotron (ANSTO), 800 Blackburn Rd, Clayton, VIC 3168, Australia

[3] Department of Chemistry and Biochemistry, Kent State University, Kent, Ohio 44242, United States

[4] Lead Contact

E-mail: s.qiao@adelaide.edu.au

Supporting Figures:
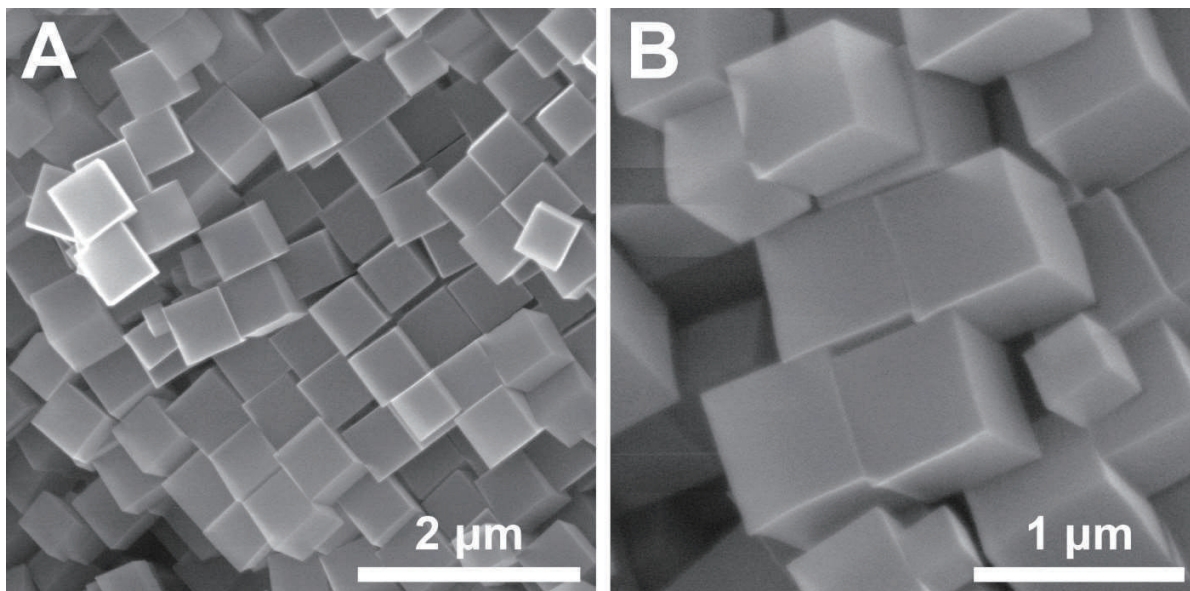
Figure S1 scanning electron microscope (SEM) images of ZIF-8 cubes.
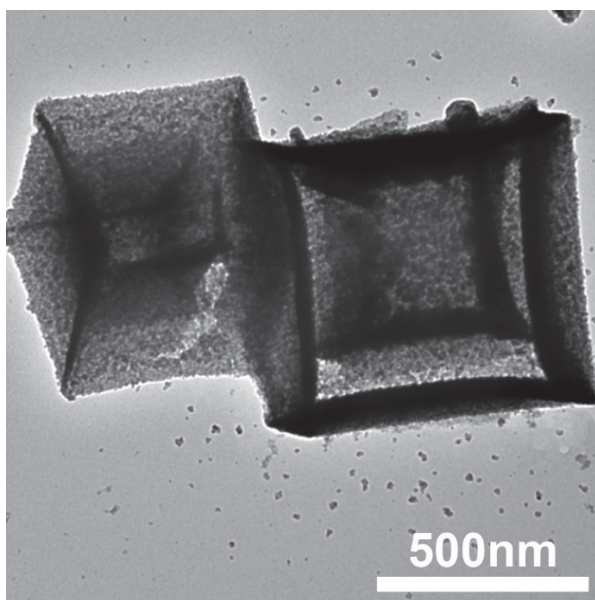
Figure S2 transmission electron microscope (TEM) image of Zinc sulfide precursor.
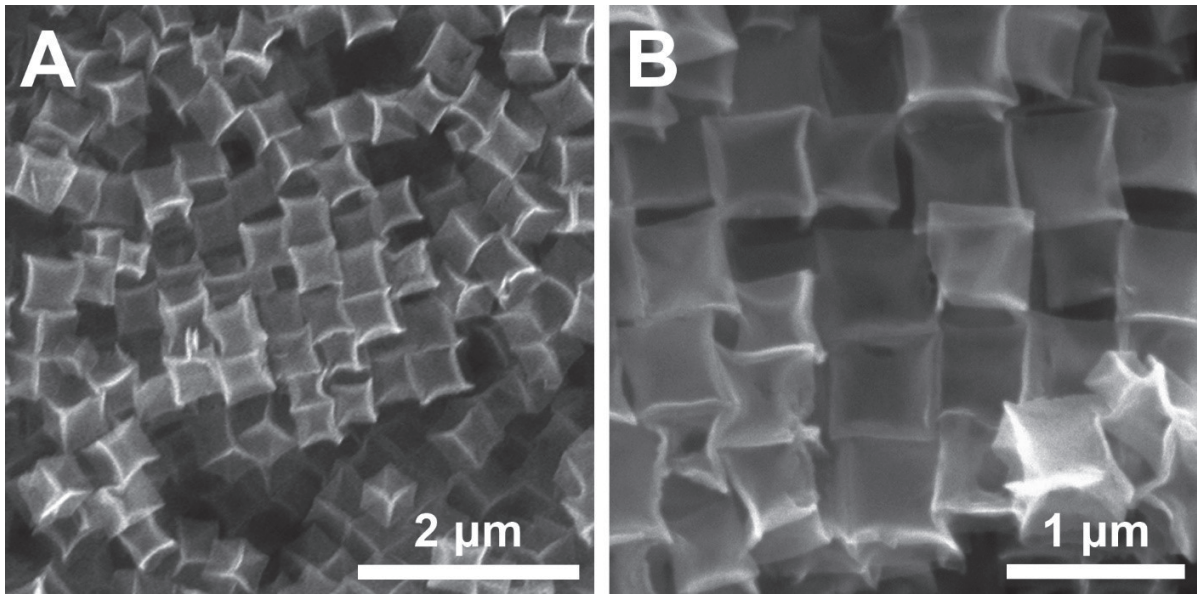
Figure S3 SEM images of dual-shell precursors.
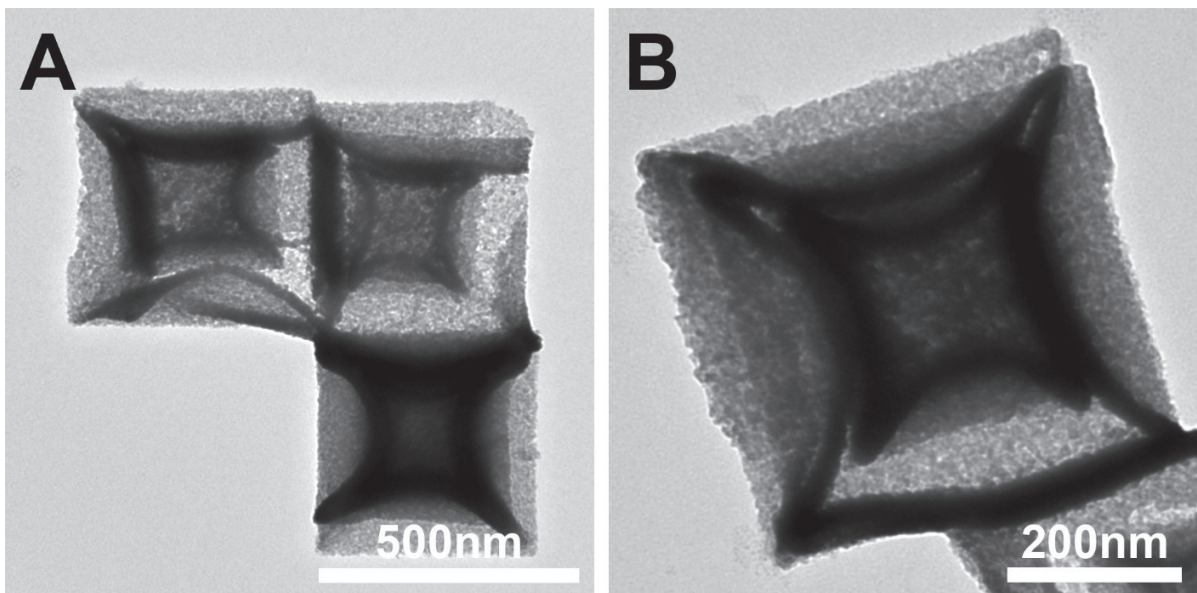
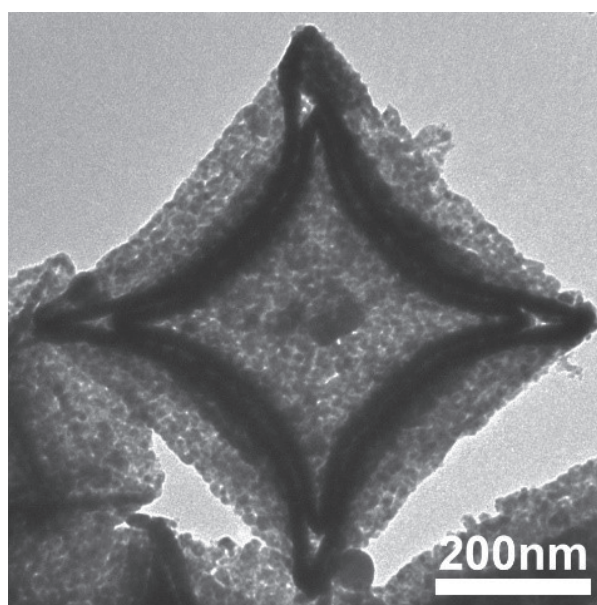**Figure S4** TEM images of dual-shell precursors.
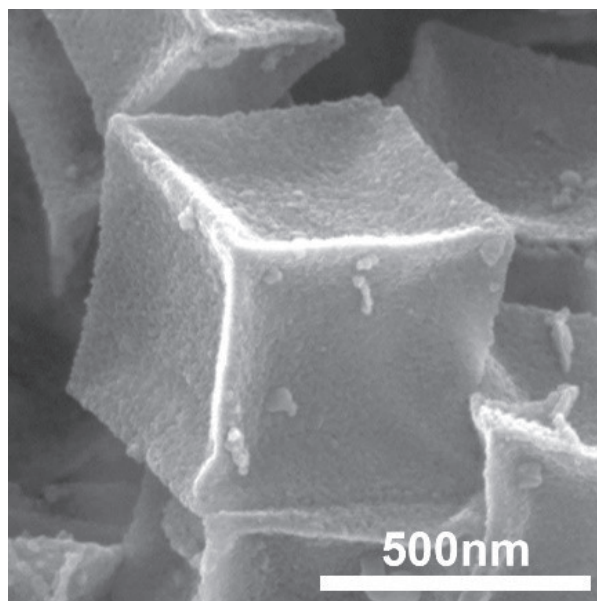
Figure S5 SEM image of C@DSBC.

Figure S6 TEM image of C@DSBC.
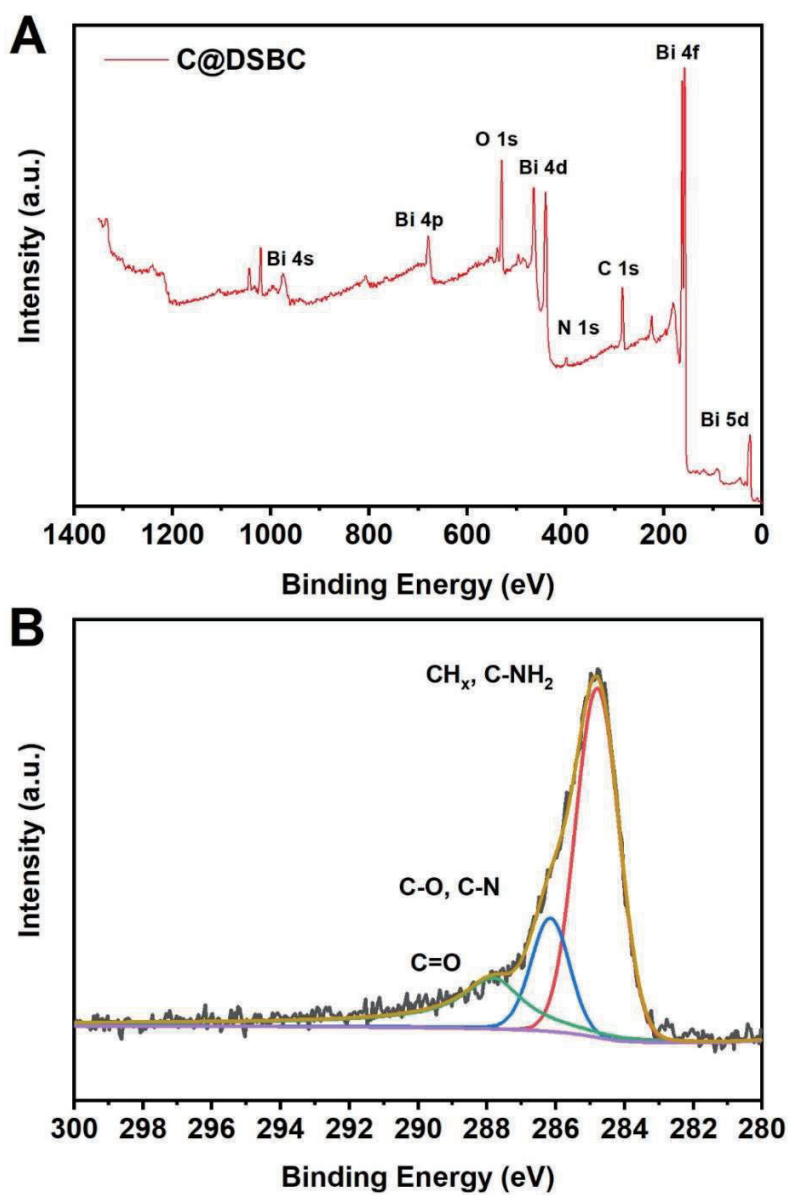
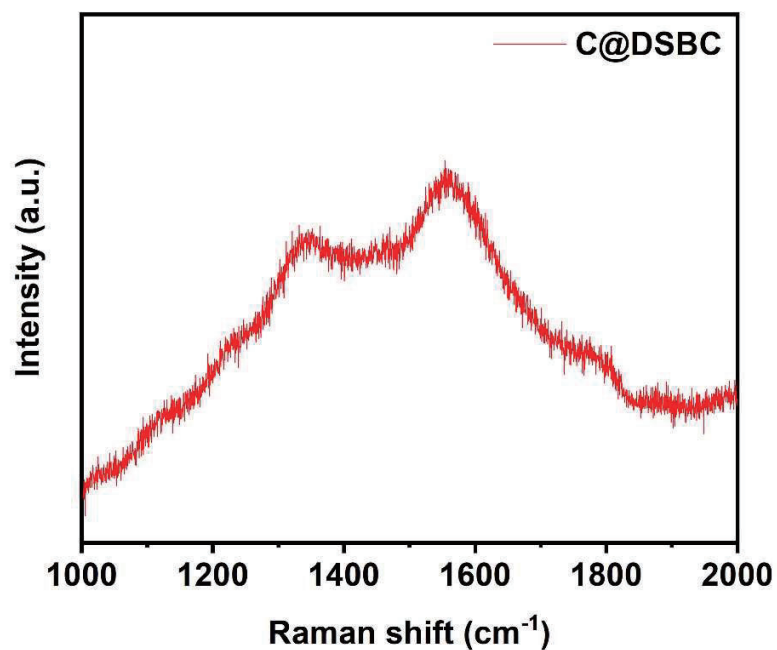**Figure S7** X-ray photoelectron spectroscopy (XPS) spectra of C@DSBC a) survey spectrum; b) high-resolution carbon spectrum.

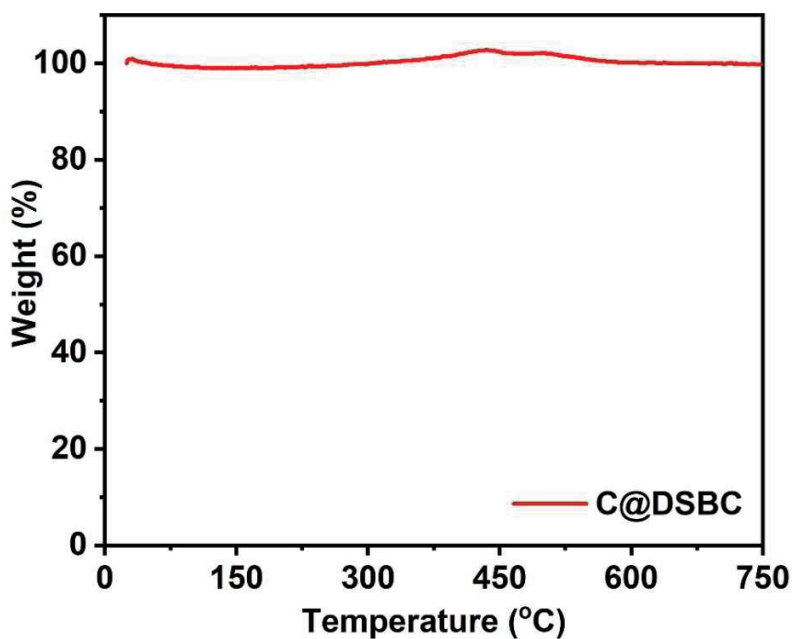**Figure S8** Raman spectrum of C@DSBC.

Figure S9 Thermogravimetric analysis profile of C@DSBC.

The mass loses after heating up to 750ºC is 0.77%. Since the final product is Bi_2O_3, the content of bismuth should be 92.9% and the carbon content is 7.1%.
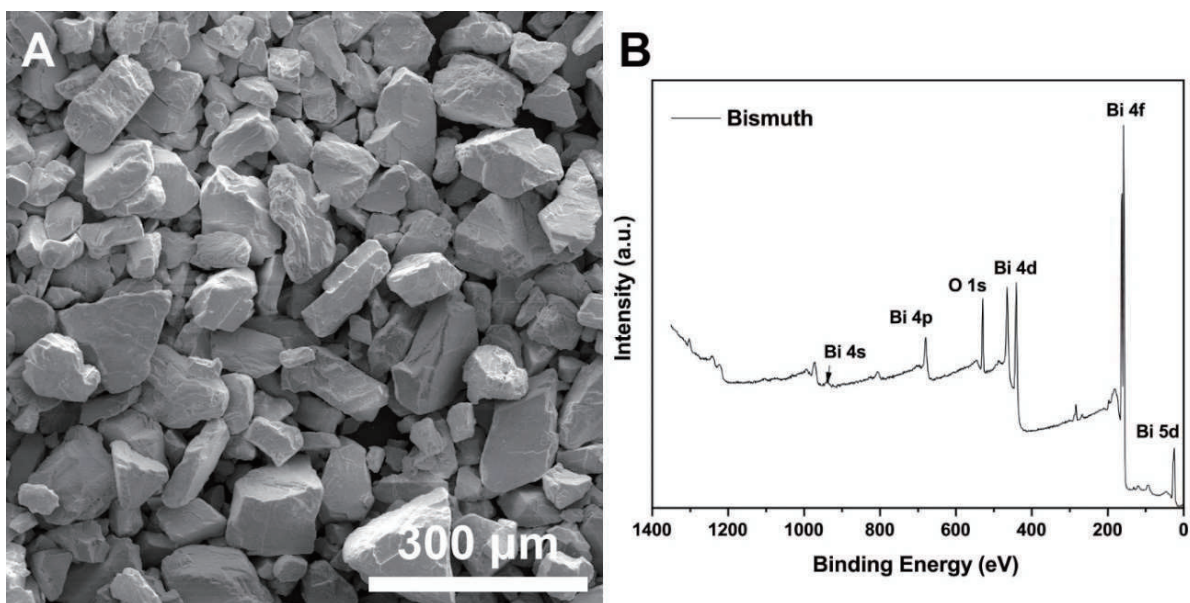
Figure S10 Detailed characterizations of microsized bismuth: A.)SEM image; B.)XPS survey spectrum.
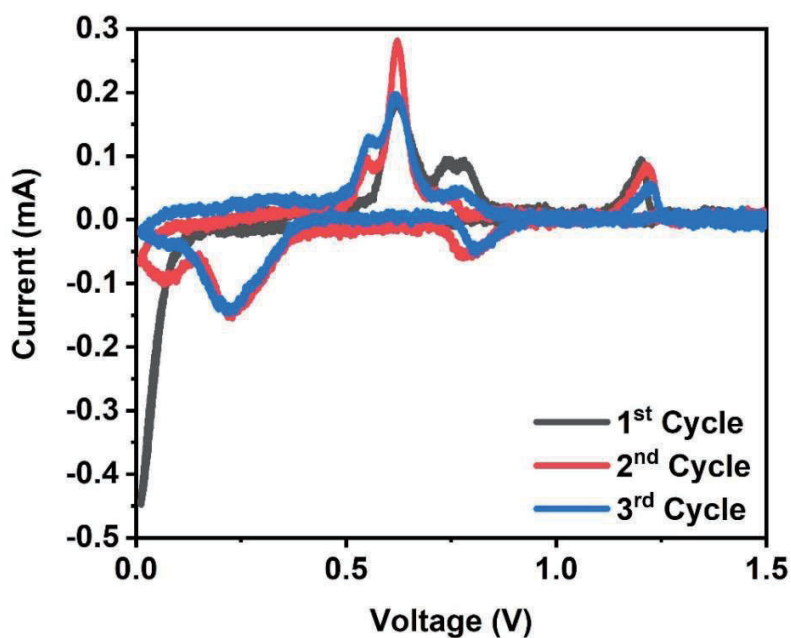

Figure S11 Initial cyclic voltammetry (CV) curves of microsized bismuth.
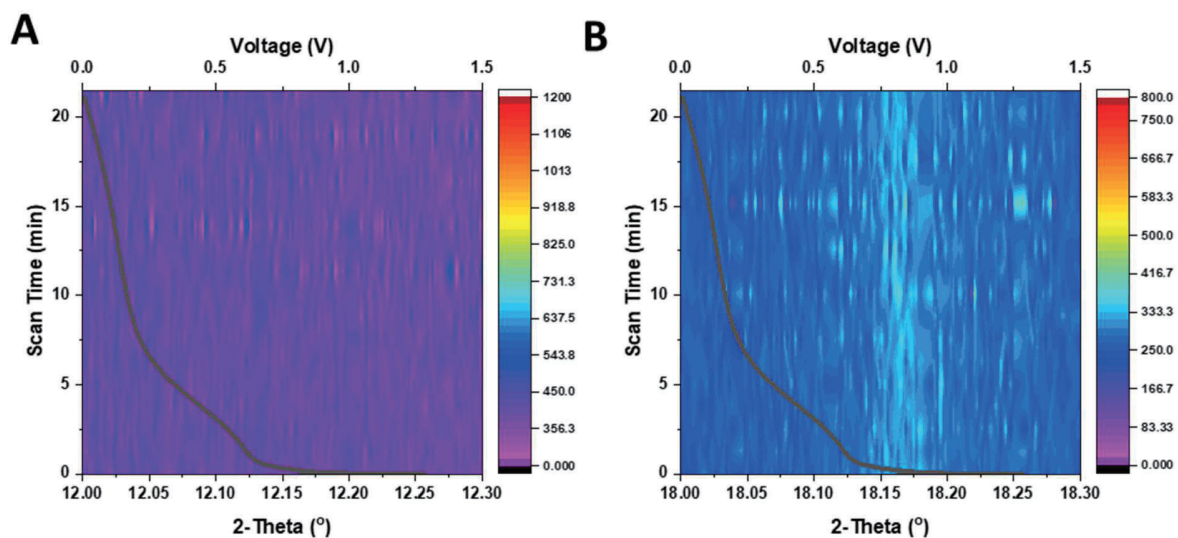
Figure S12 Contour plots of the *operando* synchrotron-based X-ray powder diffraction with superimposed voltage profiles shown for selected ranges of C@DSBC: (A) K_3Bi and (B) K_3Bi_2.
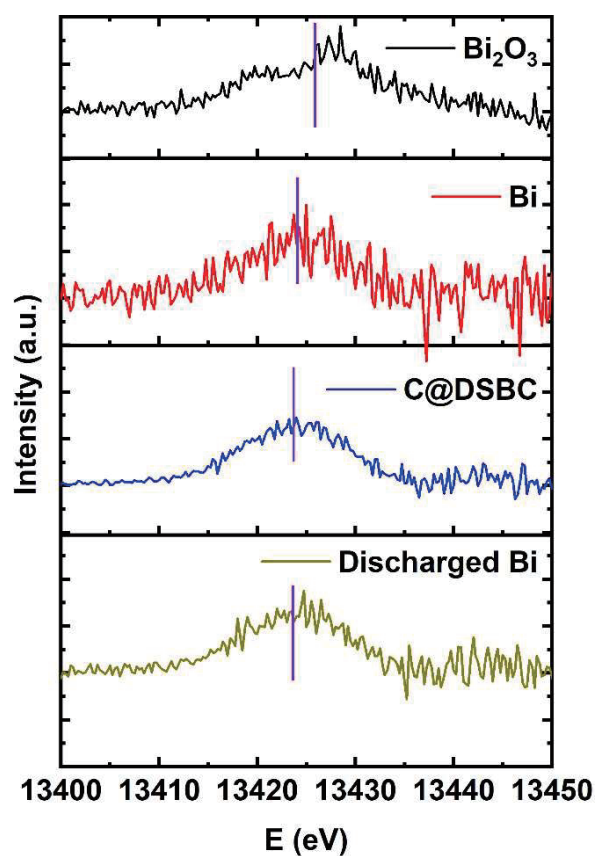

Figure S13 The selected part of the first derivative of the Bi-L_{III} edge spectra of the samples studied (the purple lines indicate the corresponding E_{mip})
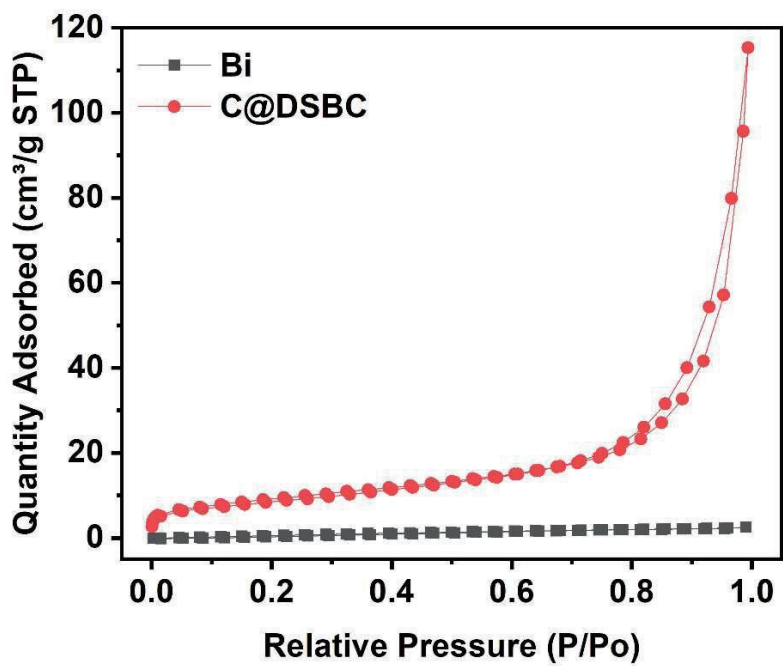
Figure S14 Nitrogen adsorption isotherms measured for bismuth samples.

Chapter 7 : Conclusions and perspectives

7.1 Conclusions

This thesis is devoted to rational design and engineering of hollow structured anodes for sodium and potassium ion batteries and to acquire fundamental insights into their enhanced electrochemical performance through various electrochemical approaches or synchrotron-based techniques. Based on the works included in this thesis, the following conclusion can be drawn:

1. The transportation of alkaline metal ions can be optimized by the rational engineering of building units of hollow structured electrode materials. Through the rational design and engineering of building units of hollow structured $Na_2Ti_3O_7$, $Na_2Ti_3O_7$ hollow spheres assembled from nanoparticles and nanosheets have been achieved. Specifically, the hollow spheres assembled from nanosheets exhibited a 33% higher charge capacity at the current density of 10 C than that of those assembled from nanoparticles, demonstrating that the building units of nanosheets facilitate the transportation of sodium ions.

2. The transportation of alkaline metal ions can be further optimized by the introducing oxygen vacancies in the nanosheets. Hollow structured sodium titanate and potassium titanate cubes assembled from nanosheets with oxygen vacancies have been synthesized. The as-prepared samples with oxygen vacancies both exhibited enhanced electrochemical performance in comparison to those ones without oxygen vacancies, demonstrating this approach as a versatile way to enhance the electrochemical performance of layered electrode materials.

3. Hollow structured materials are always considered as having high gravimetric energy density but low volumetric energy density. To solve this issue, multi-shell hollow structured Sb_2S_3 was synthesized to serve as a concept of proof to enhance the volumetric energy density of hollow structured materials. With the complex internal feature, the multi-shell structured Sb_2S_3 offered an enhanced energy density compared with its single-shell counterparts. Additionally, it also offered enhanced durability in comparison to its single-shell counterparts due to the extra support from interior shells. Both two points

demonstrated that the multi-shell structured electrode materials are more appealing than their single-shell counterparts.

4. It has been widely acknowledged that the nanosized alloy anodes offer improved reversible capacities compared to their microsized counterparts. However, the origin of these reversible capacities remains unclear. Therefore, we employed the dual-shell bismuth boxes as anodes for potassium ion batteries as a proof of concept and combined several *operando* synchrotron-based techniques to reveal the origin of the improved reversible capacity. As a result, it was revealed that the origins of the improved reversible capacities of nanostructured alloy anodes under low current density is the change of electrochemical reaction path while the one under high current density is the enhanced pseudocapacitive contribution.

In summary, various hollow structured electrode materials for sodium and potassium ion batteries have been developed. By applying those hollow structured electrodes in sodium and potassium ion batteries, it has been demonstrating that complex hollow structure can be employed to enhance the electrochemical performance of anodes for those batteries. Moreover, the insightful understandings of their improved electrochemical performance, such as the origins of the improved reversible capacity and the enhanced rate performance, are achieved from various characterizations.

7.2　Perspectives

Despite considerable progress has been achieved in the research area of hollow structured anode materials for rocking-chair batteries, more efforts are needed to achieve optimized structures and more insightful understandings for electrode materials to realize the practical application of those electrode materials.

1. The multi-shell structure can be applied to improve the volumetric energy density of hollow structured electrode materials. In the as-reported multi-shell structured anodes in this thesis, there are still significant gaps between those shells, resulting in lacking fully utilization of the voids inside those hollow structure. Therefore, to further explore the hollow structured anodes, more rational design and engineering should be achieved on better utilization of the inward voids to further enhance the volumetric energy density.

2. Apart from rational design and engineering, in my opinion, another future development direction for those hollow structured electrode materials can be to achieve more insightful understandings of their structure evolution during their cycling process. Up to now, most of the reports are about the investigation of the origin of the initial improved reversible capacity. The investigation about the origin of capacity fading and the hollow structure evolution during the cycling process remains rarely reported. Therefore, the research efforts can be paid on this aspect.

3. The further application of hollow structured electrode materials on other rocking-chair batteries, especially for those multivalent-ion batteries, remains occasionally reported. With the enhanced energy density derived from double or triple the number of electrons offered by one mole of multivalent ions, they are considered as more appealing choices than those single-valent ion batteries. Therefore, the application of hollow structured electrodes in those batteries demands more attention.

4. Furthermore, several issues remain to realize the practical applications of complex hollow structured electrode materials in rechargeable batteries. Firstly, nowadays, most of the synthesizing routes of complex hollow structured electrode materials are very complicated. Effort should be paid to explore and simplify the synthesis procedures to produce the hollow structured materials with high performance in a larger-scale, cost-effective and clean process. For example, developing template-free formation processes or exploring one-pot strategies to obtain hollow structured electrode materials could be two future directions to realize their practical applications. Secondly, another major barrier for rechargeable battery application is the low tap density of hollow structured materials due to their abundant inner voids. In my opinion, there are mainly two ways to solve this challenge: firstly, developing multi-shell structure to fulfill the inner voids with active materials; secondly, assembling the hollow structured particles to create micro-sized secondary structure which has high tap density to enhance the overall tap density of electrode materials. With these two strategies, the tap density of hollow structured materials could be improved, and the practical applications of hollow structured materials in rechargeable batteries might be realized.

To sum up, as far as I am concerned, more and more accomplishments in hollow structured electrode materials for rocking-chair batteries will be achieved through the increasing research interest in this field.

Appendix I: Publications during PhD Candidature

[1] **Fangxi Xie**, Lei Zhang, Chao Ye, Mietek Jaroniec, Shizhang Qiao, The application of hollow structured anodes for sodium-ion batteries: from simple to complex systems, *Advanced Materials*, **2018**, *30,* 1800492.

[2] **Fangxi Xie**, Lei Zhang, Dawei Su, Mietek Jaroniec, Shizhang Qiao, $Na_2Ti_3O_7$@N-doped carbon hollow spheres for sodium-ion batteries with excellent rate performance, *Advanced Materials*, **2017**, *29*, 1700989.

[3] **Fangxi Xie**, Lei Zhang, Qinfen Gu, Dongliang Chao, Mietek Jaroniec, Shizhang Qiao, Multi-shell hollow structured Sb_2S_3 for sodium-ion batteries with enhanced energy density, *Nano Energy*, **2019**, *60*, 591-599.

[4] **Fangxi Xie**, Lei Zhang, Biao Chen, Dongliang Chao, Qinfen Gu, Bernt Johannessen, Mietek Jaroniec, Shizhang Qiao, Revealing the origin of improved reversible capacity of dual-shell bismuth boxes anode for potassium ion batteries, *Matter*, 2019, *accepted for publication*

[5] **Fangxi Xie**, Lei Zhang, Yan Jiao, Anthony Vasileff, Shizhang Qiao, Dual-shell titanate cubes to optimize transport of large radii alkali ions, *to be submitted*

[6] Cheng Zeng[+], **Fangxi Xie**[+], Xianfeng Yang, Mietek Jaroniec, Lei Zhang, Shizhang Qiao, Ultrathin titanate nanosheets/graphene films derived from confined transformation for excellent Na/K ion storage, *Angew. Chem. Int. Ed*, **2018**, *57*, 8540-8544. ([+] Equal contribution)

[7] Chunxian Guo, Yao Zheng, Jingrun Ran, **Fangxi Xie**, Mietek Jaroniec, Shizhang Qiao, Engineering high‐energy interfacial structures for high‐performance oxygen‐involving electrocatalysis, *Angew. Chem. Int. Ed*, **2017,** *56*, 8539-8543.

[8] Biao Chen, Yuhuan Meng, **Fangxi Xie**, Fang He, Chunnian He, Kenneth Davey, Naiqin Zhao, Shizhang Qiao, 1D sub‐nanotubes with Anatase/Bronze TiO_2 nanocrystal wall for high‐rate and long‐life sodium‐ion batteries, *Advanced Materials*, **2018**, *30,* 1804116.

[9] Jinlong Liu, Yaqian Zhang, Lei Zhang, **Fangxi Xie**, Anthony Vasileff, Shizhang Qiao, Graphitic carbon nitride (g-C$_3$N$_4$)-derived N-rich graphene with tuneable interlayer distance as a high-rate anode for sodium-ion batteries, *Advanced Materials*, **2019**, *31,* 1901261.